

ELECTRON TRANSFER REACTIONS AT SENSITIZED NANOCRYSTALLINE
METAL OXIDE INTERFACES

Brian N. DiMarco

A dissertation submitted to the faculty of The University of North Carolina at Chapel Hill in
partial fulfillment of the requirements for the degree of doctor of Philosophy in the
Department of Chemistry.

Chapel Hill
2017

Approved by:

Gerald J. Meyer

Jillian L. Dempsey

Alexander J. M. Miller

Joanna M. Atkin

James F. Cahoon

© 2017
Brian N. DiMarco
ALL RIGHTS RESERVED

ABSTRACT

Brian N. DiMarco: Electron Transfer Reactions at Sensitized Nanocrystalline Metal Oxide Interfaces
(Under the Direction of Gerald J. Meyer)

The growing need for energy has spurred interest in the development of technologies that can directly convert solar irradiance into useful forms of energy. Dye-sensitized solar cells are a promising solar energy conversion technology due to the relatively low cost of the materials used and the tunability of the absorption profiles of the devices. The latter makes them amenable to integration into aesthetically appealing devices that can efficiently generating power. This thesis is focused on understanding the fundamentals of the electron transfer reactions that occur within these devices. The initial chapter introduces the environmental challenges facing humanity as a result of our current means of generating power. A review of the operation of a DSSCs and several important fundamental aspects are also introduced. Chapter 2 is focused on the influence that small structural changes have on the rate of electron self-exchange between ruthenium polypyridyl complexes anchored at nanocrystalline TiO_2 interfaces. Chapter 3 seeks to understand the role of Lewis acidic cations during interfacial electron transfer to solution phase electron acceptors. Chapter 4 compares the rates of interfacial electron to a pair of nearly identical triphenylamine acceptors, where one of the acceptors is functionalized with a phosphonic acid functional group that allowed it to anchored to the TiO_2 interface. This provided insight into the influence of surface anchoring on the recombination reaction. Chapter 5 assess the role of driving force during the

recombination reaction to series of substituted triphenylamine (TPA). The substitutions afforded and ~ 0.5 V change in the $\text{TPA}^{+/0}$ reduction potential, which was thought vary the driving force by the same amount. Chapter 6 compares charge recombination rates from TiO_2 and SnO_2 nanocrystalline thin films. Similar to Chapter 3, the role of Lewis acidic cations present in the external electrolyte was also investigated. Finally, Chapter 7 assess the role of electric fields and dipole moments on the injection and emissive properties of Ru polypyridyl complexes anchored at TiO_2 interfaces.

ACKNOWLEDGMENTS

I would first like to thank my parents, siblings and extended family for their support throughout this journey. I would not be where I am today without them. I am forever indebted to Prof. Cliff J. Timpson for his guidance while I attended RWU, and his friendship since graduation. I am forever in debt to the friendship and mentorship I received from the senior lab members in the Meyer group when I began. Darren, Atefeh, Will, Ryan, Ke and Erinn provided me with wonderful insights and training that were essential to my success. I must also thank Tim and Evan who help share the angst of the move from Hopkins to Chapel Hill, and to Wes and Tyler for being great lab mates when we arrived. I have been fortunate enough to work with several phenomenal scientists during my tenure in the Meyer group. Renato, Ludo, Cassie and Goucan each provided their own unique insights to many of the studies within this thesis, and greatly improved the quality of the work in the process. I've also had the pleasure of mentoring and training many of new students who have joined the lab in recent year. I feel strongly that each of them will contribute positively to our understanding of chemistry. I also need to thank my friends Steve Davidowski, Ron Lankone, Justin DeFrancisco and Justin Desrosiers for helping me to keep my sanity over the year with good conversations, cold drinks and backpacking adventures. I am thankful for the guidance provided to me by Dr. Jerry Meyer throughout my graduate career. I have thoroughly enjoyed my time in this lab, and I attribute the positive atmosphere that we all enjoy to his leadership. Last but not least, I must thank my girlfriend Suzanne for being an inexhaustible source of

support throughout the many challenges that we've both faced during our graduate careers. I couldn't have done this without her.

TABLE OF CONTENTS

LIST OF FIGURES.....	x
LIST OF SCHEMES	xv
LIST OF TABLES.....	xvii
LIST OF EQUATIONS.....	xviii
Chapter 1: Global Energy Demands and the Rise of Dye Sensitized Solar Cells.....	1
1.1 Current Energy Demand and Sources.....	1
1.2 Photovoltaic and the Rise of Dye Sensitized Solar Cells.....	5
1.2.1 Interfacial Electric Fields.....	11
1.2.2 Electron Transport.....	15
1.2.3 Charge Recombination.....	18
1.3 Conclusions.....	22
Chapter 2: A Distance Dependence to Lateral Self-Exchange Across Nanocrystalline TiO₂. A Comparative Study of Three Homologous Ru^{III/II} Polypyridyl Compounds.....	23
2.1 Introduction.....	23
2.2 Methods.....	28

2.3 Results.....	34
2.4 Discussion.....	43
2.5 Conclusions.....	49
Chapter 3: Cation Dependent Charge Recombination to Organic Mediators in Dye-Sensitized Solar Cells.....	51
3.1 Introduction.....	51
3.2 Experimental.....	53
3.3 Results.....	55
3.4 Discussion.....	60
3.5 Conclusion.....	64
Chapter 4: Electron Transfer at TiO₂ Interface. A Comparative Study Between Free and Anchored Tri-Phenylamine (TPA) Redox Mediators.....	65
4.1 Introduction.....	65
4.2 Methods and Materials.....	66
4.3 Results and Discussion.....	71
4.4 Conclusions.....	80
Chapter 5: Driving Force Dependent Charge Recombination to Solution Phase Triphenylamine Redox Mediators.....	81
5.1 Introduction.....	81
5.2 Experimental Section.....	82

5.3 Results.....	84
5.4 Discussion.....	89
5.5 Conclusion.....	93
Chapter 6: Influence of Lewis Acidic Cations and Phantom Electrons on Charge Recombination from Nanocrystalline SnO₂ Thin Films.....	95
6.1 Introduction.....	95
6.2 Results and Discussion.....	96
6.3 Conclusions.....	106
Chapter 7: Excited State Dipoles Oriented Parallel and Anti-Parallel to TiO₂ Surface Electric Fields.....	107
7.1 Introduction.....	107
7.2 Experimental.....	109
7.3 Results.....	113
7.4 Discussion.....	119
7.5 Conclusion.....	126
References.....	127

LIST OF FIGURES

Figure 1.1: Atmospheric CO ₂ concentrations measured over the past 50 years. Data taken from Ref 16.....	3
Figure 1.2: Global average temperatures over the past 130 years. Data reprinted from Ref 12..	3
Figure 1.3: Solar irradiance A.M. 1.5. The area shaded light gray can be absorbed by Si, while the dark gray can be absorbed by both Si and anatase TiO ₂ . The dashed blue lines represent the spectral response observed for a TiO ₂ thin film sensitized with a champion Ru complex ²⁸	6
Figure 1.4: Representation of the advancements in DSSCs. Taken from Ref 27.....	7
Figure 1.5: Schematic representation of a dye sensitized solar cell. In this figure, S is the surface anchored sensitizer, while M is the solution phase redox mediators. The injection, k_{reg} , sensitizer regeneration, k_{reg} and recombination reaction to the redox mediator, k_{rec} , or oxidized sensitizer, k_{rec2} , are shown.....	7
Figure 1.6: Representative current-voltage (IV) plot.....	9
Figure 1.7: (A) Shown in orange are the residuals seen after spectral modeling of the raw data (purple) (B) Similar spectral feature observed after application of an electrochemical bias. Figures adapted from Ref 64	13
Figure 1.8: Transient absorption data where the electrons in the substrate were monitored at 750 nm, while also monitored in the Stark effect. The Stark effect clearly decays in a region where there is minimal electron loss. Data taken from Ref 76.....	14
Figure 1.9: Lateral electron self-exchange between surface anchored Ru chromophores. Adapted from Ref 95.....	16
Figure 1.10: Contributions from both the charge carrier diffusion through/across the TiO ₂ and the electron transfer event on the overall rate of recombination. Figure adapted from Ref 56.....	20
Figure 2.1: Plot of an example one-dimensional reaction coordinate	

for a nonadiabatic (dashed lines) or adiabatic (solid lines) self-exchange electron transfer reaction. The orange and green spheres represent Ru molecules in the encounter complex before, during, and after electron transfer. The blue spheres depict counter ions and exaggerates their location and movement during the electron transfer process.....	26
Figure 2.2: a) Crystal structure of [Ru(dmb) ₂ (deeb)](PF ₆) ₂ . b) Crystal structure of [Ru(dtb) ₂ (dcbH ₂)](ClO ₄) ₂ . All hydrogen atoms and anions are omitted for clarity purpose. Color code: Pink, Ru; blue, N; red, O; gray, C.....	36
Figure 2.3: Normalized absorption spectra of compounds bpy , dmb , and dtb anchored to TiO ₂ in neat CH ₃ CN (solid line) or in a 0.1 M LiClO ₄ solution in CH ₃ CN (dashed line). The TiO ₂ absorption spectrum was subtracted out from the spectra of the surface-functionalized films.....	36
Figure 2.4: Spectroelectrochemical oxidation of TiO ₂ dmb immersed in 0.1 M LiClO ₄ /CH ₃ CN electrolyte. The inset plots the fraction of oxidized or reduced compound as a function of applied potential. Overlaid is a fit to a modified Nernst equation, Equation 2.5	38
Figure 2.5: Normalized absorption change measured after application of a potential sufficient to oxidize the indicated compounds plotted against the square root of time. Overlaid in gold is the fit based on Equation 2.6	40
Figure 2.6: Representative cyclic voltammograms for dmb anchored to TiO ₂ immersed in 0.1 M LiClO ₄ in CH ₃ CN at the indicated temperatures.....	40
Figure 2.7: (A) Arrhenius plot for bpy , dmb , and dtb anchored to TiO ₂ describing the variation of D_{CV} with inverse temperature as obtained by cyclic voltammetry. Overlaid are the best fits to the Arrhenius equation. (B) The temperature dependence of k_{SE} as described by non-adiabatic Marcus theory (overlaid curves).....	43
Figure 3.1: Steady-state UV-Vis absorbance of TiO ₂ Ru thin film submerged in 0.1 M acetonitrile solutions of the indicated metal perchlorate salt.....	55
Figure 3.2: The visible absorption spectra of TPTA ⁺ and PTZ ⁺ in 0.1 M NaClO ₄ /CH ₃ CN electrolyte.....	57
Figure 3.3: Absorption difference spectra measured at the indicated delay times after pulsed 532 nm laser excitation of a TiO ₂ Ru thin	

film in a 0.1 M NaClO ₄ /CH ₃ CN electrolyte containing A) 25 mM TPTA and B) 50 mM PTZ. Overlaid on the data as solid lines are spectral simulations.....	58
Figure 3.4: Single wavelength absorption changes measured after pulsed 532 nm laser excitation of a TiO ₂ Ru thin film in CH ₃ CN solutions with 0.1 M of the indicated metal perchlorate and A) 25 mM TPTA and B) 50 mM PTZ. Kinetics were monitored at 675 nm and 433 nm for TPTA ⁺ and PTZ ⁺ respectively. Fits to the KWW model are overlaid on the data as solid yellow lines.....	59
Figure 4.1: Structure of the ruthenium dye RuP , f-TPA and a-TPA used in this study.....	66
Figure 4.2: Cyclic voltammograms performed in 0.1 M LiClO ₄ acetonitrile.....	72
Figure 4.3: UV-Vis spectra of RuP sensitized TiO ₂ in neat ACN (black) and 0.1 M LiClO ₄ CH ₃ CN solution (red) as well as singly oxidized f-TPA ⁺ (blue) and a-TPA ⁺ (green).....	73
Figure 4.4: Absorption changes observed after pulse 532 nm light irradiation of TiO ₂ RuP in the presence of 30 mM f-TPa (Blue scale) or cofunctionalized with a-TPA (red scale) submerged in argon saturated 0.1 M LiClO ₄ CH ₃ CN.....	74
Figure 4.5: Single wavelength kinetics of f-TPA (a) and a-TPA (b) at various laser fluencies. Insets represent the abstracted rate using a stretched exponential fitting versus absorption changes..	75
Figure 4.6: Single wavelength kinetics of f-TPA (a) and a-TPA (b) at various temperatures. Arrhenius plot (c) for f-TPA (blue squares) and a-TPA (green circles).....	78
Figure 4.7: Schematic representation of the charge recombination processes for a-TPA and f-TPA	80
Figure 5.1: Cyclic voltammograms performed for each TPA in acetonitrile solutions.....	85
Figure 5.2: Absorption spectra generated for TPA ⁺ in acetonitrile electrolytes.....	86
Figure 5.3: Transient absorption spectra generated for TiO ₂ S submerged in 8 mM MeO -TPA at early (A) and late timescales (B).....	87
Figure 5.4: Transient absorption spectra generated after pulsed light excitation of TiO ₂ S in the presence of 8 mM Cl -TPA.....	87

Figure 5.5: Recombination kinetics to TPA^+ . Overlaid are the best fits to these kinetic traces...	89
Figure 5.6: Normalized recombination kinetics observed for Cl -TPA.....	89
Figure 6.1: UV-Vis absorption changes for $\text{SnO}_2 \text{Ru}$ films submerged in acetonitrile electrolytes. The spectral taking in LiClO_4 and $\text{Mg}(\text{ClO}_4)_2$ were normalized relative to the sample in neat acetonitrile.....	97
Figure 6.2: (A) Spectral changes observed after pulse light excitation of $\text{SnO}_2 \text{Ru}$ submerged in argon purge acetonitrile containing 0.1 M LiClO_4 and 0.25 M TBAI. (B) Comparison of spectral changes 2.5 μs after excitation observed for TiO_2 and SnO_2 substrates in the presence of 0.25 M TBAI and either 0.1 M LiClO_4 or $\text{Mg}(\text{ClO}_4)_2$	99
Figure 6.3: Recombination kinetics to I_3^- monitored at 375 nm. Overlaid are the best fits using a tri-exponential function.....	100
Figure 6.4: Comparison between the absorption measure at 375 and 800 nm at 100 μs	102
Figure 6.5: Absorption comparison between I_3^- and TiO_2 monitored $\sim 100 \mu\text{s}$ after pulse light excitation. Approximately 20 μs of data was averaged around this time point to improve signal to noise, and the error bars represent the observed standard deviation in this measurement....	103
Figure 7.1: Steady-state absorption and normalized photoluminescence (PL) spectra of A) $\text{Ru}(\text{dtb})_2(\text{dcb})/\text{TiO}_2$ and B) $\text{Ru}(\text{btfmb})_2(\text{dcb})/\text{TiO}_2$ in neat acetonitrile and in the presence of 0.1 M perchlorate acetonitrile solutions. Steady-state difference absorption spectra (ΔA_{ss}) of C) $\text{Ru}(\text{dtb})_2(\text{dcb})/\text{TiO}_2$ and D) $\text{Ru}(\text{btfmb})_2(\text{dcb})/\text{TiO}_2$ in the indicated perchlorate acetonitrile solutions.....	114
Figure 7.2: Steady-state PL spectra of A) and B) $\text{Ru}(\text{dtb})_2(\text{dcb})/\text{TiO}_2$ and C) $\text{Ru}(\text{btfmb})_2(\text{dcb})/\text{TiO}_2$ in 0.1 M LiClO_4 acetonitrile at the indicated applied potentials.....	116
Figure 7.3: The PL intensity maximum wavelength of A) $\text{Ru}(\text{dtb})_2(\text{dcb})/\text{TiO}_2$ and B) $\text{Ru}(\text{btfmb})_2(\text{dcb})/\text{TiO}_2$ measured in the five 0.1 M cation perchlorate acetonitrile solutions as a function of applied potential. The dotted line is PL center wavelength measured for $\text{Ru}(\text{dtb})_2(\text{dcb})/\text{TiO}_2$ and $\text{Ru}(\text{btfmb})_2(\text{dcb})/\text{TiO}_2$ in neat acetonitrile. The relative PL intensities of C) $\text{Ru}(\text{dtb})_2(\text{dcb})/\text{TiO}_2$ and D) $\text{Ru}(\text{btfmb})_2(\text{dcb})/\text{TiO}_2$ in 0.1 M cation perchlorate acetonitrile solutions at various applied potentials. The PL intensities of the $>200 \text{ mV}$ bands were normalized to one	

and the corresponding, more negative potential PL bands, were scaled relative to the >200 mV band. The black circles in **A** and **C** are from $[\text{Ru}(\text{dtb})_2(\text{dcb})]^{2+}$ anchored to ZrO_2 in Li^+ solution.....117

Figure 7.4: Representative time-resolved PL of $\text{Ru}(\text{dtb})_2(\text{dcb})/\text{TiO}_2$ in **A)** Li^+ and **B)** Mg^{2+} acetonitrile solutions at the indicated applied potentials. The black lines are from fitting with **Equation 2** where the first-order rate constant was held constant and $\tau_2 = 1/k_2$ was determined through global fits of the time-resolved data. The insets show τ_2 at each applied potential.....118

LIST OF SCHEMES

Scheme 1.1: Commonly used champion sensitizers.....	10
Scheme 2.1: Illustration of lateral intermolecular self-exchange electron transfer across anatase TiO ₂ nanocrystallites initiated at the fluorine-doped tin oxide (FTO) substrate.....	24
Scheme 2.2: Chemical Structure of the Molecules Used in this Hole Hopping Study.....	28
Scheme 2.3: An idealized representation of three surface functionalized anatase layers on an FTO substrate during a chronoabsorptometry (CA) experiment. At time t_0 all of the ruthenium compounds are in the formal oxidation state of II. After a potential step 500 mV more positive than the formal $E^\circ(\text{Ru}^{\text{III/II}})$ reduction potential, the FTO substrate oxidizes the Ru ^{II} compounds present on the FTO surface followed by self-exchange ‘hopping’ across the nanocrystalline TiO ₂ surface. A moving front of oxidized dyes nearly equidistant from the FTO substrate is observed at $t > t_0$. At longer times $t \gg t_0$ all the molecules within the mesoporous thin film are oxidized. The semi-infinite diffusion boundary approximation restricts data analysis to about 60% oxidation of the thin film. In cyclic voltammetry experiments that are now shown, only about 5% of the film is oxidized.....	46
Scheme 3.1: Organic redox mediators.	53
Scheme 3.2: Comparison of the redox potentials of the mediators employ, and the energetics of the distribution of trap states in TiO ₂ when different cations are employed. Reduction potentials for I ₃ ⁻ /(I ₂ [•] , I [•]) and I [•] /I are taken from reference. The latter potential is relevant to sensitizer regeneration.....	63
Scheme 5.1: Structure of the triphenylamines used throughout these studies.....	82
Scheme 5.2: The dotted lines below the colored areas represent the energy threshold required for efficient recombination.....	92
Scheme 6.1: Structure of [Ru(dtb) ₂ (dcb)] ²⁺	97
Scheme 6.2: Comparison of the I ₃ ⁻ reduction potential and the distribution of optically active electron accepting states for SnO ₂ or TiO ₂ in Li ⁺ and Mg ²⁺ based electrolytes.....	105

Scheme 7.1: Ruthenium polypyridyl compounds used in this study.....	110
--	-----

LIST OF TABLES

Table 2.1. Selected Crystal Structure Parameters for a Series of Ru Polypyridyl Compounds.....	36
Table 2.2. Selected Spectral, Electrochemical, and Film Parameters for the Compounds Studied.....	38
Table 2.3. Apparent Diffusion Coefficients and Marcus Self-Exchange Parameters for Surface Anchored Ruthenium Compounds.....	40
Table 3.1: Rate constants abstracted from KWW fits to the time resolved absorption data...	59
Table 4.1: Electrochemical and photophysical properties of RuP , <i>a</i>-TPA and <i>f</i>-TPA . Electrochemical data are recorded in 0.1M LiClO ₄ CH ₃ CN solution whereas photophysical data are recorded in argon saturated CH ₃ CN.....	72
Table 5.1: Summary of electrochemical, spectroscopic and kinetic data.....	86
Table 6.1: Values obtained from tri-exponential fit to recombination data.....	101
Table 7.1: Photophysical and Electrochemical Properties of Ru(dtb) ₂ (dcb)/TiO ₂ and Ru(btfmb) ₂ (dcb)/TiO ₂ in 0.1 M Cation Perchlorate Acetonitrile Solutions...	115

LIST OF EQUATIONS

Equation 1.1: Light harvesting efficiency.....	9
Equation 1.2: The diode equation	10
Equation 1.3: Molecule dipole moment determined from an absorbance shift.....	13
Equation 1.4: The Kohlraush-Williams-Watts function.....	19
Equation 1.5: Diffusional and electron transfer contributions to observed rate constants.....	21
Equation 2.1: Non-adiabatic Marcus theory.....	25
Equation 2.2: Determination of surface coverage from absorbance.....	33
Equation 2.3: Surface concentration based on calculated surface coverage.....	33
Equation 2.4: Intermolecular distance based on surface concentration.....	33
Equation 2.5: Modified Nernst equation	39
Equation 2.6: Apparent electron diffusion coefficient - absorbance.....	39
Equation 2.7: Apparent electron diffusion coefficient – current density.....	41
Equation 2.8: Arrhenius equation for electron self-exchange.....	41
Equation 2.9: Electron self-exchange rate.....	42
Equation 2.10: Non-adiabatic Marcus theory	42
Equation 3.1: The Kohlraush-Williams-Watts function.....	58
Equation 3.2: Average KWW rate constant.....	59
Equation 3.3: Recombination reaction to an organic acceptor.....	60
Equation 4.1: Recombination reaction to a triphenylamine acceptor.....	75
Equation 4.2: A Sum of Kohlraush-Williams-Watts functions.....	76
Equation 4.3: Average KWW rate constant	76
Equation 5.1: A Sum of Kohlraush-Williams-Watts functions.....	88
Equation 5.2: Average KWW rate constant	88
Equation 6.1: Determination of surface coverage from absorbance	98
Equation 6.2: Tri-exponential fitting function.....	101
Equation 6.3: Average rate constant from tri-exponential fit.....	101
Equation 6.4: Observed extinction coefficient based on transient absorption data	103
Equation 7.1: Excited-state reduction potential $\text{Ru}(\text{III}/\text{II}^*)$	112

Equation 7.2: Excited-state reduction potential $\text{Ru}(\text{II}^{*/+})$	112
Equation 7.3: Parallel first- and second-order kinetic model.....	118
Equation 7.4: Electron excited-state localization: $[\text{Ru}(\text{dtb})_2(\text{dcb})]^{2+}$	119
Equation 7.5: Electron excited-state localization: $[\text{Ru}(\text{btfmb})_2(\text{dcb})]^{2+}$	120
Equation 7.6: Onsager theory of geminate recombination.....	124
Equation 7.7: Field dependent disassociation probability.....	124
Equation 7.8: Luminescence dependence on disassociation probability.....	124

Chapter 1: Global Energy Demands and the Rise of Dye Sensitized Solar Cells

1.1 Current Energy Demand and Sources

As the world's population continues to grow and more nations increase their standard of living, so too will our global energy demands.¹ Total energy production generated globally was 1.61×10^8 kWh in 2012, with this value being expected to increase to 1.84×10^8 kWh by 2020, and 2.39×10^8 kWh by 2040, representing an approximate 40% increase in power consumption.¹ The ability to meet future energy demands with sustainable forms of energy production represents one of the largest challenges currently facing humanity as it is becoming abundantly clear that current means of energy production, mainly the burning of fossil fuel, is unsustainable. The best course of action is to develop a diverse energy portfolio that can largely eliminate our current dependence on fossil fuels.

Large man-made disasters resulting from fossil fuel collection and distribution are numerous, having both short and long term environmental impacts.² The scale of these disasters also seems to be increasing with time. As an example, the Exxon-Valdez oil spill of 1989 resulted in the release of an estimated 1.1 million gallons crude oil into Prince Williams Sound, and was the largest spill on record at the time. The environmental impacts of this spill are still being assessed even today. More recently, the Deepwater Horizon spill of 2013 spilled more than 210 million gallons of oil into the Gulf of Mexico, dwarfing the Exxon-Valdez spill. Much like the Exxon-Valdez spill, it will likely be years before the damage from this spill can be fully assessed.³ The scale of this spill was likely due to new drilling techniques, which

operate in more remote and demanding environments. These sorts of spills will likely occur more regularly as more easily accessible sources become scarce, driving exploration into harsher and more demanding environments.

The burning of fossil fuels leads to the release of gaseous pollutants, heavy metals and particulate matter that are all known to have a negative impact on human health.^{4,5} However, it could be argued that main problem with all fossil fuel based energies is the release of CO₂ in enormous quantities.⁶ It has been estimated that between 0.5 and 1 kg of CO₂ is released per kilowatt hour (kWh) of energy generated depending on the source.⁴ In 2015, the US energy sector consumed enough fossil fuels to release an estimated 1.9×10^{12} kg of CO₂ into the atmosphere.⁴ Despite the enormous size of the atmosphere, estimated to be 5×10^{18} kg⁷, there is growing evidence that the rate at which fossil fuels are burned is having an impact on the atmospheric CO₂ concentrations. Theoretically, increased atmospheric CO₂ can lead to increased global temperatures by trapping thermal energy through a process known as the greenhouse effect.⁸ There has been increasing experimental evidence of such a link between global temperatures and atmospheric CO₂ concentrations. For example, Antarctic ice cores contain representative snap-shots of global atmospheric conditions through trapped bubble of gas, while temperatures can be related to the ¹⁸O/¹⁶O isotopic ratio seen in the frozen water.⁹ Based on these data, a correlation between CO₂ concentrations and global temperature have been made, in agreement with predictions based on the greenhouse effect.^{10,11}

Contemporary atmospheric CO₂ concentrations were first measured in the late 19th century, which were found to be 292 ppm.⁸ Since these initial measurements, a gradual increase in the atmospheric CO₂ concentration has been observed, with recent estimates placing concentrations higher than 400 ppm, **Figure 1.1**. A gradual increase in average global

temperatures have also been observed over this period, **Figure 1.2**, in agreement with the correlation made from ice core data.¹² Concerningly, small changes in phenology, or the timing of seasonal ecological activities such as migration, have been observed over the past few decades and are often attributed to increased global temperatures.¹³ Such changes have the potential to cause massive rates of extinction in animals that rely on seasonal timing for mating, hibernation etc.^{14,15} In order to mitigate changes in the climate, drastic and rapid changes to our energy production methods are needed.

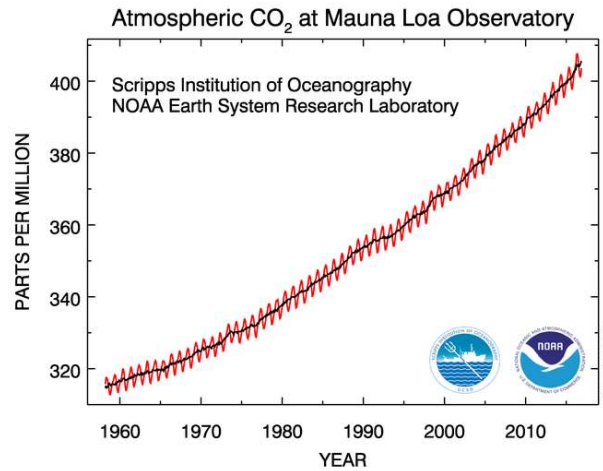


Figure 1.1: Atmospheric CO₂ concentrations measured over the past 50 years. Data take from ref 16.

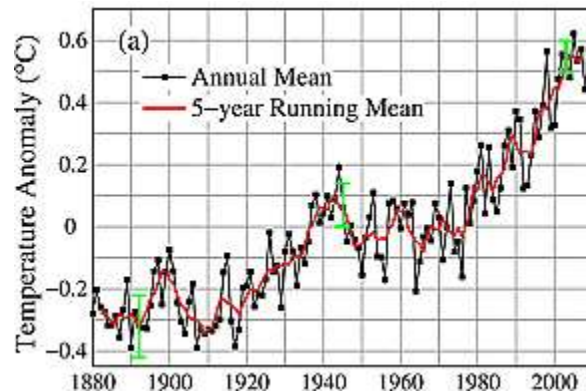


Figure 1.2: Temperature anomalies over the past 130 years. Data reprinted from Ref 12.

Currently, only 18.9% of the global energy demands are met with non-fossil fuel sources, with biofuels and nuclear taking the largest percentages at 10.3% and 4.8% respectively¹. However, neither of these sources is ideal. Though there is a net energy gain to be had from biofuel production¹⁷, meeting our energy demands through this technology would mean expanding farmlands, likely leading to increased deforestation which could ultimately exacerbate global warming.¹⁸ The many benefits of nuclear, including the extremely high energy density of the fuel, are overshadowed by the difficulties seen while managing the radioactive waste generated during energy production.¹⁹ While the years 2013-2014 saw an ~11% increase in energy production from geothermal, solar thermal, photovoltaics and wind¹, greater strides must be taken in developing these technologies in order to avoid catastrophic environmental changes.

Solar energy harvesting represents the best solution to our current and future demands. In only 1.33 hours, enough solar energy strikes the Earth to meet our current annual global energy demands.²⁰ Several promising photovoltaic technologies have emerged over the past few decades which may one day be used to generate the majority of our energy. An obvious limitation for solar is its intermittency, requiring significant energy storage to account times of darkness and heavy cloud coverage. Several approaches are successfully addressing these issues, though their description is beyond the scope of this thesis.^{21,22} Instead, this thesis will be concerned with direct solar to energy conversion, specifically focusing on dye sensitized solar cells (DSSC).

1.2 Photovoltaic and the Rise of Dye Sensitized Solar Cells.

Crystalline silicon is arguable the most prolific photovoltaic (PV) technology available today. Silicon PVs are known to have light-to-energy conversion efficiencies as high as 25%, and their relatively low cost makes them particularly appealing.²³ The cost of Si PVs have also been steadily declining over the past few years, due in part to the scale at which they are being produced.²⁴ Despite the current dominance of Si PVs, a more efficient and less expensive alternative could easily supplant Si as the primary PV technology.

Crystalline silicon has a band gap of 1.1 eV allowing it to absorb photons with energies above this threshold. This spectral response is well tuned to match the solar spectrum, **Figure 1.3**.²⁵ This broad absorption is not without its drawbacks. Photons with energies more than 1.1 eV will thermalize to the bandgap, losing the additional energy as heat.²⁶ Employing wide-bandgap semiconductors would allow for more energy to be extracted from each photon, but only a small fraction of the solar spectrum can be absorbed by these materials. As an example, the fraction of the solar spectrum that can be absorbed by anatase TiO₂ (band-gap of 3.2 eV) is shown in **Figure 1.3**, and only represents 3% of the solar irradiance.²⁷

An ingenious solution to this problem is to combine wide bandgap semiconductors with molecular chromophores which can absorb visible light and transfer the photon's energy to the semiconductor via electron transfer. These molecules are termed "sensitizers" since they extended the spectral response of the semiconductor well into the visible spectrum, **Figure 1.3**. Reports of wide bandgap semiconductor sensitization date back to the 1960's²⁹, though the concept of sensitization has been around since the end of the 18th century.³⁰ During the early development of the sensitization of wide bandgap semiconductors, titanium dioxide emerged

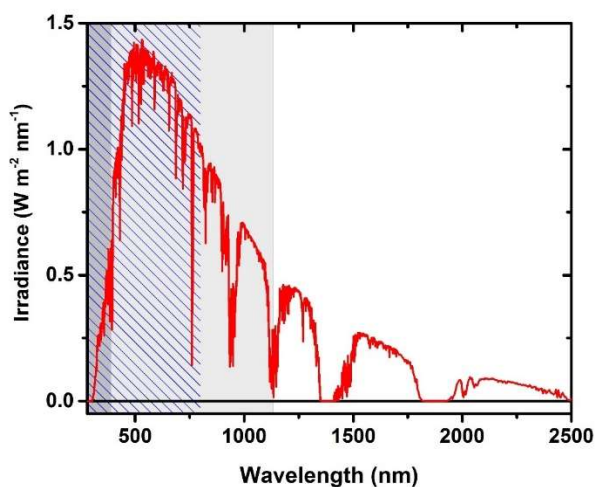


Figure 1.3: Solar irradiance A.M. 1.5. The area shaded light gray can be absorbed by Si, while the dark gray can be absorbed by both Si and anatase TiO₂. The dashed blue lines represent the spectral response observed for a TiO₂ thin film sensitized with a champion Ru complex.²⁸

as the semiconductor of choice due to its low cost, low toxicity, and wide availability.³⁰ Some of these initial studies used Ru(bpy)₃²⁺ physisorbed onto planar TiO₂ electrodes as means of sensitization. These interactions are relatively weak, meaning that the sensitizer can readily desorb from the interface under relatively benign conditions. The planar TiO₂ electrodes also did not provide a significant path length for light absorption, which led to low photocurrents. The Ru(bpy)₃²⁺ sensitizer was eventually replaced with a Ru sensitizer bearing a carboxylic acid derivative, [Ru(bpy)₂(dcb)]²⁺ (dcb = 4,4'-dicarboxylic acid 2,2'-bipyridine) which can chemically bind, or anchor, to the TiO₂ interface and greatly improve the device stability.³¹ The monolayer of sensitizers eventually gave way to thick films of sensitizer. Despite the slightly improved light absorption, light-to-current efficiencies were still less than 0.05%.³²

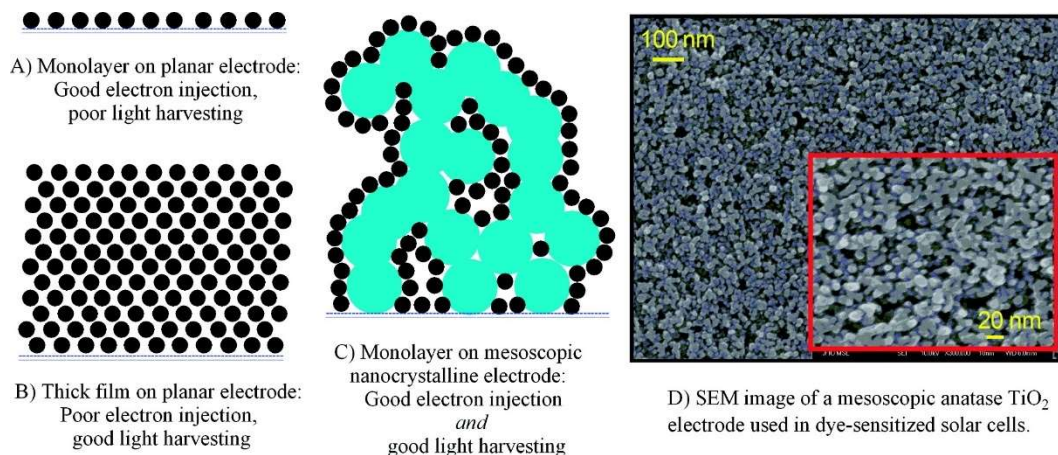


Figure 1.4: Representation of the advancements in DSSCs. Taken from Ref 27

A major breakthrough for this technology occurred in 1991, when O'Regan and Gratzel combined a sensitized mesoporous thin film of TiO_2 nanocrystallites with an organic electrolyte containing the I^-/I_3^- redox couple, **Figure 1.4**.³³ Light harvesting efficiencies of 7.12% were reported under full solar illumination, representing a significant technological leap. Within several years, devices achieving 9% efficiencies were realized. Within the past five years, devices exceeding efficiencies of 13% have been reported.^{34,35}

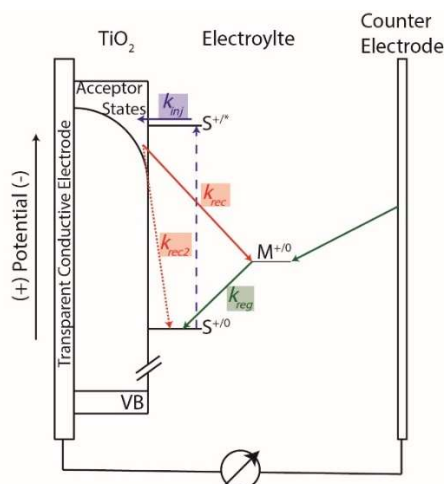


Figure 1.5: Schematic representation of a dye sensitized solar cell. In this figure, S is the surface anchored sensitizer, while M is the solution phase redox mediators. The injection, k_{reg} , sensitizer regeneration, k_{reg} and recombination reaction to the redox mediator, k_{rec} , or oxidized sensitizer, k_{rec2} , are shown.

A schematic representation of a DSSC is shown in **Figure 1.5**. A typical DSSC is comprised of a sensitized nanocrystalline TiO₂ photoanode and a platinized counter electrode with a liquid electrolyte junction between them. As mentioned, light harvesting is achieved through light adsorption by a surface-anchored chromophore, which undergoes an excited-state electron transfer to the acceptor states in the TiO₂, k_{inj} . The electron transfer event is reported to occur between 20 – 250 fs³⁶, though evidence for slower injection extending into the ps range under certain conditions does exist.³⁷ Ideally, the oxidized sensitizer is rapidly regenerated by a solution phase redox mediator, which can then transport the oxidizing equivalent, or “hole”, through the external electrolyte solution to the counter electrode. The prototypical redox mediator is based on the I⁻/I₃⁻ redox couple. The efficacious of this system as a redox mediator is often attributed to its complicated redox chemistry that impedes electron recombination from the TiO₂.^{38,39} Despite this, there are several drawbacks to this system including its fixed energetics and caustic nature. Significant progress has recently been made in developing alternative redox mediators that are both energetically tunable and less caustic.^{34,35,40–42} Of particular note are those based upon Co(bpy)₃^{3+/2+} that have seen broad adoption in recent years^{43–49}, and were used in the current record energy-to-light harvesting efficiency DSSC.³⁴

For the energy in an absorbed photon to be harvested, the injected electron must be collected at the back contact without recombining with an oxidized sensitizer or redox mediator during diffusion through the TiO₂. These recombination reaction results in the loss of the captured photon’s energy, lowering the light harvesting efficiency of the device. Overcoming this unwanted charge recombination process represents a significant obstacle in the development and optimization of DSSCs.

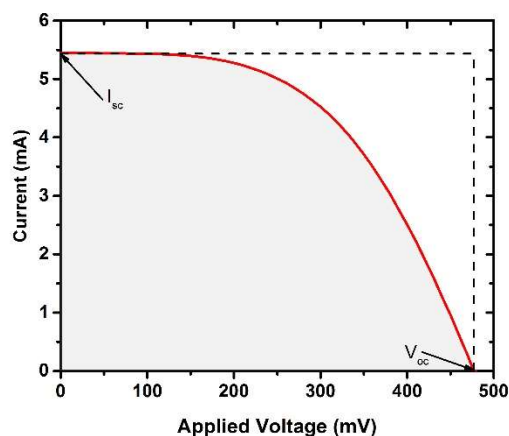


Figure 1.6: Representative current-voltage (iV) plot.

The current-voltage response of an illuminated functional DSSC device can be used to determine its overall light harvesting efficiency, η , using **Equation 1.1**. In this equation, i_{sc} is the short circuit current, V_{oc} is the open circuit voltage, FF is the fill factor, P_0 is the light flux incident on the sample and A_{cell} is the cell area. A representative curve can be seen in **Figure 1.6**.

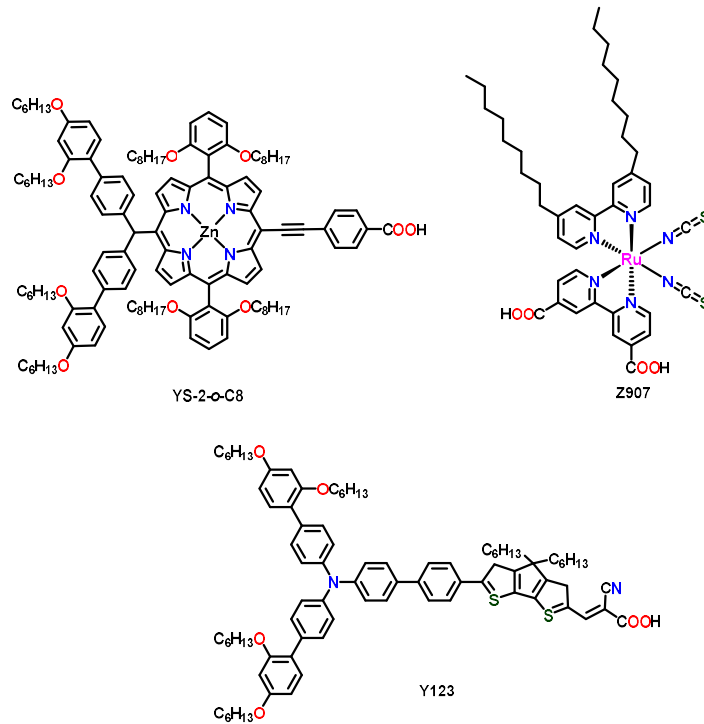
$$\eta = \frac{i_{sc}V_{oc}FF}{P_0A_{cell}} \quad (1.1)$$

The parameters in this equation report on underlying chemical processes occurring during DSSC operation. For example, i_{sc} reports on the kinetic aspects of a DSSC. Light absorption and electron injection efficiencies are thought to be the primary contributors to this value. However, it is worth noting that the diffusion of the redox mediator can limit this parameter, as has been reported for $\text{Co}(\text{bpy})_3^{3+/2+}$ based redox mediators.^{50,51} Significant effort has been made over the years towards developing panchromatic molecules that can sensitize TiO_2 from the visible to the NIR, which has improved i_{sc} .^{38,52} Examples of champion sensitizers are given in **Scheme 1.1**.^{34,38} Modern sensitizers contain a functional group which is used to anchor the

sensitizer to the TiO₂ interface. The most commonly used functional groups are carboxylic acids, though alcohols, phosphonic acids and others have been used with varying degrees of success.^{38,53,54}

The open circuit voltage represents the maximum Gibbs free energy that can be extracted from the cell, and is often represented as the energetic difference between the reduction potential of the redox mediator and the quasi-Fermi level of the TiO₂. The V_{oc} is ultimately determined by the recombination rate, since the quasi-Fermi level under these conditions is related to the number of injected electrons present in the TiO₂. The so-called

Scheme 1.1: Commonly used champion sensitizers.



diode equation, **Equation 1.2**, relates V_{oc} to the electron injection flux, I_{inj} , the sum of the recombination rate constants, k_i , to the concentration of acceptors, $[A]_i$.⁵⁵

$$V_{oc} = \left(\frac{kT}{e} \right) \ln \left(\frac{I_{inj}}{n \sum k_i [A]_i} \right) \quad (1.2)$$

Despite the importance of this reaction and significant effort in understanding it⁵⁶⁻⁶¹, a derivation of **Equation 1.2** does not exist and the factors that control V_{oc} are poorly understood.

The remainder of this chapter will highlight several key aspects of DSSC operation, which will be important throughout the subsequent chapters. These topics are: (1) Interfacial electric fields; (2) Charge mobility; and (3) Charge Recombination.

1.2.1 Interfacial Electric Fields

For a number of years, electrons injected into the TiO₂ substrate were thought to have a minimal effect on the anchored sensitizer and surrounding electrolyte solution due to the large dielectric constant of the substrate and the high ionic strength of the electrolyte.^{62,63} In 2010, transient absorption studies performed on sensitized TiO₂ thin films by Meyer et al. and Hagfeldt et al. showed this assumption to be incorrect.^{64,65}

Nanocrystalline TiO₂ thin films can be reduced by the application of a forward (negative) electrochemical bias, yielding TiO₂(e⁻). Reduced TiO₂ nanocrystallites are known to have a broad spectral absorption that spans the visible and the NIR.^{66,67} A study Ardo et al. looked at the effect of TiO₂ reduction on the photophysical properties of surface anchored sensitizers. The spectral features of the sensitizer Ru(dtb)₂(dcb)²⁺ (dtb = 4,4'-di-*tert*-butyl-2,2'-bipyridine and dcb = 4,4'-di-carboxylic acid-2,2'-bipyridine) were found to hypsochromically shift as the TiO₂ film became reduced, **Figure 1.7**.⁶⁴ These shifts were later attributed to a so called electric field, or “Stark” effect by comparison to spectra generated through classical Stark spectroscopy.⁶⁸⁻⁷⁰ The Stark effect occurs when a molecule is placed the presence of a strong electric field.^{71,72} The electric field interacts with the electronic or vibration transitions of the molecule, causing shifts that are dependent on the orientation of the molecular dipole

moment change relative to the electric field. Transitions which are aligned with the electric field will become more favored and shift to lower energies, while transitions which are antiparallel with the electric field will shift to higher energies.^{69,71,72} Unlike traditional Stark spectroscopy, where measurements are taken on isotropically orientated molecules in a frozen/rigid medium^{69,70}, the Ru sensitizers are all aligned normal to the surface and thus interact with the electric field in the same manner. This results in a unidirectional absorbance shift, rather than a broadening effect which is more typically observed.

A similar spectral feature was observed for this Ru sensitizer during transient absorption measurements. These features are most clearly seen after sensitizer regeneration by a redox mediator that is present in the external electrolyte. This demonstrated that the injected electrons can generate significant electric fields that can interact with the sensitizer and the external electrolyte solution. Hagfeldt et al. found similar spectral features for organic triphenylamine based sensitizers⁶⁵, extending the observation of the Stark effect to another class of sensitizers.

Ruthenium polypyridyl complexes anchored at TiO₂ interfaces can probe the field strength generated by the electrons. The observed shift in the sensitizer's absorbance is can be related to the dipole moment change of the sensitizer and the magnitude of the electric field. Assuming that both the molecular dipole moment and the electric field are normal to the interface, **Equation 1.3** can be used to determine the electric field magnitude.⁷³ This equation relates the absorption shift ΔA to the magnitude of the electric field change $\Delta \vec{E}$, by using a numerically determined first derivative of the ground state absorption profile, $\frac{dA}{d\nu}$. In this equation $\Delta \vec{\mu}$ is the change in molecular dipole moment between the ground and excited state.

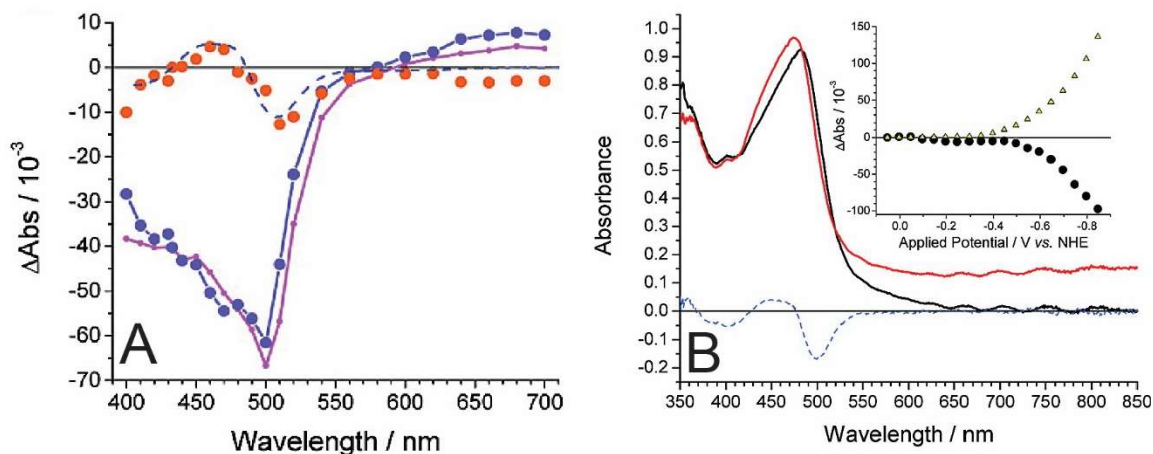


Figure 1.7: (A) Shown in orange are the residuals seen after spectral modeling of the raw data (purple) (B) Similar spectral feature observed after application of an electrochemical bias. Figures adapted from Ref 64.

$$\Delta A = \frac{dA}{d\nu} \frac{\Delta \vec{\mu} \Delta \vec{E}}{hc} \quad (1.3)$$

The molecular dipole moment change can be determined through traditional Stark spectroscopy, as demonstrated by Boxer⁶⁹, or through density functional theory.^{74,75} Using the sensitizer $\text{Ru}(\text{dtb})_2(\text{dcb})^{2+}$ as a probe, the magnitude of the electric field change under normal DSSC operating conditions has been estimate to on the order of ~ 1 mV/cm.⁷⁶ These electric fields can have a significant impact on the dynamics occurring at sensitized semiconductor interfaces, and the implications of these fields on DSSC performance has received considerable attention.^{76,59,73,74,77–80}

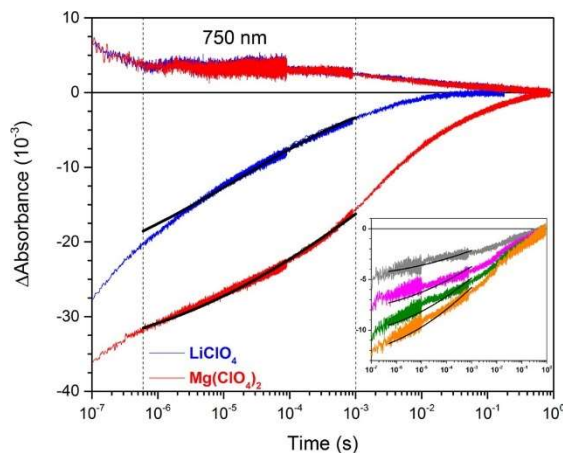


Figure 1.8: Transient absorption data where the electrons in the substrate were monitored at 750 nm, as well as features associated with the Stark effect. The Stark effect clearly decays in a region where there is minimal electron loss. Data taken from Ref 76.

Electrolytes used in DSSCs contain high concentrations of ions, which one would expect to interact with the fields generated by the injected electrons. In a study by O'Donnell et al., the spectral features for the Stark effect were monitored in relation to charge recombination for sensitized TiO₂ films immersed in acetonitrile solutions containing Li⁺ or Mg²⁺ iodide salts. The iodide was present to regenerate the sensitizer, allowing the Stark effect to be seen more clearly and to prolong the charge separated state. A key observation made during these experiments was the decay of the Stark effect (absorbance bleach) prior to significant recombination (absorbance at 750 nm), **Figure 1.8**.⁸¹ This was surprising, as both decay processes should occur concurrently, since the electrons generating the field would be depleted during recombination. The Stark effect decay was seen to be dependent on the cations in the electrolyte, and thus it was surmised that the cations in solution migrate towards the interface in the presence of the electric field, thereby reducing the electric field's influence on the surface anchored sensitizer. This effect, known as charge screening, has since been seen for both a larger series of Lewis acidic cations (Na⁺, Li⁺, Mg²⁺ and Ca²⁺)⁷⁶ and for ionic

liquids.⁸² The cation size-to-charge ratio can have an influence on both the magnitude and the rate of screening. Smaller cations such as Na^+ and Li^+ screen more rapidly than larger cations such as Mg^{2+} and Ca^{2+} , though a larger magnitude screening effect have been seen for the divalent cations under steady state conditions.^{76,59} More recently, Sampaio et. al demonstrated that in the absence of cations (i.e. neat acetonitrile), the Stark effect decayed concurrent with charge recombination, agreeing with expectations.⁷⁴

1.2.2 Electron Transport

Efficient transport of charges through a DSSC is of paramount importance to the light harvesting efficiency. Early on, electrons were thought to only be transported through the TiO_2 conduction band and by the redox mediator present in the electrolyte. This changed in 1998, when Bonhôte et al. first reported that tri-phenylamine (TPA) surface functionalized mesoporous thin films of TiO_2 could be reversible oxidized.⁸³ This was surprising, as the $\text{TPA}^{+/0}$ reduction potential fell within the bandgap of TiO_2 , meaning that the oxidation of the TPA could not occur *through* the TiO_2 (as in through the CB), but rather *across* the TiO_2 by either a self-exchange electron transfer reaction or by physical diffusion by the TPA. To investigate the specific mechanism of transport, the surface coverage was systematically varied and the percentage of the films that was oxidable was monitored. A key finding was that the TPAs could not be oxidized below a certain surface coverage. This observation, termed a percolation threshold, demonstrated that electron transfer occurred through a lateral electron self-exchange, rather than the physical movement of the molecules across the surface. An example of this is found in Figure 1.9. The latter should have allowed for complete oxidation of the functionalize film at all surface coverages investigated.^{84,85} The percolation threshold was later observed for ruthenium and osmium polypyridyl complexes by Trammel et. al.⁸⁶

Understanding these self-exchange reactions has garnered significant interest in recent years.^{87–}

94

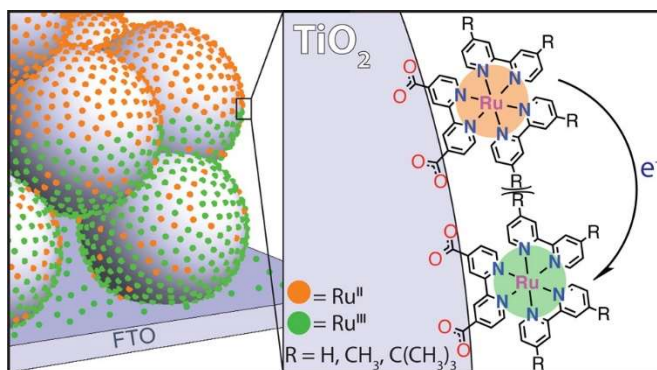


Figure 1.9: Lateral electron self-exchange between surface anchored Ru chromophores. Adapted from Ref 95.

The electron/hole mobility across the surface is likely governed by similar factors as solution phase self-exchange electron transfer.⁹² Molecular structure has been shown to greatly impact the electron transfer rate. For example, the inclusion of thiocyanate ligands onto a ruthenium polypyridyl compounds (example Z907 in **Scheme 1.1**) increases the self-exchange rate relative to similar sensitizers without the thiocyanate present.⁹⁶ This is thought to be a result of increased electronic coupling between adjacent compounds. Solvent has also been shown to play an important role during the lateral self-exchange, likely due to the outer sphere reorganization energy component of self-exchange.^{94,97} The implications of this electron transfer event on the charge recombination is poorly understood. Self-exchange has been shown to be active on the timescale of charge recombination, as has demonstrated through several time resolved techniques.^{88–90,98} How this influences charge recombination is currently unknown, but is of significant interest. More recently, a functional DSSCs which rely solely on this lateral-exchange process for transport of the hole to the counter electrode have been reported⁹⁹, representing a new and interesting approach for the production of DSSCs.

The electron accepting states in mesoporous nanocrystalline TiO₂ play a pivotal role during charge transport. The electron accepting states in nanocrystalline semiconductors are often modeled as localized states rather than the conduction bands of single crystal semiconductors.^{76,100} The chemical identity of these states is not well understood, though many postulate that these are lower energy trap states caused by oxygen vacancies.^{101–104} The energetic position of these states can be tuned by additives in the external electrolyte solution. For example, it has been well document that the conduction band of metal-oxide films shift by 59 mV/pH when submerged in aqueous electrolytes.^{67,105,106} Lewis acidic cations in acetonitrile solutions can also cause a shift in acceptor states, though the magnitudes have not been quantified so as to give a shift per concentration change.⁷⁶ A shift towards positive energies (i.e. away from the vacuum) often increases the excited state orbital overlap of the sensitizer and electron accepting states in the substrate, thereby improving charge injection.^{63,107} This can be seen in the photoluminescence quenching of Ru sensitizer anchored at TiO₂ interfaces after the introduction of Lewis acidic cations such as Li⁺.^{76,108} It is worth noting that the bandgap is not observed to change with changing pH or the addition of cations, meaning the valence and conduction band-like states move in concert.

Electrons injected into TiO₂ localize within this distribution of electron accepting states. In order to diffuse though the TiO₂, these electrons must move between states, which can reside at higher or lower energies. Two mechanisms that are commonly invoked to describe this transport process are the so-called continuous-time random walk (CTRW) model^{60,109} and a random time of flight (RTF) model^{110,111}. Both model proposes that the injected electron becomes trapped within a localized state, and that the transport of the electron is limited by the rate of release from these states. The key difference between the two is that the CTRW model

assumes that electrons can only jump to their nearest neighbor, while the RTF model inserts a tunneling effect that places equal jump probabilities on all the localized states in the TiO_2 . Although similar, the trapping-detrapping rates was orders of magnitude slower for RTF relative to CTRW. Several other models account for electron transport have also been proposed^{112,113}, though these two models have found the most broad application within the field.

The mobility of charge has a strong influence on device performance. Slow electron diffusion can lead to reduced charge collection, as charge recombination becomes more competitive. Until recently, the mobility of charge across the interface was not thought to significantly alter device performance. However, there is growing evidence that electron mobility across the surface can influence charge recombination and therefore device performance.^{94,97} The implications of charge mobility on recombination will be discussed in the next section.

1.2.3 Charge Recombination

The recombination reaction between injected electrons and molecular acceptors represents an unwanted electron transfer reaction that lowers the light harvesting efficiency of DSSCs. Understanding and impeding these unwanted reactions has been the focus of numerous studies^{56,38,44,111,113–120}, but despite this, interfacial electron transfer reactions remain poorly understood. An experimental difficulty is relating the observed rate constants, abstracted from time resolved kinetic data, to the actual interfacial electron transfer step. Recombination kinetics are dispersive, stretching from the nanosecond to the microsecond timescales and beyond. A number of explanations have been given to explain the slow recombination kinetics, including the reaction occurring in the Marcus inverted region^{121–123} and/or that the kinetics

dominated by electron/hole transport discussed above.^{124–126} Though often difficult to understand, the charge rectification imparted by the large discrepancy in the electron injection rate versus that for charge recombination ultimately allows for efficient charge separation and DSSC performance.

Common approaches to modeling charge recombination kinetics are to use a sum of exponential functions¹²⁷ or a stretch exponential function, also known as the Kohlraush-Williams-Watts function (KWW)^{56,128,129}, **Equation 1.4**. The time required for half the injected electrons to recombine, $t_{1/2}$, are often reported in lieu of kinetic modelling.⁵⁸

$$\Delta A = \Delta A_0 e^{-(k t)^\beta} \quad (1.4)$$

Even with extensive kinetic modeling the abstracted rate constants often give little insight into the recombination mechanism.³⁸ The initial reaction conditions can greatly influence the abstracted rate constants requiring systematic studies, where only a single parameter is intentionally varied, in order to gain meaningful insights into the recombination mechanism.

It is worth noting that a study published by Kelly et al. saw that recombination kinetics between TiO₂ and an oxidized Ru sensitizer followed an second-order equal-concentration kinetic model.¹⁰⁸ A single rate constant was abstracted from concentration dependent kinetic data. Although there are reports of this second-order kinetic model being utilized by other¹²³, it has not been broadly adopted by the field. In one recent study, Brigham and Meyer monitored charge recombination when an electrochemical bias was applied to sensitized TiO₂ electrodes.⁵⁶ The electrochemical bias was used to establish either an excess of oxidized sensitizer or electrons in the substrate. This was used to create pseudo-first order conditions for either participant, so that the reaction order could be determined. The kinetics were modeled

with a KWW function. The concentration of electrons when the oxidized sensitizers were in excess was varied through the laser intensity and its influence on recombination was quantified. The reaction was found to be first order in electrons. The recombination reaction was also found to be first order in oxidized sensitizer when the oxidized sensitizer was in excess.

The application of a light or electrochemical bias can have a significant influence on the recombination rate,^{58,117,119,130–132} with important ramifications for functional DSSCs. There are expected to be ~ 20 electrons in each nanocrystallite at the power point condition.^{117,133} Under these conditions, Hu et al. showed that the increased charge recombination rates under these conditions leads to incomplete sensitizer regeneration in functional DSSCs that decreases the devices V_{oc} .¹¹⁷ The connections between electron concentration and the rate of recombination has led to the development of different recombination models that attempt to rationalize interfacial electron transfer behavior.

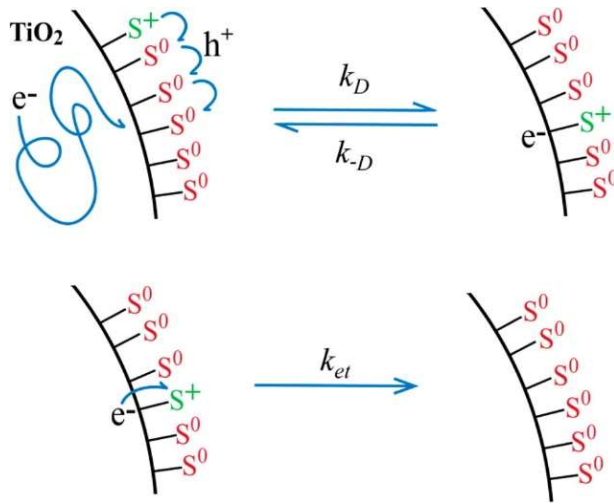


Figure 1.10: Contributions from both the charge carrier diffusion thought/across the TiO₂ and the electron transfer event on the overall rate of recombination. Figure adapted from Ref 56.

The increased rate and less dispersive recombination kinetics reported by Durrant et. al has been used to develop several models for charge recombination. These models involve both electron diffusion through the TiO₂, invoking a trap/detrapping model, and kinetic parameters governing the electron transfer event.^{60,101} Electron transfer reactions that are limited by diffusion are known to follow **Equation 1.5**, where k_{obs} is the observed electron transfer rate constant, k_D is the diffusion coefficient, k_{et} is the intrinsic electron transfer rate constant and K is an equilibrium, $K = k_D/k_{-D}$.⁵⁶ As diffusion becomes slow relative to k_{et} , the reaction is dominated by diffusion, **Figure 1.10**. Understanding the diffusional components for charge recombination would likely lead to better insights into interfacial electron transfer.

$$\frac{1}{k_{obs}} = \frac{1}{k_D} + \frac{1}{Kk_{et}} \quad (1.5)$$

A study Farnum et al. reported charge recombination on sensitized indium doped tin oxide (ITO) nanocrystalline thin films.¹³⁴ Unlike TiO₂, ITO is metallic in nature without a forbidden energy gap, i.e. bandgap, between the valence and conduction bands. This allows rapid electron transport. The recombination processes for these films were monitored over a series of applied potentials, with the difference between the applied potential and the Ru^{3+/2+} reduction potential was taken to be the driving force for the reaction. The rate constants found followed Marcus-Gerischer theory. It is likely that similar kinetics would be observed for TiO₂ films if the diffusional contribution to recombination was eliminated or minimized.

Ultimately, charge recombination represents an unwanted process in DSSCs. Several tactics have been employed to slow charge recombination. Surface passivation with insulating layers applied by atomic layer deposition represents one of the most prevalent methods.^{135–137}

Molecular approaches have also been employed to slow recombination to molecular sensitizers^{22,53,90,116,138,139} Extending the distance between the TiO₂ and the sensitizer can also slow charge recombination,^{89,138} but may also lower the quantum yield for electron injection, as the increased distance lowers electronic coupling between the excited-sensitizer and the TiO₂.^{37,140} To avoid this, dyad systems are often employed, where a sensitizer is covalently linked to an electron donating moiety. After injection, the sensitizer rapidly transfers the hole to the acceptor, increasing the distance between the acceptor and the interface.^{90,118} In some cases, this approach can greatly slow charge recombination relative to simple sensitizer systems. Molecular bridges between the donor and acceptor were recently shown to influence recombination, suggesting a through bond recombination mechanism.¹¹⁸

1.3 Conclusions

Numerous electron transfer and transport processes govern the overall efficiency of a DSSC. This thesis is focused on the fundamental electron transfer processes that underlie DSSC operation. Through this research, we have gained a deeper understanding of the electron self-exchange reaction TiO₂ interfaces, the role of cations on charge recombination to solution and surface anchored mediators as well as fundamental aspects of interfacial electron transfer.

Chapter 2: A Distance Dependence to Lateral Self-Exchange Across Nanocrystalline TiO₂. A Comparative Study of Three Homologous Ru^{III/II} Polypyridyl Compounds

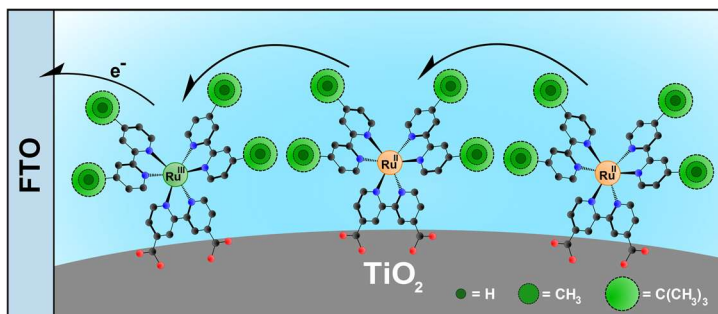
Reprinted with Permission from DiMarco, B. N.; Motley, T. C.; Balok, R. S.; Li, G.; Siegler, M. A.; O'Donnell, R. M.; Hu, K.; Meyer, G. J. *J. Phys. Chem. C* **2016**, *120* (26), 14226-14235.
Copyright 2016 American Chemical Society

2.1 Introduction

Studies as far back as 1998 have demonstrated that molecules anchored to the mesoporous nanocrystalline (anatase) TiO₂ thin films commonly used in dye-sensitized solar cells can be reversibly oxidized and reduced in standard electrochemical cells.^{83,141} Molecules with formal reduction potentials that lie within the forbidden 3.2 eV band gap of TiO₂ are rapidly and quantitatively oxidized indicating that the redox chemistry does not involve the conduction or valence bands. Instead a model was proposed wherein electron transfer was initiated at the transparent conductive oxide substrate that supports the thin film and continues across the TiO₂ nanocrystallites by lateral intermolecular self-exchange electron transfer, now commonly referred to as ‘hole hopping’.^{83,142} A simplified description of Ru^{III/II} self-exchange for three Ru compounds linked to a single TiO₂ nanocrystallite on a fluorine-doped tin oxide (FTO) substrate is given in **Scheme 2.1**. A more realistic description would display about 500 Ru compounds anchored to each ~ 20 nm anatase crystallite interconnected in an ~ 5-micron thin film. The importance of self-exchange electron *transfer* between surface immobilized molecules is that it provides a means to *transport* charge across nanocrystalline surfaces

without a loss of free energy. In this chapter, it is shown for the first time that such transport can be controlled at the molecular level with insulating organic functional groups.

Scheme 2.1: Illustration of lateral intermolecular self-exchange electron transfer across anatase TiO₂ nanocrystallites initiated at the fluorine-doped tin oxide (FTO) substrate.



It was previously found that a minimal surface coverage of the redox active molecules was required for complete oxidation and reduction.⁸³ At least 50% of the saturation (often assumed to be a monolayer) surface coverage was necessary to ensure that all of the surface anchored molecules could be electrochemically accessed.^{83,86} This minimum surface coverage, termed a percolation threshold, helped demonstrate that oxidation occurs through electron self-exchange, rather than physical diffusion of the anchored molecules. More recent chronoamperometric studies have provided apparent electron diffusion coefficients (D) for lateral self-exchange for a growing number of redox active molecules.^{87,89,90,92,93,142,143} From this prior work, it is clear that self-exchange dynamics on TiO₂ nanocrystallites can, in some particular cases, be controlled at the molecular level. For example, the inclusion of two isothiocyanate groups in a *cis*-geometry about the ruthenium center has been demonstrated to significantly increase D .⁸⁷ However, the extent to which self-exchange rate constants, and hence charge transport, across nanocrystalline surfaces can be controlled by molecular structures remains uncertain. This is unfortunate as recent studies have shown that dye-

sensitized solar cells do not require mediators such as iodide, and can instead use self-exchange electron transfer to complete the circuit and generate electrical power.⁹⁹ Lateral self-exchange also has relevance for the photo-oxidation of water to oxygen by molecular catalysts.^{142,144} This manuscript seeks to identify structure-property relationships for self-exchange ‘hole hopping’ in a family of three Ru polypyridyl compounds.

Non-adiabatic Marcus theory has been extensively used to quantify or predict electron-transfer rate constants and has been thoroughly reviewed.^{145,146} Non-adiabatic Marcus theory is commonly used to describe self-exchange electron-transfer reactions between weakly coupled donors and acceptors in homogenous fluid solutions. A generic potential energy diagram for self-exchange electron-transfer is shown in **Figure 2.1**. A key feature of self-exchange electron-transfer reactions is that $\Delta G^\circ = 0$, due to the equivalence of the products and reactants. The reactant and product surfaces are split at their intersection by $2 H_{AB}$, the electronic coupling matrix element. For outer-sphere bimolecular self-exchange in fluid solution, coupling in the encounter complex is weak, $H_{AB} \ll kT$. Constraining molecules undergoing exchange electron transfer to a surface is expected to further decrease H_{AB} justifying the use of non-adiabatic Marcus theory.

The self-exchange electron transfer rate constant, k_{SE} , is described by **Equation 2.1**.

$$k_{SE} = \left(\frac{2\pi}{\hbar} \right) \left(\frac{|H_{AB}|^2}{\sqrt{4\pi\lambda k_b T}} \right) \exp \left(-\frac{\lambda}{4k_b T} \right) \quad (2.1)$$

This equation relates k_{SE} to temperature (T), H_{AB} , and the total reorganization energy (λ) for the reaction. The total reorganization energy is related to the free energy of activation (ΔG^\ddagger) $= \lambda/4$ and is typically partitioned into inner sphere, λ_I , and outer sphere, λ_O components, $\lambda = \lambda_I + \lambda_O$. Inner-sphere reorganization reflects changes in bond lengths and angles that accompany

electron transfer while λ_o reflects reorientation of the solvent molecules and ions present in the electrolyte.

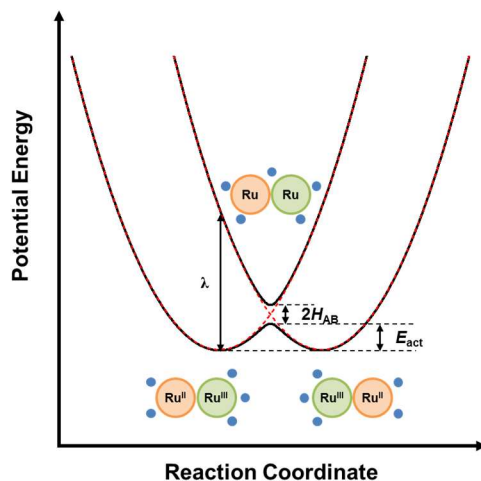


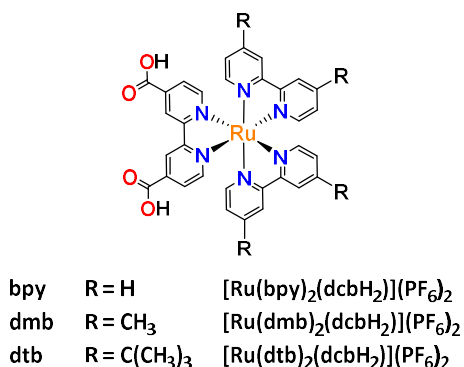
Figure 2.1: Plot of an example one-dimensional reaction coordinate for a nonadiabatic (dashed lines) or adiabatic (solid lines) self-exchange electron transfer reaction. The orange and green spheres represent Ru molecules in the encounter complex before, during, and after electron transfer. The blue spheres depict counter ions and exaggerates their location and movement during the electron transfer process.

The state-of-the-art in characterization of lateral self-exchange in mesoporous TiO_2 thin films was recently reported by Moia and coworkers.⁹² These authors quantified self-exchange among ten different dye molecules as a function of temperature for the first time. Self-exchange was found to be an activated process with E_{act} that ranged from 170-370 meV, values that were dependent on the nature of the redox active molecule. Marcus analysis λ and H_{AB} for self-exchange in macrocyclic, ruthenium polypyridyl, and organic push-pull (i.e. D- π -A) molecules. The λ 's abstracted from the transient kinetic data were found to be in good agreement with expectations based on density functional theory. Reorganization energies associated with highly delocalized frontier orbitals and rigid molecular structures with

extended conjugation were concluded to be small. There was also some evidence that non-conjugated functional groups on the molecules could potentially influence lateral self-exchange. This report compliments this previous study through characterization of a homologous series of compounds where λ is expected to be held near parity, yet the steric bulk of the bipyridine ligand was intentionally varied. The data provide compelling evidence that these side groups can be used to tune the self-exchange between immobilized redox sites.

In this chapter, a comparative study of three analogous Ru diimine compounds of the general form $[\text{Ru}(\text{LL})_2(\text{dcbH}_2)](\text{PF}_6)_2$ where dcbH_2 is 2,2'-bipyridyl-4,4'-dicarboxylic acid and LL is 2,2'-bipyridine (**bpy**), 4,4'-dimethyl-2,2'-bipyridine (**dmb**), or 4,4'-di-*tert*-butyl-2,2'-bipyridine (**dtb**), is reported, **Scheme 2.2**. These compounds share a tris-chelated, pseudo-octahedral geometry and hence the reorganization energy for the $\text{Ru}^{\text{III/II}}$ redox chemistry is expected to be approximately the same across the series. Each compound possesses a single dcb ligand for surface binding to TiO_2 with two other substituted bipyridine ligands possessing substitutions at the 4,4'-position that were expected to influence lateral self-exchange reactivity. In fact, small changes to the molecular structure, such as replacement of a H atom with a methyl group, was found to have a surprisingly large influence on the D , as observed through both chronoabsorptometry and temperature-dependent cyclic voltammetry studies.

Schemes 2.2. Chemical Structure of the Molecules Used in this Hole Hopping Study



2.2 Methods

Materials. The following solvents and reagents were purchased from the indicated supplier, and were used without further purification: titanium(IV) isopropoxide ($\text{Ti}(i\text{-OPr})_4$; Aldrich $\geq 97.0\%$); deionized water; acetonitrile (CH_3CN , Burdick & Jackson, spectrophotometric grade); diethyl ether (Et_2O ; Fisher Scientific, 99.9%); anhydrous ethanol (EtOH , Fisher Scientific, 99%); silver nitrate (AgNO_3 ; Stream, 99.9%); sodium hydroxide (NaOH ; Sigma-Aldrich, $>97\%$); hexafluorophosphonic acid (HPF_6 ; 65% solution in H_2O , Sigma-Aldrich); lithium perchlorate (LiClO_4 ; Sigma-Aldrich 99.99%); ammonium hexafluorophosphate (NH_4PF_6 ; Sigma-Aldrich, 99.8%); 4,4'-dimethyl-2,2'-bipyridine (*dmb*; Combi-Blocks), argon (Airgas, $\geq 99.998\%$); oxygen (O_2 , Airgas, $\geq 99.998\%$); fluorine-doped tin(IV) oxide (FTO; Hartford Glass Co., Inc., 2.3 mm thick, $15\ \Omega/\square$), $[\text{Ru}(\text{bpy})_2(\text{dcbH}_2)](\text{PF}_6)_2$ (**bpy**; Solaronix). The complexes $[(p\text{-cymene})\text{Ru}(\text{deeb})\text{Cl}]\text{Cl}$, where *deeb* is the 2,2'-bipyridyl-4,4'-diethyl ester, and $[\text{Ru}(\text{dtb})_2(\text{dcbH}_2)](\text{PF}_6)_2$ (**dtb**) were available from previous studies.^{147,148} Anion metathesis of **dtb** was used to generate a ClO_4^- salt. Single crystals of the perchlorate salt of **dtb** suitable for X-ray structure determination were obtained by slow diffusion of hexanes into concentrated acetonitrile solutions.

Synthesis. $[\text{Ru}(\text{dmb})_2(\text{deeb})](\text{PF}_6)_2$ (**1**): The $[(p\text{-cymene})\text{Ru}(\text{deeb})\text{Cl}]\text{Cl}$ (80.1 mg, 0.13 mmol) precursor was combined with *dmb* (49.0 mg, 0.27 mmol) and AgNO_3 (61.6 mg, 0.36 mmol) in 10 mL of EtOH . The solution was purged with N_2 for >15 minutes, then heated to a reflux under an N_2 atmosphere for 14 h. After this time had elapsed, the solution was cooled to room temperature and the solvent was removed. The colored product was redissolved in a minimal amount of water. The aqueous solution was filtered to remove any remaining Ag^+ salts. To the filtrate was added an excess of NH_4PF_6 , which yielded a brown solid. The solid

was filtered and dissolved in dichloromethane to prevent any remaining Ag^+ salts from being carried forward. The solvent was removed, and the product was dissolved in CH_3CN . Slow diffusion of Et_2O into a concentrated CH_3CN solution afforded 128.3 mg of product as large brown crystals, which were suitable for X-ray structure determination. (Yield = 92%) ^1H NMR (400 MHz, CD_3CN) δ 9.00 (s, 2H), 8.334(d, J = 6.2Hz, 4H), 7.94(d, J = 5.8Hz, 2H), 7.80(d, J = 5.9 Hz), 7.50-7.43 (M, 4H), 7.26-7.18(M, 4H), 4.24(q, J =6.9, 14.1, 4H) 2.52(d, J =9.92Hz, 12H), 1.41(t, J =7.1Hz, 12H) ^{13}C NMR (150 MHz, CD_3CN) δ 164.8, 159.2, 157.5, 154.0, 152.3, 152.1, 152.1, 151.8, 139.6, 129.7, 129.6, 127.6, 126.3, 124.8, 63.9, 21.6, 14.6. HS-ESI-MS: m/z = 915.1826 (calcd. for $\text{RuC}_{40}\text{H}_{40}\text{N}_6\text{O}_4\text{PF}_6$ $[\text{Ru}(\text{dmb})_2(\text{deeb})](\text{PF}_6)^+$: 915.1796); m/z = 385.1077 (calcd. for $\text{RuC}_{40}\text{H}_{40}\text{N}_6\text{O}_4$ $[\text{Ru}(\text{dmb})_2(\text{deeb})]^{2+}$: 385.1077).

$[\text{Ru}(\text{dmb})_2(\text{dcbH}_2)](\text{PF}_6)_2$ (**dmb**): $[\text{Ru}(\text{dmb})_2(\text{deeb})](\text{PF}_6)_2$ (60.9 mg, 57 μmol) and NaOH (9 mg, 230 μmol) were added to 30 mL of a 1:5 EtOH/ H_2O solution. The solution was purged with N_2 for >20 mins, then heated to reflux. The reflux was maintained for 15 h under a N_2 atmosphere, after which the solution was allowed to cool to room temperature. The solution volume was reduced, and the remaining the water was acidified with HPF_6 . The resultant solid was filtered, washed with Et_2O and H_2O , and left under vacuum overnight to dry. This afforded 51.1 mg of a reddish brown solid (Yield = 88.6%) ^1H NMR (500 MHz, CD_3CN) δ 9.52 (s, 2H), 8.33(d, J = 8.1Hz, 4H), 7.82(dd, J = 5.8, 21.5Hz, 4H), 7.48(dd, J = 5.8, 21.1Hz, 4H), 7.24(d, J = 5.2Hz, 2H), 7.17(d, J = 5.7Hz, 2H), 2.51(d, J = 14.2Hz, 12H) ^{13}C NMR (150 MHz, CD_3CN) 167.3, 159.4, 157.7, 157.6, 153.3, 152.2, 151.8, 129.62, 129.60, 128.0, 126.25, 126.22, 21.6. HS-ESI-MS: m/z = 859.1162 (calcd. for $\text{RuC}_{36}\text{H}_{32}\text{N}_6\text{O}_4\text{PF}_6$ $[\text{Ru}(\text{dmb})_2(\text{dcbH}_2)](\text{PF}_6)^+$: 859.1142); m/z = 357.0758 (calcd. For $\text{RuC}_{36}\text{H}_{32}\text{N}_6\text{O}_4$ $[\text{Ru}(\text{dmb})_2(\text{dcbH}_2)]^{2+}$: 357.0764)

Thin Film Preparation. Titania nanocrystallites were made by hydrolysis of $\text{Ti}(i\text{-OPr})_4$ via a previously published sol-gel technique.¹⁴¹ Thin, mesoporous films were cast through doctor blading onto an ethanol cleaned FTO substrate using Scotch tape ($\sim 50\ \mu\text{m}$ thick) as a spacer for consistent thickness. The films were first dried while covered for 30 min and then sintered at $450\ ^\circ\text{C}$ for 30 min under O_2 flow at $\sim 1\ \text{atm}$. Films were either used immediately or stored in an oven ($\sim 70^\circ\text{C}$) until use. Film thicknesses ($\sim 4\text{--}6\ \mu\text{m}$) were determined using a Bruker Dektak XT profilometer using the Vision 64 software.

Titania films were submerged into concentrated CH_3CN solutions of **bpy**, **dmb**, or **dtb** to allow the molecules to anchor to the nanocrystallite surface. Films were submerged for a minimum of 48 h to ensure saturated surface coverages. Prior to use, the films were soaked for $\sim 1\ \text{h}$ in neat CH_3CN to remove any weakly adsorbed molecules from the film in order to minimize dye desorption during the course of the experiments.

UV-Visible Spectroscopy. Steady-state UV-visible spectra were obtained on either Hewlett Packard 8453 photodiode array or Varian Cary 60 spectrophotometer at room temperature. All measurements were made in custom-made 1 cm pathlength quartz cuvettes with a 24/40 ground glass joint affixed to the top. Surface-functionalized films were placed along the diagonal of the cuvette at a 45° angle to the incident probe beam.

Electrochemistry. Electrochemical measurements were performed with a potentiostat (Bioanalytical Scientific Instruments model CV-50W or Epsilon electrochemical analyzer) using a standard three electrode arrangement. A surface-functionalized TiO_2 film was employed as the working electrode, while a platinum mesh was used as the auxiliary electrode. Potentials were applied against a non-aqueous silver wire pseudo-reference electrode (Pine Research Instruments), which was filled with 0.1 M LiClO_4 containing CH_3CN . Unless

otherwise noted, the pseudo-reference electrode was externally calibrated against the ferrocenium/ferrocene ($\text{Fc}^{+/0}$) reduction potential in 0.2 M LiClO_4 containing CH_3CN , where the $\text{Fc}^{+/0}$ potential is 0.31 V vs the saturated calomel electrode (SCE), and SCE is 0.241 V vs the normal hydrogen electrode (NHE).¹⁴⁹ The three electrodes were placed within a custom quartz cuvette, consisting of a 1 cm pathlength square quartz cuvette attached by ~8 cm of round glass tubing to a 24/40 ground glass joint, which allowed the TiO_2 film to be monitored spectroscopically. The electrode connections were fed through a rubber septum, which was used to seal the cuvette. For measurement taken at room temperature, the $\text{Fc}^{+/0}$ potential was measured before and after the experiment to ensure reference electrode stability.

Spectroelectrochemical measurements were used to quantify E° for TiO_2 anchored complexes. The experiment monitored the absorbance of the surface-functionalized TiO_2 film while applying increasingly positive electrochemical biases. The films were held at each potential for a minimum of 1 min, or until no additional spectral changes were observed, in order to ensure the film was equilibrated. Chronoabsorptometry (CA) was used to investigate the apparent diffusion coefficient, D , for the molecules studied. In contrast to the spectroelectrochemical experiment, a single oxidizing potential was applied to the film, and the oxidation rate was monitored spectroscopically as a function of time. Full oxidation of the film was achieved after stepping the potential to $E^\circ + 0.5$ V for several minutes. A new surface-functionalized film was used for each experiment to minimize the impact of dye desorption. All spectroelectrochemical experiments were performed in argon purged CH_3CN containing 0.1 M LiClO_4 as the supporting electrolyte.

Cyclic voltammetry (CV) was also used to investigate D for the surface bound compounds. Variable temperature CV experiments were performed within a custom cell comprised of a ~1

cm² square tubing attached to a 19/22 ground glass joint. The electrodes were arranged in a manner analogous to the CA experiments. The argon purge electrochemical cell was placed within a UniSoku CoolSpek USP-203-B liquid nitrogen cryostat, which allowed the temperature to be adjusted to ± 1 °C of the desired temperature. The apparatus was allowed to thermally equilibrate at each temperature for >10 min prior to performing the measurement. Again, a new film was used for each experiment. Note that D_{CV} and D_{CA} denote diffusion coefficients that were measured by CV or CA respectively.

Data Analysis. Kinetic modeling was performed in Origin 9.0, and least-squares error minimization accomplished by the Levenberg-Marquardt iteration method. Resulting values from the best fit are reported with the standard error from the fitting procedure. In the case of the CA measurements, the error reported is the standard deviation of multiple trials. Spectral modeling of the spectroelectrochemical data was performed a least squares fitting function written into a custom script in Mathematica 9

Calculation of c_0 and R . The ‘concentration’ of redox active molecules within the mesoporous TiO₂ thin films is an ill-defined parameter. To determine the volume concentration (cm⁻³), c_0 , and consequently, the intermolecular spacing between ruthenium compounds (cm), R , assumptions about the porosity of the film and close packed nature of the molecules were required. Below are presented methods to determine the upper and lower limits as well as one intermediate value of R .

Upper Limit of R . This approach represents an upper limit to R as the molecules are assumed to be distributed throughout both the TiO₂ nanoparticle and pore volume as opposed to the more reasonable situation where they are localized on the TiO₂ surface. Further calculations of R in this regime lead to upper limits for both self-exchange rate constant and

electronic coupling matrix element. To estimate c_0 and R , the surface coverage (mol/cm^2), Γ , was first determined with **Equation 2.2**, where A and ε are the absorbance and molar extinction coefficient ($\text{M}^{-1}\text{cm}^{-1}$) of the film at a given wavelength and 1000 is a factor to convert from L to cm^3 . Note that the wavelength used for each compound is the wavelength where the absorbance of the surface-functionalized TiO_2 film is the same in neat and 0.1 M LiClO_4 solutions in acetonitrile (*vide infra*). The extinction coefficient at the absorbance peak observed in fluid solution is assumed to be retained upon anchoring.

$$A=1000\times\varepsilon\times\Gamma \quad (2.2)$$

Next, Γ was converted to c_0 using **Equation 2.3**, where N is Avogadro's number and d is the film thickness (cm). The inclusion of $\cos(45^\circ)$ adjusts for the path length of the probe being incident to the film at a 45° . The Ru compounds were assumed to be distributed evenly throughout the total film volume.

$$c_0=\frac{\Gamma\times N}{d\times\cos 45^\circ} \quad (2.3)$$

Finally, to convert to R , the cubic lattice arrangement was assumed on the surface as was done previously by Daum, *et al.* for redox sites immobilized in polymer films¹⁵⁰ and by Moia, *et al.* for molecules anchored to TiO_2 films.⁹² This relation is given simply by **Equation 2.4**.

$$R=c_0^{-1/3} \quad (2.4)$$

Intermediate Value of R. For a more accurate value of R , the pore volume of the mesoporous TiO_2 film must be accounted for. In the present study, the films were assumed to have a $\sim 50\%$ porosity. In this method, the c_0 was calculated as it was in the upper limiting case.

To adjust for the pore volume, the c_0 was multiplied by a factor of two. This approximation still assumes that the Ru compounds are evenly distributed throughout the volume occupied by the TiO₂ nanoparticles, but now the volume has decreased by half which results in a doubling of the calculated concentration. R was calculated as before.

Lower Limit of R . The lower limit of R was estimated from crystal structures of the Ru molecules, where R represents the distance between the substituents in the 4 positions of the bipyridine group trans to one another (**Figure 2.2**). In order to carry out further calculations needed to determine the apparent diffusion coefficients from the CV experiments, **Equation 2.4** was used to calculate c_0 . This value gives an estimate for the spacing between molecules close to the van der Waals radii limit allowed by the compounds, and calculations based on these values lead to a lower limit for the self-exchange rate constant and electronic coupling matrix element.

2.3 Results.

Preparation of the [Ru(dmb)₂(deeb)](PF₆)₂ (**1**) precursor was achieved in high yield using a modified, previously reported procedure for the synthesis of similar ruthenium polypyridyl compounds.¹⁴⁷ Base catalyzed hydrolysis of the ethyl ester groups in **1** generated the desired carboxylic acid form of the compound, **dmb**. Structural identity was confirmed through ¹H and ¹³C NMR, and high-resolution mass spectroscopy.

Slow diffusion of Et₂O into concentrated CH₃CN solutions of **1** gave crystals suitable for X-ray diffraction (Figure 2). The average Ru-N distance is 2.054 Å. The Ru-N distance for the deeb ligand is slightly shorter than those for the dmb ligands, indicative of stronger back-bonding from the Ru non-bonding d-orbitals to deeb π^* orbitals. The average N-Ru-N bite

angle is 78.73° , while the bite angle for the deeb ligand is 0.5° smaller than the dmb ligand, consistent with the shorter Ru-N bond lengths for deeb ligand. The Ru compounds appear in pairs in the crystal structure through π - π interaction between the deeb ligands with an interlayer distance of 4.331 \AA . A weaker π - π intermolecular interaction with neighboring dmb ligands was also evident in the solid state. Saponification of the ester is not expected to significantly impact the Ru-N bond distances, or the N-Ru-N bite angles. No significant structure differences were observed for $[\text{Ru}(\text{dtb})_2(\text{dcbH}_2)](\text{ClO}_4)_2$ when compared to **1**. An average Ru-N bond length of 2.056 \AA and an average N-Ru-N bite angle of 78.62° was observed.

A pertinent value for this study is the “molecular diameter”, or the distance between the farthest points on the molecule. This value was taken to be the distance between substituents in the 4 positions of bipyridine that were trans to one another on adjacent coordinated ligands. More specifically, this is the H to H distance for **bpy**, the C to C of the methyl groups for **dmb**, or CH_3 group to CH_3 group of the *tert*-butyl groups for **dtb**. A summary these values and other relevant parameters for all three compounds are given in **Table 2.1**.

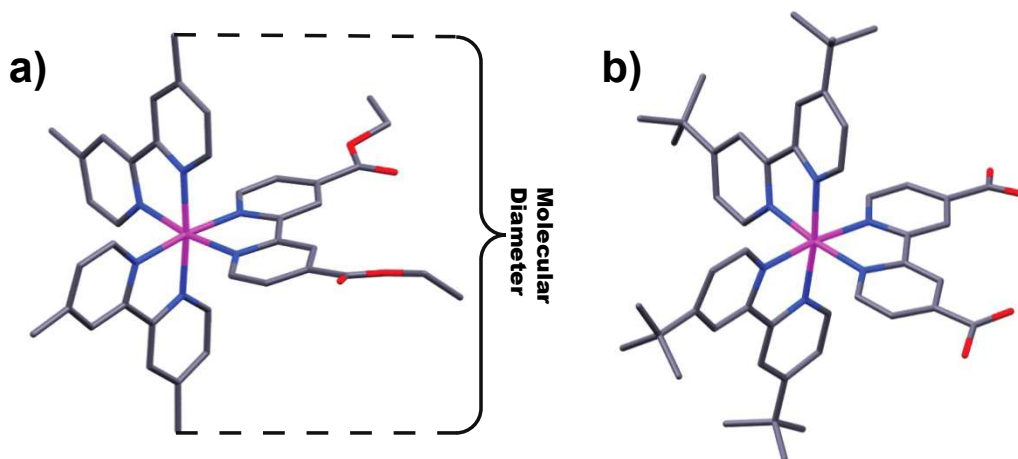


Figure 2.2: a) Crystal structure of $[\text{Ru}(\text{dmb})_2(\text{deeb})](\text{PF}_6)_2$. b) Crystal structure of $[\text{Ru}(\text{dtb})_2(\text{dcbH}_2)](\text{ClO}_4)_2$. All hydrogen atoms and anions are omitted for clarity purpose. Color code: Pink, Ru; blue, N; red, O; gray, C.

Table 2.1: Selected Crystal Structure Parameters for a Series of Ru Polypyridyl Compounds

	Average Ru-N Distance (Å)	Average N-Ru-N Bite Angle (°)	Molecular Diameter (nm)
bpy ^{a,b}	2.056	79.01	1.15
dmb ^b	2.054	78.83	1.27
dtb	2.056	78.62	1.37

^a Taken from ref¹⁵¹. ^b Values shown are for the ethyl ester complex.

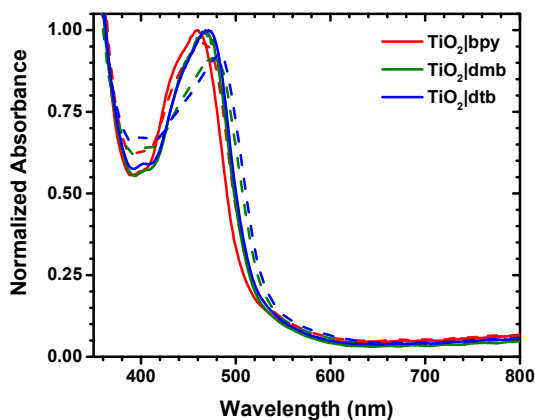


Figure 2.3: Normalized absorption spectra of compounds **bpy**, **dmb**, and **dtb** anchored to TiO₂ in neat CH₃CN (solid line) or in a 0.1 M LiClO₄ solution in CH₃CN (dashed line). The TiO₂ absorption spectrum was subtracted out from the spectra of the surface-functionalized films.

The TiO₂ thin films were reacted with the desired Ru compounds by submersion into concentrated CH₃CN solutions. Extended reaction times (>48 h) were used to ensure that maximum surface coverages were achieved. Representative spectra of the TiO₂ films placed in neat CH₃CN after surface-functionalization, abbreviated TiO₂|X, are seen in **Figure 2.3** (solid lines). The main absorption feature centered at ~450 nm observed in neat CH₃CN is reasonably assigned to metal-to-ligand charge transfer (MLCT) transitions. It is assumed that the peak extinction coefficients, ϵ , are retained upon surface anchoring, **Table 2.2**.

The addition of 0.1 M LiClO₄ to the neat CH₃CN induced a bathochromic shift of the MLCT absorption (**Figure 2.3**, dashed lines). This has previously been reported for ruthenium polypyridyl complexes, and is attributed to a change in the electric field at the surface of the TiO₂ upon cation adsorption.^{76,152,153} The peak absorption for each compound in the presence of Li⁺ is shown in **Table 2.2**. The surface coverage Γ , was calculated using a modified Beer's law expression, **Table 2.2**.⁸⁶ Note that Γ was calculated with the assumption that the ϵ value measured in fluid solution was the same as that for the surface anchored molecules. Though several assumptions are made during this calculation, a comparison of values between the three compounds provides insight into the molecular environment present at the surface. A decrease in Γ was seen with increasing steric bulk, suggesting that the side groups influence the intermolecular distance.

Spectroelectrochemical measurements were performed on TiO₂|**dmb** to quantify the $E^\circ(\text{Ru}^{\text{III/II}})$ potential. Application of a positive applied potential resulted in spectral changes consistent with oxidation of Ru^{II} to Ru^{III}, **Figure 2.4**. Complete oxidation to yield Ru^{III} was determined when an increased applied potential no longer induced a spectral change. The mole fraction, χ , of oxidized and reduced species present at a given applied potential was determined through spectral modeling using a linear combination of the Ru^{II} and Ru^{III} species.

Spectroelectrochemical measurements were performed on TiO₂|**dmb** to quantify the $E^\circ(\text{Ru}^{\text{III/II}})$ potential. Application of a positive applied potential resulted in spectral changes consistent with oxidation of Ru^{II} to Ru^{III}, **Figure 2.4**. Complete oxidation to yield Ru^{III} was determined when an increased applied potential no longer induced a spectral change. The mole fraction, χ , of oxidized and reduced species present at a given applied potential was determined through spectral modeling using a linear combination of the Ru^{II} and Ru^{III} species.

Table 2.2: Selected Spectral, Electrochemical, and Film Parameters for the Compounds Studied

	$\lambda_{\max}^{\text{soln}}$ (nm) (ϵ , $\text{M}^{-1}\text{cm}^{-1}$) ^a	$\lambda_{\max}^{\text{neat}}$ (nm) ^b	$\lambda_{\max}^{\text{Li}^+}$ (nm) ^c	E° (V vs NHE) (α)	Γ (10^{-7} mol/cm ²)	c_0 (10^{19} cm ⁻³)
bpy	471 (12000) ^d	460	467	1.48 (1.4) ^d	1.9 ± 0.14	38 ± 2
dmb	475 (14200)	468	475	1.39 (1.6)	0.95 ± 0.20	19 ± 1
dtb	465 (16400) ^e	471	482	1.36 (1.2) ^e	0.77 ± 0.13	12 ± 1

^a Peak absorption of the compound in neat CH₃CN. ^b Peak absorption of the TiO₂ anchored compound in neat CH₃CN. ^c Peak absorption of the TiO₂ anchored compound in 0.1 M LiClO₄ containing CH₃CN. ^d Taken from Ref ⁵⁶. ^e Taken from Ref 14

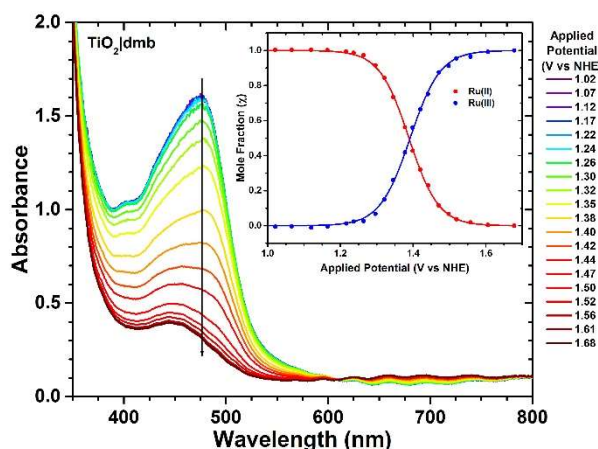


Figure 2.4: Spectroelectrochemical oxidation of TiO₂|**dmb** immersed in 0.1 M LiClO₄/CH₃CN electrolyte. The inset plots the fraction of oxidized or reduced compound as a function of applied potential. Overlaid is a fit to a modified Nernst equation, **Equation 2.5**.

Spectroelectrochemical measurements were performed on TiO₂|**dmb** to quantify the $E^\circ(\text{Ru}^{\text{III/II}})$ potential. Application of a positive applied potential resulted in spectral changes consistent with oxidation of Ru^{II} to Ru^{III}, **Figure 2.4**. Complete oxidation to yield Ru^{III} was determined when an increased applied potential no longer induced a spectral change. The mole fraction, χ , of oxidized and reduced species present at a given applied potential was determined through spectral modeling using a linear combination of the Ru^{II} and Ru^{III} species.

The formal reduction potential, E° , was determined using **Equation 2.5**. In this equation, E_{app} is an applied potential and α is an ideality factor that accounts for deviations from Nernstian behavior. Values for E° and α are given in **Table 2.2**.

$$\chi = \left(1 + 10^{(E_{\text{app}} - E^\circ)/(\alpha \cdot 59)}\right)^{-1} \quad (2.5)$$

Insight into intermolecular electron self-exchange was gained by spectroscopically monitoring the oxidation process as function of time after a potential step to potentials ~ 0.5 V positive of $E^\circ(\text{Ru}^{\text{III/II}})$. A comparison of this rate for the three Ru compound of interest is seen in **Figure 2.5**. The rate of this conversion, monitored at a single wavelength, is converted to apparent electron diffusion coefficient, D_{CA} , using **Equation 2.6**.⁸³

$$\Delta A = \frac{2\Delta A_f D_{\text{CA}}^{1/2} t^{1/2}}{d\pi^{1/2}} \quad (2.6)$$

In this equation, ΔA_f is the final change in absorbance, and d is TiO_2 film thickness. A linear fit to the initial CA data allowed for the determination of D_{CA} using **Equation 2.6**. The wavelengths monitored during the oxidation were 468, 480 and 482 nm for **bpy**, **dmb**, and **dtb**, respectively. During the analysis, care was taken to only fit the linear portion of the data. Deviations from linearity indicates movement away from diffusion-limited conditions, which is typical as the oxidation front approaches the edge of the film. Bonhôte and coworkers reported that linearity was maintained for the oxidation of $\sim 60\%$ of the molecules within the mesoporous thin film.⁸³ Thus, only the first 60% of the total observed absorption change was fit, gold overlay, **Figure 2.5**. The observed rate of oxidation, as well as the calculated D_{CA} value, was seen to increase following **dtb** < **bpy** < **dmb**.

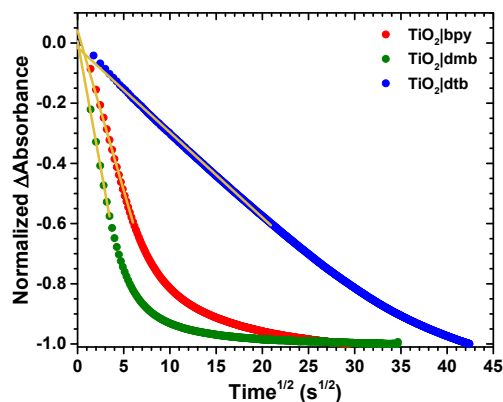


Figure 2.5: Normalized absorption change measured after application of a potential sufficient to oxidize the indicated compounds plotted against the square root of time. Overlaid in gold is the fit based on Equation 2.6.

Table 2.3: Apparent Diffusion Coefficients and Marcus Self-Exchange Parameters for Surface Anchored Ruthenium Compounds

	D_{CA} ($10^{-9} \text{ cm}^2/\text{s}$)	D_{CV}^a ($10^{-10} \text{ cm}^2/\text{s}$)	E_{act} (meV)	A ($10^{-6} \text{ cm}^2/\text{s}$)	H_{AB}^b (meV)	R (nm)
TiO ₂ bpy	2.2 ± 1.1	1.1 ± 0.1	240 ± 30	50	0.07 ± 0.04	1.4 ± 0.03
TiO ₂ dmb	5.3 ± 0.6	3.1 ± 0.2	240 ± 20	3	0.10 ± 0.06	1.8 ± 0.03
TiO ₂ dtb	0.24 ± 0.01	0.14 ± 0.01	270 ± 30	43	0.02 ± 0.02	2.0 ± 0.06

^a Value taken at 30 °C. ^b $\lambda = 900 \pm 100$ meV shared between data sets.

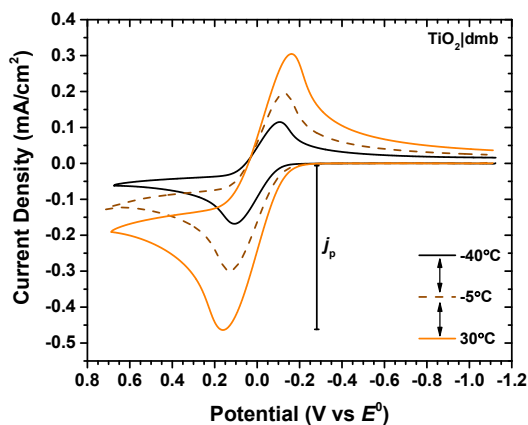


Figure 2.6: Representative cyclic voltammograms for **dmb** anchored to TiO₂ immersed in 0.1 M LiClO₄ in CH₃CN at the indicated temperatures.

The apparent diffusion coefficients were determined over a range of temperatures for each compound by cyclic voltammetry (CV). The peak current density, j_p , observed during the CV, was related to D_{CV} using **Equation 2.7**.⁹²

$$D_{CV} = \frac{5.02 k_b T_p^2}{q^3 c_0^2 \nu} \quad (2.7)$$

In this equation, k_b , q , T , c_0 , and ν are the Boltzmann constant (J/K), the elementary charge (C), temperature (K), the volume concentration (cm^{-3}), and scan rate (V/s), respectively. Determination of c_0 was non-trivial, as concentrations at nanocrystalline TiO_2 interfaces are an ill-defined parameter. For the purposes of this study, the total volume available to the molecule was assumed to be the volume of the TiO_2 film, excluding pores, with the Ru molecules uniformly dispersed throughout the remaining volume. The Γ value was initially quantified using a modified Beer's law. Γ was then converted to c_0 by **Equation 2.3**, where $\cos(45^\circ)$ accounts for the increase in path length due to the film being at a 45° angle to the probe. To account for a $\sim 50\%$ porosity, the calculated c_0 was multiplied by a factor of two. Table 2 shows the c_0 obtained for the compounds studied. Other methods used to calculate c_0 are discussed in the experimental section that provided quantitatively different values of D_{CV} , yet the same trend was observed. Throughout all experiments, ν was kept to be 0.1 V/s, applied against a self-contained Ag wire. The expected temperature dependence of the reference electrode was not important to the experiment. A linear correction was made to all the data in order to compensate for non-faradaic processes, as was described by previous by Moia et al.⁹² The j_p was determined by dividing the observed peak current from the initial scan by the geometric area of the TiO_2 film ($\sim 1.5 \text{ cm}^2$).

$$D_{CV} = A e^{\left(\frac{-E_{act}}{k_b T}\right)} \quad (2.8)$$

Activation energies, E_{act} , for self-exchange on the surface were extracted from the variable temperature data with the Arrhenius equation, **Equation 2.8**. **Figure 7A** shows the D_{CV} obtained over a range of temperatures fit to **Equation 2.8**. The E_{act} along with the associated pre-exponential factors, A , are included in **Table 2.3**. The abstracted E_{act} values were between 200-300 meV.

In order to perform a Marcus analysis on these data, D_{CV} was converted into an effective electron transfer rate constant, k_{SE} , using **Equation 2.9**.⁹² This required knowledge of the intermolecular distance, R , between redox active sites. It was assumed that the molecules were evenly distributed in a cubic lattice throughout the porosity corrected volume of the film, **Equation 2.4**. Values of R for each compound are shown in **Table 2.3**. These values represent an ‘intermediate’ estimate of the true and unknown intermolecular distance on the TiO_2 surface.

$$k_{\text{SE}} = \frac{4D_{\text{CV}}}{R^2} \quad (2.9)$$

The magnitude of H_{AB} was determined by fitting the data shown in **Figure 2.7B** to non-adiabatic Marcus theory for electron self-exchange, **Equation 2.10**, where \hbar and λ are the reduced Planck constant and the total reorganization energy, respectively. To aid in the fitting process, a global fitting analysis was used and λ was shared between the three data sets. **Table 2.3** shows the resulting H_{AB} values. As previously mentioned, the value of R utilized directly influenced the value of H_{AB} determined.

$$k_{\text{SE}} = \left(\frac{2\pi}{\hbar}\right) \left(\frac{|H_{\text{AB}}|^2}{\sqrt{4\pi\lambda k_{\text{b}}T}}\right) \exp\left(-\frac{\lambda}{4k_{\text{b}}T}\right) \quad (2.10)$$

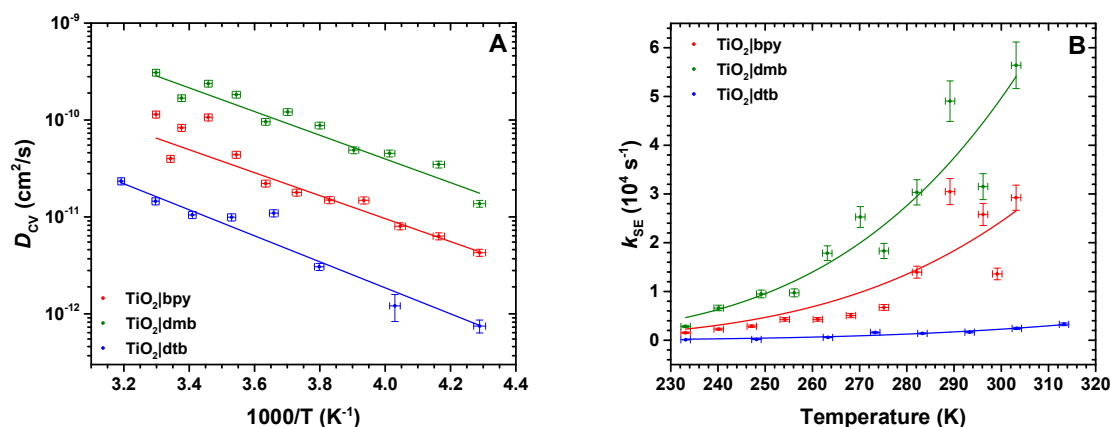


Figure 2.7: (A) Arrhenius plot for **bpy**, **dmb**, and **dtb** anchored to TiO_2 describing the variation of D_{cv} with inverse temperature as obtained by cyclic voltammetry. Overlaid are the best fits to the Arrhenius equation. (B) The temperature dependence of k_{SE} as described by non-adiabatic Marcus theory (overlaid curves).

2.4 Discussion.

As was described in the introduction section, self-exchange between surface immobilized molecules results in the transport of charge and is hence of interest for energy applications.⁹⁹ A key finding disseminated here is that insulating organic side-groups on the redox active molecules can be used to tune self-exchange ‘hole hopping’ and hence charge transport across nanocrystalline TiO_2 surfaces. This was most readily quantified by abstraction of an apparent diffusion constant, D , from the temporal data. Indeed, an experimental challenge was to identify methods by which the intrinsic self-exchange rate constants and activation parameters could be reliably abstracted from bulk kinetic electrochemical data. The two techniques utilized herein relied upon a ramped (cyclic voltammetry) or stepped (chronoabsorptometry) potential to quantify $\text{Ru}^{\text{III/II}}$ self-exchange and while both techniques revealed the same trend in D , **dmb** > **bpy** > **dtb**, the quantitative values differed significantly. Below we discuss the electrochemical methods used to quantify self-exchange followed by an

analysis of the kinetic data within the framework of Marcus theory for non-adiabatic electron transfer.

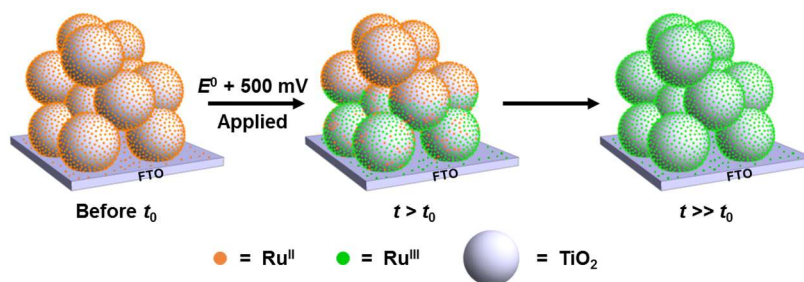
Quantification of Reduction Potentials and Apparent Diffusion Coefficients. The formal $E^\circ(\text{Ru}^{\text{III/II}})$ reduction potentials were taken as the equilibrium potential where equal numbers of compounds measured spectroscopically were present in the formal oxidation states of III and II. The electron donating methyl- and *tert*-butyl groups in the dmb and dtb ligands induced a measurable negative shift in the formal reduction potentials relative to that measured for $\text{TiO}_2|\text{bpy}$. A complication in data analysis was the non-Nernstian behavior of the interfacial redox chemistry. An ~ 80 mV potential step was required to induced a factor of ten change in the $\text{Ru}^{\text{III}}/\text{Ru}^{\text{II}}$ ratio for **bpy** and ~ 70 mV were required for **dtb** rather than the Nernstian value of 59 mV. The spectroelectrochemical data were adequately modeled by including α to account for deviation from Nernstian behavior, as has been done in the past, however such modeling does not address the origin(s) of the non-ideality. Prior studies with metalloporphyrins and molecules with two redox active groups have indicated that the non-ideality arises from local electric fields present at the oxide-electrolyte interface.¹⁵⁴ The α increased in the order **dtb** > **dmb** > **bpy** suggesting that intermolecular interactions like those in the Frumkin isotherm model may also underlie this behavior.⁹⁰ If instead, the non-ideality arises from a distribution of formal reduction potentials, then the data may reflect a greater degree of heterogeneity for **bpy** than for **dtb**. Regardless of the non-ideality origin(s), the steady state spectroelectrochemical data suggests that the true self-exchange electron transfer hole-hopping may not occur with $\Delta G^\circ = 0$ throughout the mesoporous film.

Chronoabsorptometry (CA) and cyclic voltammetry (CV) experiments were performed to estimate the diffusion coefficient D for self-exchange. The data analysis is based upon a semi-

infinite diffusion boundary approximation that has been previously described.⁹² Since the mesoporous TiO₂ thin film has a finite thickness, this analysis is only valid if the ‘front’ of oxidized molecules does not reach the outer edge of the mesoporous thin film. This boundary condition is maintained through the CV experiments, where only about 5% of the redox active molecules within the thin film were oxidized. This value was determined by using $L = (D_{CV} * t)^{1/2}$ where L is the linear diffusion length and t is the elapsed time from the onset of oxidation to the peak oxidation current. In contrast, all of the electrochemically accessible compounds were oxidized over the course of the CA experiments, **Scheme 2.3**.

Deviation from linear was observed when ~60% of the compounds were oxidized, which has been previously attributed to the breakdown of the boundary conditions.¹⁵⁵ Both experiments revealed that D decreased in the order **dmb** > **bpy** > **dtb**, however the values abstracted from cyclic voltammetry data were consistently about an order of magnitude larger, $D_{CV} > D_{CA}$. This behavior has previously been reported and is not fully understood.⁹⁶ Since a larger fraction of the self-exchange occurs near the fluorine-doped tin oxide (FTO) substrate in the voltammetry measurements, the larger diffusion coefficient may reflect more rapid self-exchange near the FTO interface.

Values of D have previously been determined for other metal polypyridyl complexes anchored to TiO₂ surfaces, and provide context for the values reported here. Trammel and Meyer previously determined $D_{CA} = 1.4 \times 10^{-9} \text{ cm}^2/\text{s}$ for the Os^{III/II} self-exchange in the compound [Os(bpy)₂(dcb)]²⁺.⁸⁶ This value is within experimental error the same as that measured for the analogous Ru compound, yet is in contrast to solution phase self-exchange



Scheme 2.3: An idealized representation of three surface functionalized anatase layers on an FTO substrate during a chronoabsorptometry (CA) experiment. At time t_0 all of the ruthenium compounds are in the formal oxidation state of II. After a potential step 500 mV more positive than the formal $E^\circ(\text{Ru}^{\text{III/II}})$ reduction potential, the FTO substrate oxidizes the Ru^{II} compounds present on the FTO surface followed by self-exchange ‘hopping’ across the nanocrystalline TiO_2 surface. A moving front of oxidized dyes nearly equidistant from the FTO substrate is observed at $t > t_0$. At longer times $t \gg t_0$ all the molecules within the mesoporous thin film are oxidized. The semi-infinite diffusion boundary approximation restricts data analysis to about 60% oxidation of the thin film. In cyclic voltammetry experiments that are now shown, only about 5% of the film is oxidized.

studies, where $[\text{Os}(\text{bpy})_3]^{3+/2+}$ self-exchange rate constants were more than double that of $[\text{Ru}(\text{bpy})_3]^{3+/2+}$.¹⁵⁶ Comparisons such as these draw attention to the differences that may exist between electron-transfer reactions between molecules in fluid solution, and those anchored at a semiconductor interface. In another literature report, D_{CA} was quantified for $[\text{Ru}(\text{bpy})_2(4,4'-(\text{PO}_3\text{H}_2)_2\text{-bpy})]^{3+/2+}$ in an 0.1 M HClO_4 aqueous medium.¹⁴³ Remarkably similar values for D were quantified for this compound ($1.33 \times 10^{-9} \text{ cm}^2/\text{s}$) as for those reported herein. Similar values were also reported by Mallouk *et. al.*¹⁵⁷ Hence the nature of the anchoring groups, carboxylic acids versus phosphonic acids, has a less significant impact than does the inclusion of insulating organic functional groups on the ancillary ligands. However, it should be emphasized that the details of the mesoporous TiO_2 film structure may have a significant yet undocumented influence on D . Factors such as film porosity, nanocrystallite size, and surface chemistry have an unknown impact on the electron transfer kinetics. Until such parameters are better understood, systematic studies similar to the one reported here are needed.

Self-exchange Kinetics and Theory. Estimation of rate constant for self-exchange, k_{SE} , from D_{CV} requires knowledge of the distance between the surface anchored molecules. While it is sometimes stated that dcb-containing molecules bind to the TiO_2 surface in monolayer surface coverage, the ill-defined surface area make such statements difficult to validate experimentally. There is little data to suggest that these dicationic complexes form multi-layers on TiO_2 , but whether any or all are within Van der Waals radii of each other is unclear. However, in the raw measured visible absorption spectra of the thin films it was clear that the saturation surface coverage increased in the order **dtb** < **dmb** < **bpy**. This correlates well with a steric increase in R when tertiary-butyl groups replace methyl groups or H atoms and suggests that on average the Ru centers are further apart in **dtb**.

The number of molecules present within the mesoporous film is reasonably estimated through absorption measurements using Beer's Law, though the distance between the molecules and their homogeneity is much more difficult to assess. An analysis described in the experimental section takes the total number of redox active molecules and disperses them within the mesoporous thin film as if there were no TiO_2 present, to give the largest value of R , as well as the case where the molecules pack as tightly as they do in the solid state crystal structure. These analyses provide upper and lower limits to R , that are within a factor of ten of what would be expected when molecules as 10 Å spheres are close-packed on a planar idealized surface. Furthermore, the mean separation distance in the encounter complex formed between $Ru(bpy)_3^{3+/2+}$ for solution-phase self-exchange reaction has been calculated to be 13.6 Å which is comparable to the intermolecular distances determined from the crystal structures of the compounds.¹⁵⁸ The k_{SE} values abstracted in such a manner were in good agreement with previous literature reports that are discussed in more detail below.

An Arrhenius analysis of k_{SE} revealed activation energies for each studied complex were within experimental error the same, $E_{act} = 250 \pm 50$ mV. Within the framework of Marcus theory for non-adiabatic electron transfer, the activation energy for electron transfer is approximately equal to the sum of the work required to bring the two species together and one fourth the total reorganization energy, $\lambda/4$. Assuming the work term is zero for the reaction between anchored molecules, this activation data implies a reorganization energy of ~ 1 eV, a value that is consistent with literature values for similar electron transfer reactions between Ru based chromophores anchored to TiO₂ nanocrystallites.⁹² As the inner-sphere contributions to the total reorganization energy are mainly associated with the Ru-N bond lengths and angles, there was no *a priori* reason to suspect that the methyl or *tert*-butyl substituents would contribute to λ and no evidence of significant bond length alterations were evident in the crystal structures. Moreover, the structural changes observed upon oxidation of similar Ru polypyridyl complexes are minimal and therefore λ_I contribute negligibly to the total reorganization.¹⁵⁹ As a result, the primary contribution to the total reorganization energy arises from outer sphere contributions that are difficult to determine experimentally. Based on the negligible contribution of λ_I to the total reorganization energy, we conclude that the changes in steric bulk have a minimal influence on λ_o .

Application of Marcus theory using a shared λ in the fitting procedure revealed that the electronic coupling matrix element, H_{AB} , increased from 0.02 to 0.10 meV in going from **dtb** to **dmb**. A λ of 900 ± 100 meV was found to provide the most satisfactory fit to all three data sets under the assumption that the reorganization energies do not change appreciably between the compounds investigated. In contrast to those observed here, values of H_{AB} observed for the electron self-exchange reaction for the parent complex Ru(bpy)₃^{3+/2+} in fluid solution are

reported to be between 2.5 meV and 12.4 meV.¹⁴⁵ The significant decrease in H_{AB} is likely a result of the increased molecular distance, and the heterogeneous nature of the interface.

Self-exchange and activation parameters garnered from studies of $\text{TiO}_2|\text{dtb}$ were dramatically different than those obtained with **dmb** or **bpy** providing compelling evidence that bulky side groups do indeed influence H_{AB} . This finding supports the previous suggestion that long-chain side groups can be used to tune self-exchange at these same interfaces. In side-by-side comparative studies both H_{AB} and D were consistently the largest for **dmb** which was intriguing as this is counter-intuitive to what was expected based on the steric bulk of the compounds. While it is not clear why this is the case, it suggests that the electron donating behavior of the alkyl substituents is also playing a role. The self-exchange rate constants for $\text{Ru}(\text{bpy})_3^{3+/2+}$ are orders of magnitude larger than those of the corresponding ammine or aqua compounds, behavior that Sutin rationalized by concluding that the π -acidic nature of the bipyridine provides sufficient electron density on the ligands for self-exchange. It is hence likely that substituents modify the ligand electron density in a manner sufficient to alter self-exchange between immobilized redox centers.

2.5 Conclusions.

Self-exchange intermolecular $\text{Ru}^{\text{III/II}}$ electron transfer across the surface of mesoporous nanocrystalline (anatase) TiO_2 thin film was characterized by cyclic voltammetry and chronoabsorptometry techniques for a series of three Ru polypyridyl compounds $[\text{Ru}(\text{LL})_2(\text{dcbH}_2)](\text{PF}_6)_2$, where LL is 2,2'-bipyridine (**bpy**), 4,4'-dimethyl-2,2'-bipyridine (**dmb**) or 4,4'-di-*tert*-butyl-2,2'-bipyridine (**dtb**) and dcb is 2,2'-bipyridyl-4,4'-dicarboxylic acid. Apparent diffusion coefficients, D , abstracted from the electrochemical data revealed that the self-exchange was much slower for the *tert*-butyl containing compounds. Temperature

dependent measurements revealed that this was due to lower intermolecular electronic coupling that result from the sterically bulky *tert*-butyl groups. The results indicate that insulating side groups can indeed be placed on redox active molecules to tune the electronic coupling, and hence self-exchange rate constants, without significantly altering the reorganization energy for electron transfer. Such behavior can be exploited in artificial photosynthetic assemblies both to enhance and inhibit lateral charge transport across oxide surfaces.

Chapter 3: Cation Dependent Charge Recombination to Organic Mediators in Dye-Sensitized Solar Cells

Reprinted with Permission from DiMarco, B. N.; O'Donnell, R. M.; Meyer, G. J. Cation-Dependent Charge Recombination to Organic Mediators in Dye-Sensitized Solar Cells. *J. Phys. Chem. C* **2015**, *119* (37), 21599–21604. Copyright 2016 American Chemical Society

3.1 Introduction

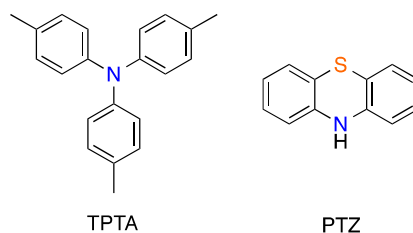
The sensitization of wide-bandgap semiconductors to visible light by organic and inorganic molecules, called sensitizers, has proven to be a viable means of solar energy conversion.^{38,160} Record sunlight-to-electrical energy conversion efficiency in a dye-sensitized solar cell (DSSC) now exceeds 12%^{34,35} and the potential for low cost production has motivated many studies toward practical application. The sensitized materials also provide new opportunities for advancing our fundamental understanding of light driven electron transfer reactions at molecular-semiconductor interfaces. This manuscript specifically focuses upon how the identities of cations present in the external acetonitrile electrolyte influence the unwanted recombination reaction between injected electrons and organic redox mediators.

The identity and concentration of alkali or alkaline earth cations present in the electrolyte is known to have a dramatic influence on the efficiency of an operational DSSC.^{161,162} Attempts to understand exactly why the cation identity is so critical to solar cell efficiency have been frustrated by the fact that the cations play many roles. For example, the cations are potent Lewis acids that form adducts with oxide surface sites that result in significant shifts in the energy levels of the TiO₂ acceptor states.^{76,106,108,163} For this reason they are sometimes called

“potential determining” cations that control excited state injection yields.^{106,108,164} In addition, smaller cations like Li^+ can intercalate into anatase TiO_2 and influence the transport of injected electrons to the external circuit; behavior that has been understood with an ambipolar diffusion model.^{165,166} In iodide containing electrolytes, the cation has been proposed to influence the rate at which the oxidized sensitizer is regenerated.¹⁶⁴ Finally, and of most relevance to this study, cations present in the electrolyte can screen the electric fields that are generated by excited-state injection.^{64,76,65,81,163} Given that the chemical nature and concentration of the cations influence so many elementary and inter-related processes in an operational DSSC it is perhaps not surprising that it remains a challenge to understand and fully optimize them for solar energy applications.

It was previously shown that charge recombination between $\text{TiO}_2(\text{e}^-)$ and I_3^- was cation dependent and the anionic nature of this acceptor was thought to be of critical importance.⁵⁹ To test the generality of this finding and to quantify recombination to organic redox mediators, two neutral electron donors were selected: tri-*p*-tolylamine (TPTA) and phenothiazine (PTZ), **Scheme 3.1**. In contrast to iodide, both of these mediators are positively charged upon oxidation and were hence expected to behave differently in the presence of the electric field created by the injected electrons. Indeed, charge recombination was sensitive to the identity of the cations present and this data provides new insights into interfacial electron transfer at sensitized TiO_2 interfaces.

Scheme 3.1: Organic redox mediators.



3.2 Experimental

Materials. The following solvents, reagents, and materials were purchased from the indicated providers, and used as received: acetonitrile (Burdick and Jackson, spectrophotometric grade), methanol (Fischer, ACS Reagent Grade), tri-*p*-tolylamine (TPTA, Sigma-Aldrich, 97%), phenothiazine (PTZ, Sigma-Aldrich, >97%) lithium perchlorate (LiClO_4 , Sigma-Aldrich, 99.99%); sodium perchlorate (NaClO_4 , Sigma-Aldrich 99%); magnesium perchlorate ($\text{Mg}(\text{ClO}_4)_2$, Sigma-Aldrich, ACS Reagent Grade), calcium perchlorate tetrahydrate ($\text{Ca}(\text{ClO}_4)_2 \cdot 4\text{H}_2\text{O}$, Sigma-Aldrich, 99%), argon gas (Airgas, >99.998%), microscope slides (Fisher Scientific, 1mm thick). The $[\text{Ru}(\text{dtb})_2(\text{dcb})](\text{PF}_6)_2$ was available from previous studies.⁶⁴

Materials Preparation. Anatase nanocrystallites of TiO_2 were prepared using previously reported methods.¹⁴¹ TiO_2 pastes were doctor bladed onto glass microscope slides, which had previously been cleaned with methanol. Scotch tape (~10 μm thick) was used to provide a consistent thickness and size to the films. After drying (~30 minutes, covered), the tape was removed and the glass slides were sintered in a 450°C furnace under a blanket of oxygen. Films were allowed to cool to near room temperature before removal, and were stored in an oven (~70°C) prior to use. Films were sensitized to saturation surface coverages ($>6 \times 10^8 \text{ mol/cm}^2$) by submersion in concentrated solutions (50:50 tert-butanol/acetonitrile) of

[Ru(dtb)₂(dcb)](PF₆)₂ for a minimum of 48 hour prior to use. Slides were rinsed with neat acetonitrile and placed in neat acetonitrile for >30 minutes to remove weakly bound sensitizers.

Spectroelectrochemistry. An EC Epsilon electrochemical analyzer was employed as a potentiostat for electrochemical measurements. Solution spectroelectrochemistry employed a Pine Research Institute honeycomb spectroelectrochemical cell, equipped with a gold working electrode. A non-aqueous reference electrode (0.1 M LiClO₄ acetonitrile, Pine Research Institute) was used throughout, and was externally calibrated against the Fc⁺⁰ redox couple in a 0.2 M LiClO₄ acetonitrile solution. This allowed for conversion to the KCl-saturated aqueous calomel electrode (SCE) using previous literature values (Fc^{0/+} = 0.31 V vs SCE), where SCE is 0.241 V positive of NHE.¹⁴⁹ Measurement UV-Vis measurements were taken on either an Agilent Cary 50 or 60 spectrophotometer at room temperature. Solutions of PTZ were sparged with argon for >30 minutes to prevent known sulfoxide chemistry.¹⁶⁷

Transient Absorption. Nanosecond transient absorption measurements were obtained with a previously described apparatus.¹⁶⁸ Briefly, sample excitation was provided by a Q-switched, pulsed Nd:YAG laser (Quantel USA (BigSky) Brilliant B; 5-6 ns full width at half maximum, 1 Hz, ~10mm diameter spot size), using a frequency doubler to generate 532 nm light. Excitation fluence was measured at the sample using a thermopile (Molelectron). Power was generally kept between 1-5 mJ/pulse, with a normal experimental values being at ~2.5 mJ/pulse. Sensitized TiO₂ thin films were placed in quartz cuvettes fitted with 24/40 ground glass joints. Acetonitrile solutions containing 0.1 M of a single metal perchlorate salt and between 25-50 mM of the mediator of choice were then added. Solutions were sparged with argon for >30 minutes and sealed with a rubber septum before use. To generate full-wavelength transient absorption spectra in the visible region, kinetic measurements were taken

in 5-30 nm increments over the desired wavelength range. Typically, about 30 kinetic traces were averaged at each observation wavelength. In an effort to improve the signal-to-noise ratio, data at a single time point were often generated by averaging 1-11 adjacent time points. Single wavelength kinetics were averaged using 90-150 individual kinetic traces in order to achieve satisfactory signal-to-noise.

Data Modeling. Kinetic modeling was performed with OriginPro 9 which utilizes a Levenberg Marquardt iteration method.

3.3 Results

Thin films of mesoporous TiO_2 were sensitized to visible light with $\text{Ru}(\text{dtb})_2(\text{dcb})^{2+}$ by immersion in a 1:1 (v/v) *t*-butanol/acetonitrile solutions for 48 hours at room temperature. Typical saturation surface coverages were $\sim 7 \times 10^{-8} \text{ mol/cm}^2$ as determined by previously reported methods.⁷⁶ Sensitized thin films, abbreviated $\text{TiO}_2|\text{Ru}$, exhibited a characteristic metal-to-ligand charge transfer (MLCT) band with a peak centered at 465 nm in neat acetonitrile. The presence of 0.1 M metal perchlorate salts resulted in a bathochromic shift of the absorption maximum relative the value measured in neat acetonitrile, with the dications displaying the most significant shift, **Figure 3.1**.

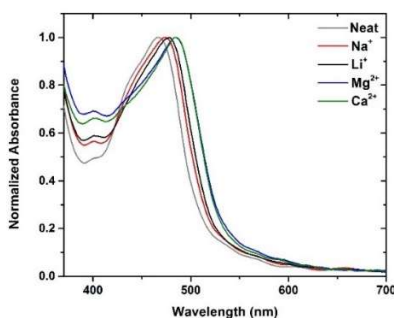


Figure 3.1: Steady-state UV-Vis absorbance of $\text{TiO}_2|\text{Ru}$ thin film submerged in 0.1 M acetonitrile solutions of the indicated metal perchlorate salt.

The neutral PTZ donor displayed no significant absorption over the wavelength range of interest (400 – 800 nm). The TPTA showed a new feature between 400 – 500 nm in the visible absorption at concentrations used during the regeneration studies that was cation dependent, and maybe indicative of some aggregation or interactions with the cations. However, these new features were small by comparison to the main absorbance centered at 316 nm (<1%), suggesting minimal influence from this effect. The extinction coefficients for the neutral species were generated by serial dilution of stock acetonitrile solutions of the compound also containing 0.1 M NaClO₄. Final concentrations were between 30 – 400 μM. The spectrum and extinction coefficients of the oxidized forms of TPTA and PTZ were quantified by spectro-electrochemistry. In a typical experiment an electrochemical bias ~300 mV positive of the formal potentials of the donor (TPTA $E^0 = 0.99 \text{ V}^{169}$ and PTZ $E^0 = 0.70 \text{ V}^{53}$ vs. NHE, respectively) was applied to a working electrode in an acetonitrile electrolyte. Spectra were measured during the oxidation reaction that was deemed complete when the spectra became time independent. The extinction coefficients of the oxidized donors were determined by comparison to the initial absorbance of the neutral compound, **Figure 3.2**. The measured spectra of the oxidized species were experimental independent of the identity of the metal perchlorate salt present in the acetonitrile electrolyte.

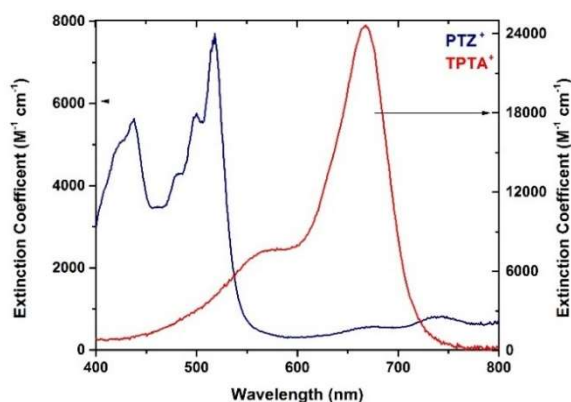


Figure 3.2: The visible absorption spectra of TPTA^+ and PTZ^+ in 0.1 M $\text{NaClO}_4/\text{CH}_3\text{CN}$ electrolyte.

Pulsed 532 nm excitation of a $\text{TiO}_2|\text{Ru}$ thin film immersed in an argon saturated 0.1 M metal perchlorate acetonitrile solution resulted in the formation of a charge-separated state comprised of an injected electron and an oxidized sensitizer, $\text{TiO}_2(\text{e}^-)|\text{Ru}^+$. The addition of 25 mM TPTA or 50 mM PTZ resulted in the appearance of intense transient absorbance bands in the visible region consistent with regeneration of the oxidized sensitizer, **Figure 3.3**. At the donor concentrations shown, the bleach associated with the oxidized sensitizer was completely absent on timescales $> 1 \mu\text{s}$ for both mediators, consistent with quantitative regeneration. Regeneration with PTZ was found to be rapid and complete by $\sim 400 \text{ ns}$. Also present in the absorption difference spectra at these timescales was a feature near 490 nm that has previously been assigned to a “Stark” shift in the ground state spectra due to the electric field generated by injected electrons.^{64,76} Indeed the measured difference spectra were well modeled by standard addition of the oxidized donor, the injected $\text{TiO}_2(\text{e}^-)$ electron, and the Stark shift. Overlaid as solid lines in **Figure 3.3** are such simulations of the experimental data. Full regeneration allows the recombination reaction $\text{TiO}_2(\text{e}^-)|\text{Ru} + \text{D}^+ \rightarrow \text{TiO}_2|\text{Ru} + \text{D}$ to be monitored without complications from other electron transfer reactions.

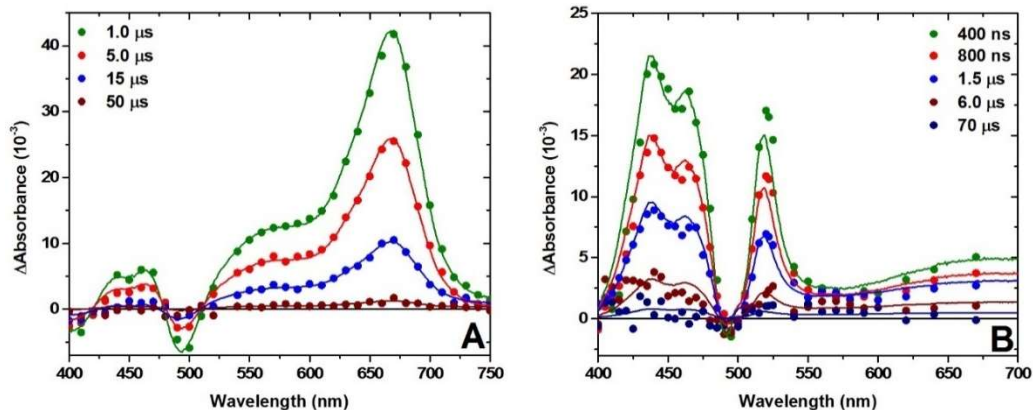


Figure 3.3: Absorption difference spectra measured at the indicated delay times after pulsed 532 nm laser excitation of a $\text{TiO}_2|\text{Ru}$ thin film in a 0.1 M $\text{NaClO}_4/\text{CH}_3\text{CN}$ electrolyte containing A) 25 mM TPTA and B) 50 mM PTZ. Overlaid on the data as solid lines are spectral simulations.

Shown in **Figure 3.4** are single wavelength absorption kinetics attributed to the recombination reaction between electrons in TiO_2 and the solution phase electron acceptor with the indicated cations present. The observation wavelength was 675 nm for TPTA^+ and 433 nm for PTZ^+ . The absorbance at 433 nm was an isosbestic point for absorbance shifts caused by the Stark effect under all conditions, and monitoring at this wavelength allowed the recombination kinetics to be more clearly monitored. The measured absorption change at these monitoring wavelengths was proportional to the concentration of oxidized donors. The kinetics were non-exponential, but were accurately modeled by the Kohlraush-Williams-Watts (KWW) stretched exponential function, **Equation 3.1**,

$$A(t) = A_0 e^{(-kt)^\beta} \quad (3.1)$$

where A_0 is the initial amplitude, k is the rate constant and β is inversely proportional to the width of an underlying Lévy distribution.⁶⁴ A value of $\beta = 0.65$ and 0.40 were found to provide the best fits of the kinetic data for TPTA and PTZ respectively. An “average” rate constant, calculated as the first moment in the distribution, could be obtained from **Equation 3**.

$$k_{KWW} = \frac{k\beta}{\Gamma(\frac{1}{\beta})} \quad (3.2)$$

The rate constants obtained from these fits are found in **Table 3.1**.

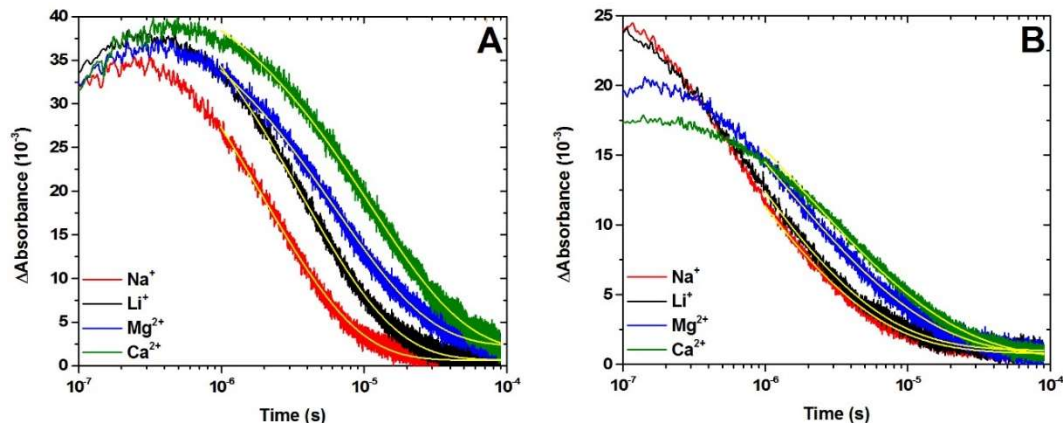


Figure 3.4: Single wavelength absorption changes measured after pulsed 532 nm laser excitation of a TiO_2/Ru thin film in CH_3CN solutions with 0.1 M of the indicated metal perchlorate and A) 25 mM TPTA and B) 50 mM PTZ. Kinetics were monitored at 675 nm and 433 nm for TPTA^+ and PTZ^+ respectively. Fits to the KWW model are overlaid on the data as solid yellow lines.

Table 3.1: Rate constants abstracted from KWW fits to the time resolved absorption data.

Cation	TPTA ($\beta=0.65$)		PTZ ($\beta=0.40$)		I_3^- ($\beta=0.45$) ^a	
	k (10^5 s^{-1})	k_{KWW} (10^5 s^{-1})	k (10^6 s^{-1})	k_{KWW} (10^5 s^{-1})	k (s^{-1})	k_{KWW} (s^{-1})
Na^+	4.4 ± 0.6	3.2 ± 0.4	2.1 ± 0.2	6.3 ± 0.6	450	180
Li^+	2.3 ± 1.1	1.7 ± 0.8	2.3 ± 0.2	6.9 ± 0.6	210	80
Mg^{2+}	1.5 ± 0.1	1.1 ± 0.07	0.90 ± 0.03	2.7 ± 0.1	160	60
Ca^{2+}	1.4 ± 0.4	1.0 ± 0.3	0.69 ± 0.2	2.1 ± 0.6	20	10

^aData taken from Ref ⁵⁹

3.4 Discussion

The reaction between electrons injected into sensitized TiO₂ and the oxidized donors TPTA⁺ and PTZ⁺, **Equation 3.3**, were quantified in acetonitrile electrolytes where the cation present was systematically varied. This reaction represents an unwanted yet thermodynamically favored process in DSSCs.



To our knowledge, this report represents the first spectroscopic study of charge recombination between electrons injected into TiO₂ and organic mediators where the electrolyte cations were intentionally varied. Previous studies have focused on the impact of metal cations (Na⁺, Li⁺, Mg²⁺) on rates of sensitizer regeneration or overall incident photon-to-current efficiencies.^{107,164} There was no experimental evidence suggesting that these cations interacted with the organic donors in their oxidized forms. However, a marked cation dependence was found for both donors where the rates decreased in the order Na⁺ > Li⁺ > Mg²⁺ > Ca²⁺. Interestingly, this is the same trend that has been reported for recombination with I₃⁻.⁵⁹ The origins of this cation dependence remain unknown. Possible physical phenomena that can account for this trend are discussed within the framework of published literature results below: Electric Fields, Diffusion Coefficients and Thermodynamic Driving Force.

Electric Fields. It is now well established that excited-state electron injection at a sensitized TiO₂ interface generates a significant electric field.^{64,65,81} Ions and solvent molecules in the electrolyte reorganize in response to this field. A recently discovered electro-absorption feature enables the magnitude of the field to be quantified.^{76,59,170} Injected electrons result in a uni-directional shift in the sensitizer absorption spectrum that is directly proportional to the

field strength. Interestingly, when the same number of electrons are injected into TiO_2 , the measured field strength as reported by the sensitizer absorption shift follows the same $\text{Na}^+ < \text{Li}^+ < \text{Mg}^{2+} < \text{Ca}^{2+}$ trend with magnitudes of 1.1 MV/cm for Na^+ and 2.2 MV/cm for the Ca^{2+} extremes.⁷⁶ This behavior has been attributed to the ability of the cations to screen the electric field from the surface anchored sensitizers. In previous work, the correlation of the field strength with the $\text{TiO}_2(\text{e}^-) + \text{I}_3^- \rightarrow$ charge recombination rate constants was attributed to the anionic nature of I_3^- as a repulsive interaction should result.⁵⁹ Cations that more rapidly and effectively screen the negative charge from TiO_2 enhanced the recombination reaction relative to those that screened more poorly.⁸¹

Recombination of injected electrons with I_3^- occurred on a milliseconds time scale while that for TPTA^+ and PTZ^+ was complete within tens of microseconds. The longer time window available for I_3^- may enable more efficient screening compared to the organic acceptors. Nevertheless, the fact that the same Lewis cation induced trend was observed for the organic acceptors employed herein disputes the conclusion that the surface electric field is the primary factor that gives rise to this trend. If the interfacial electric fields were the *sole* factor that determined recombination, then the opposite trend would have been expected for the cationic TPTA^+ or PTZ^+ relative to anionic I_3^- , behavior that is contrary to the experimental observations.

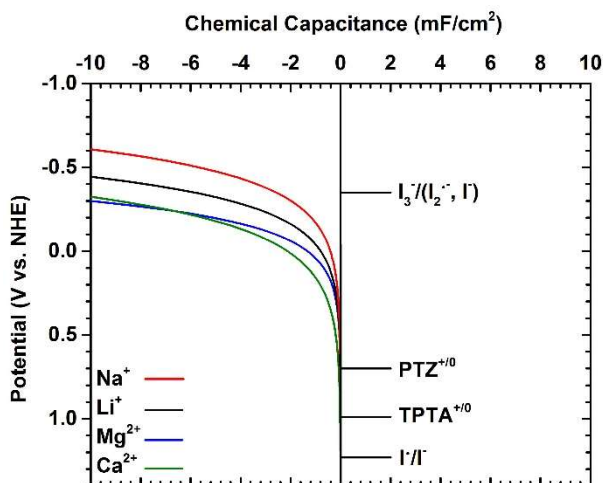
Diffusion Lengths. Wang and Peter found that the electron diffusion lengths followed the trend $\text{Na}^+ < \text{Li}^+ < \text{Mg}^{2+}$ in acetonitrile:valeronitrile electrolyte mixtures with iodide.¹⁰⁷ The electron diffusion lengths for these cations were $\sim 100\ \mu\text{m}$ for Na^+ and $\sim 40\ \mu\text{m}$ for the Mg^{2+} . The strong cation dependence indicates that transport of the injected electron and the cation were correlated, behavior that is consistent with previous intensity modulated photocurrent

measurements (IMPS) that have been understood in the context of ambipolar diffusion models.^{38,165} These diffusion lengths are much larger than the film thickness indicating that all of the injected electrons could be collected at the conductive glass substrate in these iodide nitrile solutions.¹⁰⁷ In the present work, all experiments were performed at the open circuit condition where care was taken to ensure that all injected electrons recombined before the next laser pulse. Under such conditions, a large diffusion length would enable more interactions as the TiO₂-electrolyte interfaces that would favor recombination as was measured experimentally.

Thermodynamic Driving Force. As mentioned in the Introduction section, the ‘potential determining’ cations studied here are known to influence the energy levels of the acceptor states in TiO₂ and hence may influence the free energy change accompanied with charge recombination. Fitzmaurice and coworkers first characterized this behavior with a Schottky-junction model and concluded that in acetonitrile the conduction band edge was at the most negative value (i.e. closest to the vacuum level) for Na⁺, followed by Li⁺ and then Mg²⁺; the entire potential range spanned about 100 mV.¹⁰⁶ The results of previous spectro-electrochemical studies with the indicated cations are shown in **Scheme 3.2**.⁷⁶ The data was acquired under the so-called forward bias condition for an n-type semiconductor where the absorption spectra of reduced TiO₂ was quantified. The measured spectra were superposable when normalized and hence gave evidence for only one redox active state in TiO₂ that many would term “trap states”.¹⁷¹ The onset potentials were nearly cation independent, while the capacitance associated with these states at more negative applied potentials that may correspond to the conduction band edge was clearly cation dependent. The relatively small number of electrons injected into the TiO₂ corresponds to a capacitance of < 1 mF/cm².

Therefore, if recombination were to occur directly from these trap states, then an approximately equivalent cation-independent, driving force for charge recombination would be expected.

Scheme 3.2: Comparison of the redox potentials of the mediators employed, and the energetics of the distribution of trap states in TiO₂ when different cations are employed. Reduction potentials for I₃⁻/(I₂^{•-}, I[•]) and I[•]/I⁻ are taken from reference ³⁹. The latter potential is relevant to sensitizer regeneration.



Alternatively, if recombination proceeds through thermal activation to a higher lying conduction band states prior to interfacial electron transfer, then a driving force and hence cation dependence kinetics would be anticipated. This latter interpretation is consistent with the experimental data. The cation dependence of the rate constant would then indicate Marcus normal kinetic behavior. Observations made here are in agreement with the latter, assuming electron transfer occurs within the Marcus normal region. Comparison of the rates of recombination across the different acceptors (I₃⁻, TPTA⁺, PTZ⁺) is not trivial as factors such as reorganization energy and electronic coupling are likely different between the mediators.

3.5 Conclusion

Charge recombination between electrons injected into mesoporous TiO₂ thin films and the oxidized organic mediators PTZ or TPTA present within the mesopores displayed a significant dependence on the electrolyte cation. Rate constants abstracted from time resolved absorption data decreased in the order $\text{Na}^+ \geq \text{Li}^+ > \text{Mg}^{2+} > \text{Ca}^{2+}$. Such data was inconsistent with a model where the surface electric field controls the recombination rate. Instead, the data is better understood by free energy considerations and electron transfer in the normal Marcus region, or larger diffusion lengths that enable more interactions of the injected electron and the redox mediators.

Chapter 4: Electron Transfer at TiO₂ Interface. A Comparative Study Between Free and Anchored Tri-Phenylamine (TPA) Redox Mediators

Work in collaboration with Ludovic Troian-Gautier and Seth L. Marquard

4.1 Introduction

The ability to control electron transfer reactions occurring between semiconductors materials and molecules is of broad interest.^{36,38,172} In dye-sensitized solar cells (DSSCs), prevention of electron transfer from the semiconductor to either oxidized sensitizers and/or oxidized redox mediators present in the electrolyte enhances charge collection, and therefore higher solar to energy conversion performance. Numerous studies have investigated these charge recombination processes that occurred to either surface anchored molecular chromophores^{56,36,114,122,124}, or to solution phase redox mediators^{40,57,59,135,152} separately. To our knowledge, there are currently no studies focused on understanding the influence that surface anchoring of the molecular acceptor has on the recombination process. This chapter presents the results of such a study, which compares interfacial electron transfer to a pair of tri-phenylamines (TPA) electron acceptors that are either free (***f*-TPA**) in fluid solution or anchored (***a*-TPA**) at the TiO₂ interface (**Figure 1**). A novel ruthenium chromophore was employed to sensitize the TiO₂ thin films, in order to generate an initial charge separated state. The insights gained have broad implications for both DSSC and dye-sensitized photoelectrosynthetic applications.

4.2 Methods and Materials

Materials: NMR solvents were purchased from Cambridge Isotope Laboratories, Inc. and were used as received. Sephadex-LH20 used for column purification was purchased from GE Healthcare and was swelled in the eluent of choice overnight prior to use. All other reagents and solvents were obtained from commercial sources and used without further purification. Mesoporous thin films of anatase TiO₂ nanocrystallites were prepared according to previously reported literature¹⁶⁸, and either used immediately after preparation or were stored in an ~70°C oven until use.

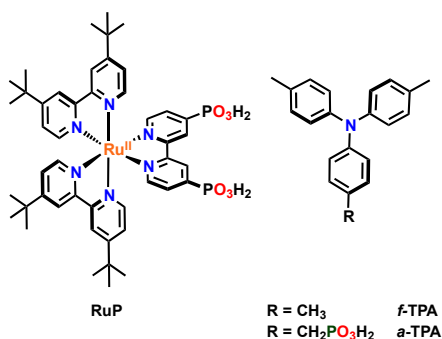


Figure 4.2: Structure of the ruthenium dye **RuP**, **f-TPA** and **a-TPA** used in this study

Molecular Characterization: Characteristic NMR spectra were obtained at room temperature on a Bruker Avance III 400 or 600 MHz spectrometer. Solvent residual peaks were used as internal standards for ¹H and ¹³C chemical shift referencing. All ³¹P{¹H} NMR spectra were obtained on a Bruker Avance spectrometer at 162 MHz and recorded relative to H₃PO₄. Generated spectra were processed using the MNOVA software.

Mass spectrometry was performed with a hybrid LTQ FT (ICR 7T) (ThermoFisher) mass spectrometer. Samples were introduced via a micro-electrospray source at a flow rate of 3 μL/min. The software Xcalibur (ThermoFisher) was used to analyze the data. Each mass

spectrum was averaged over 200 time domains. Electrospray source conditions were set as: spray voltage 4.7 kV, sheath gas (nitrogen) 3 arb, auxiliary gas (nitrogen) 0 arb, sweep gas (nitrogen) 0 arb, capillary temperature 275 °C, capillary voltage 35 V and tube lens voltage 110 V. The mass range was set to 150-2000 m/z. All measurements were recorded at a resolution setting of 100,000. Solutions were analyzed at 0.1 mg/mL or less based on responsiveness to the ESI mechanism. Low-resolution mass spectrometry (linear ion trap) provided independent verification of molecular weight distributions.

Spectroscopy: UV–vis absorption spectra were recorded on a Varian Cary 60 UV–vis spectrophotometer. The extinction coefficients were determined the dilution of stock solutions and represent averages of at least two independent measurements. Nanosecond transient absorption measurements were acquired on a setup published previously. Emission spectra was generated on an Edinberg Fluorescence Spectrometer. All solutions were sparged with argon for at least 30 minutes before transient absorption experiments.

Electrochemical measurements were performed on a BASi Epsilon potentiostat in a standard three-electrode cell in CH₃CN electrolytes employing a platinum disk working electrode and a platinum mesh as an auxiliary electrode. A non-aqueous silver/silver chloride pseudo-reference electrode (Pine) was calibrated using ferrocene.

Compound Synthesis:

[Ru(4,4'-bis-(diethylphosphonate)-2,2'-bipyridine)(η^6 -C₆H₆)Cl]Cl: A 100 mL round bottom flask equipped with a stir bar was charged with [Ru(η^6 -C₆H₆)Cl]₂Cl₂ (148 mg, 0.295 mmol), and 4,4'-bis-(diethylphosphonate)-2,2'-bipyridine (255 mg, 0.595 mmol). The flask was flushed with nitrogen and then dichloromethane (30 mL) was introduced via syringe. The resulting suspension was stirred for 12 h at room temperature. The solvent was removed by

rotary evaporation, and then 50 mL of diethyl ether was added to the yellow-brown residue. The solid precipitate was collected by suction filtration and then dried in vacuo affording 310 mg (78%) of the product as a yellowish brown solid. ^1H NMR (400 MHz, CDCl_3): δ 10.22 (brs, 2H), 8.47 (d, $J = 12.0$ Hz, 2H), 8.05 (dd, $J = 12.0, 4.0$ Hz, 2H), 6.44 (s, 6H), 4.24 (m, 8H), 1.37 (q, $J = 8.0$ Hz, 12H). ^{31}P NMR (162 MHz, CDCl_3): δ 10.69. HRMS (ESI) m/z : $[\text{M}]^+$ for $\text{C}_{24}\text{H}_{32}\text{N}_2\text{O}_6\text{P}_2\text{ClRu}$: 643.04676; Found: 643.04541.

[Ru(4,4'-bis-(diethylphosphonate)-2,2'-bipyridine)(4,4'-di-*tert*-butyl-2,2'-bipyridine) $_2$ Cl $_2$]: A 100 mL Teflon microwave vessel equipped with a stir bar was charged with [Ru(4,4'-bis-(diethylphosphonate)-2,2'-bipyridine)(η^6 - C_6H_6)Cl]Cl (164 mg, 0.241 mmol), and 4,4'-di-*tert*-butyl-2,2'-bipyridine (132 mg, 0.493 mmol). A 30 mL portion of 2:1 ethanol:water was added to the microwave vessel and the suspension was then sonicated for 10 minutes. The resulting suspension was stirred and heated to 160 $^\circ\text{C}$ in a microwave reactor over a 5-minute period, and then held at that temperature for 20 minutes. After the reaction cooled to room temperature, the orange solution was filtered through a 0.2 μm syringe filter, and then added to a 100 mL round bottom flask. The solvent was removed by rotary evaporation, and then the residue was dissolved in a minimum amount of methanol. The orange solution was loaded onto a column of Sephadex LH-20 and eluted with methanol. The fractions containing the product were combined and the solvent removed by rotary evaporation. The resulting compound was treated with diethyl ether and the solid was collected by suction filtration and then dried in vacuo affording 219 mg (80%) of the product as an orange-red solid. ^1H NMR (400 MHz, CD_3OD): δ 8.84 (d, $J = 16.0$ Hz, 2H), 8.71 (brs, 4H), 7.80 (m, 2H), 7.67 (m, 6H), 7.53 (m, 4H), 3.96 (m, 4H, under integrates due to partial hydrolysis under microwave conditions), 1.45 (s, 18H), 1.44 (s, 18H), 1.24 (t, $J = 16.0$ Hz, 6H, under integrates due to

partial hydrolysis under microwave conditions). ^{31}P NMR (162 MHz, CD_3OD): δ 7.09. Several hydrolyzed products were observed by HRMS; HRMS (ESI) m/z : $[\text{M}]^+$ for $\text{C}_{52}\text{H}_{69}\text{N}_6\text{O}_6\text{P}_2\text{Ru}$: 1037.37973; Found: 1037.38141; HRMS (ESI) m/z : $[\text{2M}]^{2+}$ for $\text{C}_{50}\text{H}_{65}\text{N}_6\text{O}_6\text{P}_2\text{Ru}$: 1009.34843; Found: 1009.35007

[Ru(4,4'-bis-(PO_3H_2)-2,2'-bipyridine)(4,4'-di-*tert*-butyl-2,2'-bipyridine) $_2$](PF_6) $_2$: A 50 mL round bottom flask was charged with Ru(4,4'- (ethyl hydrogen phosphonate)-2,2'-bipyridine)(4,4'-di-*tert*-butyl-2,2'-bipyridine) $_2$ Cl $_2$ (237 mg, 0.208 mmol). The flask was sealed with a rubber septum, and flushed with nitrogen before the introduction of 20 mL of anhydrous CH_3CN . Finally, trimethylsilyl bromide (100 μL , 0.758 mmol) was added by syringe. The reaction was heated to 70 $^\circ\text{C}$ for 2 days. After cooling to room temperature, 1 mL of methanol was added to the orange solution. The solvent was removed in vacuo affording an orange-red residue. The residue was dissolved in a minimal amount of water, and the product was precipitated by the addition of saturated aqueous NH_4PF_6 . The precipitate was collected and washed with a small amount of cold water, and then dried in vacuo affording 178 mg (69%). ^1H NMR (400 MHz, CD_3OD): δ 8.87 (d, J = 9.6 Hz, 2H), 8.71 (brs, 4H), 7.76 (brs, 2H), 7.68 (m, 6H), 7.53 (m, 4H), 1.45 (s, 18H), 1.44 (s, 18H). ^{31}P NMR (162 MHz, CD_3OD): δ 5.01. HRMS (ESI) m/z : $[\text{M}]^+$ for $\text{C}_{46}\text{H}_{57}\text{N}_6\text{O}_6\text{P}_2\text{Ru}$: 953.28583; Found: 953. 28687.

4-[N,N-di(*p*-tolyl)amino]benzylalcohol: The synthetic procedure was adapted from a previously published protocol.¹⁷³ 4-(N,N-di-*p*-tolylamino)benzaldehyde (1.38g, 4.58 mmol) was dissolved in 30 mL of ethanol. Sodium borohydride (675mg, 17.84 mmol) was then added and the reaction mixture was heated at reflux for 4 hours. Over time, the color changed from yellow to colorless. After reaction, the mixture was brought to room temperature and poured into 50 mL of water. The mixture was extracted three times with diethyl ether. The organic

layers were combined, dried over anhydrous MgSO_4 and filtered. The filtrate was finally evaporated under reduced pressure to yield the title compound as a white powder (1.36 g, 98 %). ^1H NMR (CDCl_3 , 600 MHz): 7.20 (2H, d, $J = 8.5$ Hz), 7.06 (4H, d, $J = 8.2$ Hz), 7.02 (2H, d, $J = 8.4$ Hz), 6.98 (4H, d, $J = 8.4$ Hz), 4.61 (2H, s), 2.31 (6H, s), 1.59 (1H, s). ^{13}C NMR (CDCl_3 , 600 MHz): 148.04, 145.41, 134.04, 132.60, 129.99, 129.14, 128.33, 124.63, 124.56, 122.88, 65.33, 20.95. HRMS (ESI-MS) m/z : $[\text{M}-\text{OH}]^+$ Calcd for $\text{C}_{21}\text{H}_{20}\text{N}$ 286.15957; Found 286.15888; $[\text{M}+\text{H}]^+$ Calcd for $\text{C}_{21}\text{H}_{21}\text{NO}$ 304.17014; Found 304.16851.

4-[N,N-di(*p*-tolyl)amino]benzylphosphonic ester: 4-(N,N-di(*p*-tolyl)amino)- benzylalcohol (1.04 g, 3.4 mmol) was dissolved in 13 mL of triethyl phosphite. The mixture was cooled to 0°C and sparged with argon for 30 minutes. A 900 mg (3.5 mmol) portion of I_2 was then added, and the mixture is stirred at 0°C for 5 minutes before being brought to room temperature and stirred for an additional 12 hours. After this time had elapsed, the triethyl phosphite was removed under vacuum and the residue was purified through column chromatography (SiO_2 , CH_2Cl_2 :MeOH 100:0 to 96:4). The final product was recovered as a yellow oil (1.16 g, 80%) ^1H NMR (CDCl_3 , 600 MHz): 7.13 (2H, dd, $J = 8.6, 2.5$ Hz), 7.04 (4H, d, $J = 8.2$ Hz), 6.97 (6H, m), 4.04 (4H, m), 3.09 (2H, d, $J = 21.3$ Hz), 2.30 (6H, s), 1.26 (6H, t, $J = 7.2$ Hz). ^{13}C NMR (CDCl_3 , 600 MHz): 147.14, 147.12, 145.38, 132.42, 130.53, 130.48, 129.91, 124.49, 124.41, 122.97, 122.95, 62.21, 62.16, 33.52, 32.61, 20.90, 16.53, 16.49. HRMS (ESI-MS) m/z : $[\text{M}]^{2+}$ Calcd for $\text{C}_{25}\text{H}_{30}\text{NO}_3\text{P}$ 424.20417; Found 424.20403.

-[N,N-di(*p*-tolyl)amino]benzylphosphonic acid: 4-[N,N-di(*p*-tolyl)amino]benzylphosphonic ester (423 mg, 1 mmol) was dissolved in 3 mL of dry CH_3CN . The mixture was cooled to 0°C and TMSBr (460 mg, 396 μL , 3 mmol) was added. The mixture was then stirred overnight at room temperature. After this reaction completed, the solvent was removed by

vacuum distillation and 5 mL of methanol was added to the resulting solid. Aqueous sodium hydroxide was added until the solution reached pH~8, which was followed by the formation of a white precipitate that was collected by filtration. The solid was then dissolved in 10 mL of water and precipitated by the addition of 0.1 M HCl. The off-white solid was filtered, washed with water and dried under vacuum (340 mg, 93 %). ^1H NMR (CD_3OD , 600 MHz): 7.16 (2H, d, $J = 7.6$ Hz), 7.04 (4H, d, $J = 8.2$ Hz), 6.88 (4H, m), 3.01 (2H, d, $J = 21.1$ Hz), 2.28 (6H, s). ^{13}C NMR (CD_3OD , 600 MHz): 148.03, 146.92, 133.36, 131.63, 131.59, 130.77, 125.25, 124.20, 35.82, 20.82. HRMS (ESI-MS) m/z : $[\text{M}+\text{H}]^+$ Calcd for $\text{C}_{21}\text{H}_{22}\text{NO}_3\text{P}$ 368.14157; Found 368.14135. $[\text{M}]^+$ Calcd for $\text{C}_{21}\text{H}_{22}\text{NO}_3\text{P}$ 367.13374; Found 368.14135.

4.3 Results and Discussion

The compounds **RuP** and ***a*-TPA** were prepared using standard synthetic methods. **RuP** displayed a characteristic metal-to-ligand charge transfer feature centered at 480 nm, while ***a*-TPA** and ***f*-TPA** displayed appreciable absorption features centered at 300 nm. Cyclic voltammetry measurements showed that the different compounds could be reversibly oxidized when dissolved in 0.1 M LiClO_4 CH_3CN solution, **Figure 4.2**. The formal reduction potentials were taken as the average potential between the peak anodic and cathodic currents. Spectroelectrochemical measurements were used to generate spectra of the one electron oxidized form of the TPAs and **RuP** chromophore. The oxidized TPA compounds displayed a strong absorption band centered around 670 nm (**Figure 4.3**), while oxidized **RuP** does not absorb appreciably within the visible region. A summary of these spectral and electrochemical properties can be found in **Table 4.1**. All the compounds displayed room temperature photoluminescence. The photoluminescence wavelength peaks and the photoluminescence lifetimes are also included in **Table 4.1**.

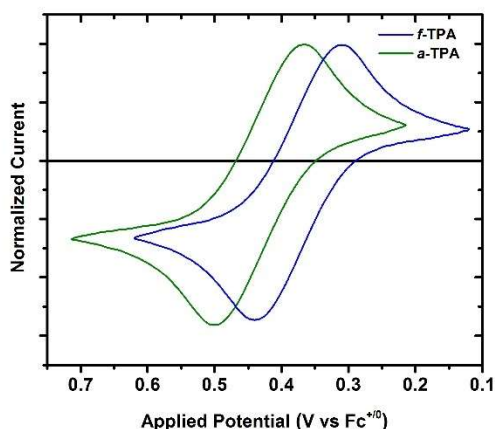


Figure 4.2: Cyclic voltammograms of the indicated TPA compounds performed in 0.1 M LiClO₄ acetonitrile.

Table 4.1: Electrochemical and photophysical properties of **RuP**, *a*-TPA and *f*-TPA.

	$E^{n+1/n}$ (V vs NHE) ^a	λ_{abs} (nm) (ϵ [M ⁻¹ cm ⁻¹])	λ^+ (nm) (ϵ [M ⁻¹ cm ⁻¹])	λ_{em} (nm)	τ (μ s)
RuP	1.37	460 (1.4)	---	638	1.3
<i>a</i> -TPA	1.05	300 (2.5) ^{a,b}	670 (2.4) ^b	--	< 10 ns ^c
<i>f</i> -TPA	0.99	301 (2.4) ^d	668 (2.4) ^d	353 ^e	< 10 ns ^c

^aElectrochemical data are recorded in 0.1M LiClO₄ CH₃CN solution whereas photophysical data are recorded in argon saturated CH₃CN. ^b Values obtained from the ester derivative *a*-TPA. ^c The emission lifetime for the TPA species could not be determined using our equipment. ^d Taken from ref ¹⁵². ^e Take from ref ¹⁷⁴

Mesoporous nanocrystalline TiO₂ films were prepared using previously reported methods¹⁴¹, and were sensitized to visible light by submersion into acetonitrile solutions containing **RuP** for a minimum of 12 h. The surface coverage was intentionally varied between saturation (9×10^8 M cm⁻²) and ~30 % of saturation (3×10^8 M cm⁻²) by altering the **RuP** solution concentration. When studying *a*-TPA, films prepared at ~30% saturation **RuP** coverage were subsequently submerged in concentrated *a*-TPA ethanol solutions, and the remaining surface sites were assumed to be filled with *a*-TPA. These “cofunctionalized” films are abbreviated as TiO₂|**RuP**|*a*-TPA.

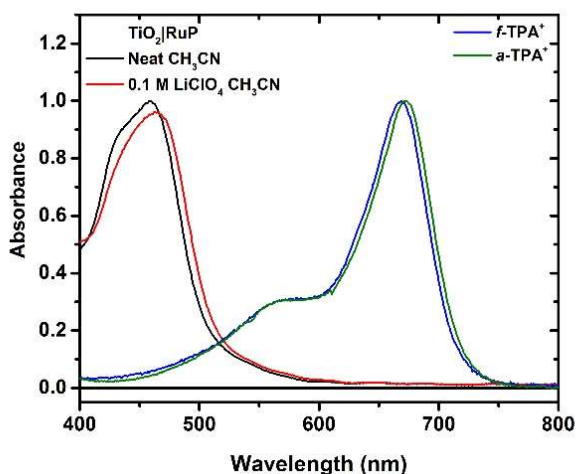


Figure 4.3: Visible absorption spectra of **RuP** sensitized TiO_2 in neat ACN (black) and 0.1 M LiClO_4 CH_3CN solution (red) as well as singly oxidized $f\text{-TPA}^+$ (blue) and $a\text{-TPA}^+$ (green).

Shown in **Figure 4.3** are the spectra generated from a saturated TiO_2 film placed in a neat acetonitrile solution, which displays the characteristic metal-to-ligand charge transfer feature of the **RuP** sensitizer. No significant spectral changes were observed at lower concentrations, or after cofunctionalization with $a\text{-TPA}$. The addition of 0.1 M LiClO_4 , which was introduced to the acetonitrile in order to improve the injection yield of the sensitizer^{76,108}, resulted in a bathochromic shift of the MLCT band. This has been previously attributed to a change in the electric fields present at the interface after Li^+ adsorption.^{76,152,153}

Figure 4.4 shows the transient absorption difference spectra generated from either $\text{TiO}_2|\text{RuP}$ submerged in a 30 mM $f\text{-TPA}$ CH_3CN solution or $\text{TiO}_2|\text{RuP}|a\text{-TPA}$. At early timescales (50 ns), the $f\text{-TPA}$ sample displayed spectral signatures assigned to $f\text{-TPA}^+$ and RuP^+ . This is consistent with partial sensitizer regeneration on a sub 50 nanosecond timescale. The RuP^+ continues to decay concomitant with the growth of $f\text{-TPA}^+$, achieving full sensitizer regeneration at $\sim 1\mu\text{s}$. An additional spectral signature at $\sim 500\text{ nm}$ results from an interaction between the ground state RuP^+ and $\text{TiO}_2(e^-)$ s whose electric field induces a hypochromic shift

in the sensitizer's absorbance, known as a “Stark effect”.^{64,76} In contrast, the ***a*-TPA** sample showed no evidence for the presence of the oxidized RuP sensitizer, indicating that sensitizer regeneration is very fast (< 20 ns). This is likely due to the proximity of ***a*-TPA** to the oxidized sensitizer that eliminates any diffusional component to the regeneration process. The same first derivative signature is seen at ~ 500 nm, further suggesting that ***a*-TPA** does not appreciably influence **RuP**'s spectral properties.

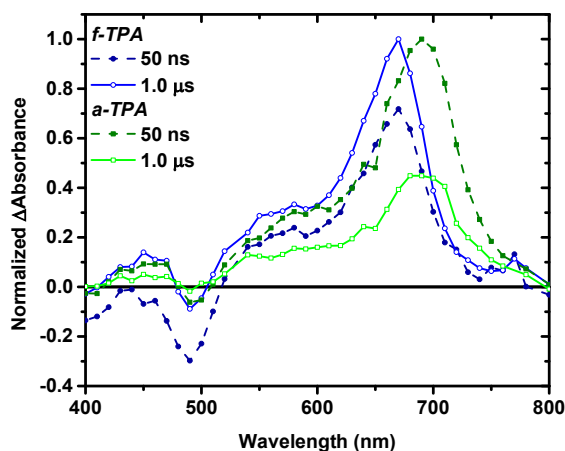


Figure 4.4: Absorption changes observed after pulse 532 nm light irradiation of TiO_2/RuP in the presence of 30 mM ***f*-TPA** (Blue scale) or cofunctionalized with ***a*-TPA** (red scale) submerged in argon saturated 0.1 M LiClO_4 CH_3CN .

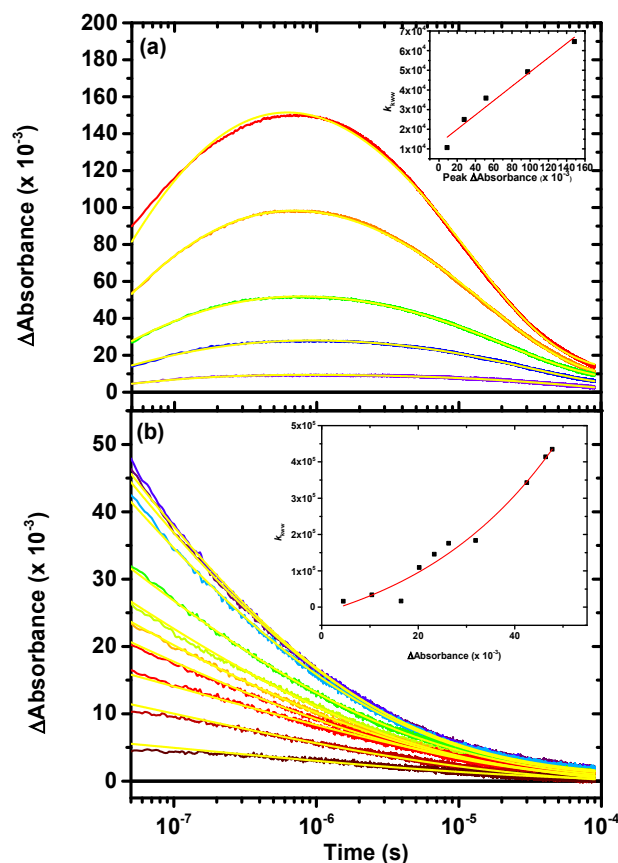


Figure 4.5: Single wavelength absorption change measured after pulsed like excitation of **f-TPA** (a) and **a-TPA** (b) at various laser fluencies. Insets represent the abstracted rate constant versus the magnitude of the absorption changes.

In order to assess the influence of surface anchoring on the interfacial electron transfer (Equation 4.1), the oxidized TPA concentration was monitored at 670 and 675 nm for the **f-TPA** and **a-TPA** respectively.



Interfacial electron transfer to the **f-TPA** was complicated by delayed regeneration, which results in a bi-phasic kinetic profile consisting of an initial growth followed by a decay. Both phases were dispersive in nature, and two Kohlrausch-Williams-Watts (KWW) stretched exponential functions were utilized to model the kinetic data. In order to assist with the

modeling, the oxidized sensitizer concentration was monitored at 412 nm as these data report on the same regeneration process as the initial rise in the **f-TPA⁺** data (**Figure S17**). The kinetics associated with the oxidized sensitizer were modeled using a single KWW function (**Equation 2**). Best fits were found by fixing $\beta = 0.3$, while k was allowed to float. The values for β and k obtained from the 412 nm data were then applied as β_1 and k_1 in the bi-KWW function used to model the 670 nm traces. A value of $\beta_2 = 0.7$ was found to provide the best fits to the kinetic data. An average rate constant, k_{kww} , was abstracted from these data using **Equation 4.3**. This value represents the first moment of the underlying Levy distribution.

$$\Delta A = \sum \Delta A_n e^{-(k_n t)^{\beta_n}} \quad (4.2)$$

$$k_{kww} = \frac{k\beta}{\Gamma(\frac{1}{\beta})} \quad (4.3)$$

The kinetics for recombination to **a-TPA** was modeled by a single KWW function. In contrast to the free TPA, a value of $\beta = 0.17$ provided the best fits. These recombination kinetics more closely resemble those of commonly used sensitizers.^{56,89,90}

The disparity in the values of β suggests that recombination to surface anchored acceptors are governed by fundamentally difference processes than those that are unanchored. The exact meaning of a specific β value remains unknown, despite significant effort to understand it.^{58,101,125,126} Recently, a Monte Carlo simulation based study on sensitizer regeneration found that reactions that were more limited by diffusion required lower values for β , while reactions controlled by the electron transfer event had β near unity.¹⁷⁵ This suggests that recombination to **a-TPA** is limited more by electron diffusion rather than electron transfer.

The number of electrons present in TiO₂ is known to influence the recombination rate.^{60,176} To this end, recombination process was investigated over a wide range of laser fluencies to tune the number of injected electron. The inset in both **Figure 4.4a** and **Figure 4.4b** shows the abstracted average rate constants plotted as a function of the maximum absorbance change. Since after regeneration, the number of oxidized TPA must necessarily equal number of injected electrons, the absorption of TPA⁺ is linearly proportional to the number of electrons in the TiO₂ through Beer's law. An increased recombination rate was observed with increased irradiance for both ***f*-TPA** and ***a*-TPA**. However, a much larger increase was seen for ***a*-TPA** (10-fold increase) compared to ***f*-TPA** (4-fold increase) when varied over a similar range of concentration. The increase in rate for the ***f*-TPA** was approximately linearly dependent in the irradiance. Though the corresponding data for ***a*-TPA** could be modeled with linear fit, an exponential model provided a better fit. These observations again highlight the often-undiscussed influence that surface attachment can have on interfacial electron transfer.

To gain further information on the energetics that govern this charge recombination process and the influence of surface transient measurements were carried out over a range of temperatures (**Figure 4.5**), which allowed an activation energy, E_a , for the reaction to be determined. A wider range of temperatures was available for the ***a*-TPA** (303 K – 233 K), since the ***f*-TPA** began to precipitate at temperatures below 258 K.

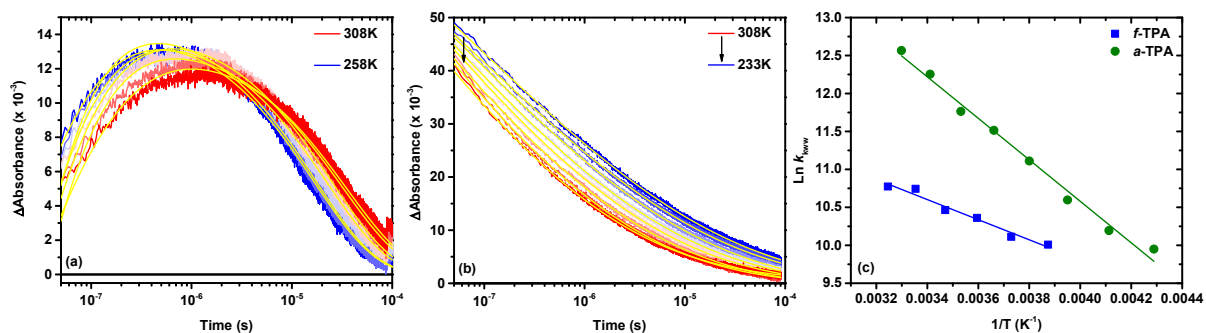


Figure 4.6: Single wavelength kinetics of *f*-TPA (a) and *a*-TPA (b) at various temperatures. Arrhenius plot (c) for *f*-TPA (blue squares) and *a*-TPA (green circles)

The observed kinetics could be modeled using the previously described procedure. Plots of the natural logarithm of k_{kww} versus the inverse of temperature (**Figure 4.6 c**) gives rise to a linear behavior whose slope corresponds to $-E_a/R$. Hence, these measurements allowed E_a determination for recombination from TiO_2 to *f*-TPA⁺ and *a*-TPA⁺ of $12 \pm 2 \text{ kJ mol}^{-1}$ and $23 \pm 1 \text{ kJ mol}^{-1}$, respectively. Measurements taken under different irradiances showed the same activation energies. This significant difference provides further insight into both recombination processes. It is worth noting that processes occurring within the TiO_2 (i.e. electron transport) are expected to be independent of whether the TPA is anchored to the surface or is free in solution. Additionally, as mentioned above, the redox potentials between *a*-TPA and *f*-TPA are nearly identical (see **Table 4.1**), which suggest that their contribution to the driving force for recombination are also nearly identical. Rational for the differences in activation energy is discussed below.

According to the Marcus equation, the rate of electron transfer is governed by the driving force for the reaction (ΔG), the electronic coupling (H_{ab}), the reorganization energy (λ), and the temperature (T). A key difference between the *f*-TPA and *a*-TPA are molecular orientations relative to the TiO_2 . The methylene spacer present on the *a*-TPA likely restricts

TPA orientation to be nearly normal to the surface, while the ***f*-TPA** is free to adopt whatever orientation it prefers. The normal orientation of the ***a*-TPA** likely inhibits significant electronic coupling between the interface and the molecule's π system. This in turn will reduce the electronic coupling between the TPA and the interface. In contrast, the ***f*-TPA** can obtain geometries that could enhance electronic coupling between the π system and the TiO₂. Based on this logic, a higher electronic coupling for the ***f*-TPA** relative to the ***a*-TPA** is expected. Binding may also introduce an additional barrier to recombination, since the negative charge on the anchoring group can introduce a columbic penalty to recombination. Given the similar structure between the two molecules, the total reorganization energy is assumed to be at parity.

Electron transport in TiO₂ is believed to occur through a multiple trapping/detrapping mechanism, where an electron localizes at a given trap state requiring thermal activation to a conduction band to allow for transport. We assert that TiO₂(e⁻) must access higher energy states in order to efficaciously recombine with ***a*-TPA** when compared to ***f*-TPA**, in order to overcome the additional barrier observed for recombination, **Figure 4.7**. This would require more trapping/detrapping events within the TiO₂ prior to a recombination event, leading to a more diffusive recombination process which would in turn lower the β value. As the driving force for this reaction increases, more states should be available for recombination which would increase the values for β . Indeed in an analogous study the kinetics for charge recombination to tris-(4-bromophenyl)amine (data not shown) were well described by a single exponential function ($\beta = 1$). This acceptor has a TPA⁺⁰ potential of 1.4 V vs NHE, which would increase the number of states capable of recombination, consistent with the proposed model.

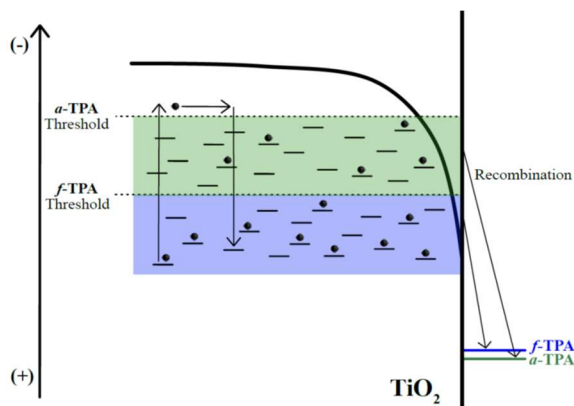


Figure 4.7: Schematic representation of the charge recombination processes for *a*-TPA and *f*-TPA

This model agrees qualitatively with previous observation on the recombination process. It has been shown that applying an electrochemical bias to a TiO₂ film results in more rapid and less dispersive recombination. The electrochemical bias would preferentially fill the lower energy electron accepting states in the TiO₂, which would increase population of electrons capable of recombining after light irradiation.

4.4 Conclusions

In conclusion, we communicated here on the first fundamental study that investigates the interfacial electron transfer between TiO₂ and redox tri-phenylamine mediators, that share the same redox potential and structural features, but that are either free in solution or anchored on TiO₂. We have been able to show instantaneous regeneration of the oxidized **RuP** sensitizer when TPA is co-sensitized on TiO₂. We have shown that main differences exist in the behavior, kinetics and energetics of *a*-TPA and *f*-TPA and have given plausible explanation as to why these trends are observed. Efforts are currently undertaken in order to investigate the driving force dependency of this recombination processes as well as to understand the main discrepancy that exist between mediator in solution and anchored at the surface.

Chapter 5: Driving Force Dependent Charge Recombination to Solution Phase Triphenylamine Redox Mediators

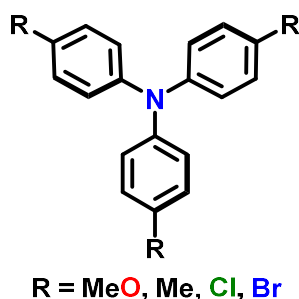
5.1 Introduction

Control of electron transfer occurring at illuminated semiconductor interfaces has practical significance in addition to being fundamentally important.^{21,105,120,133,172,177} For example, photoinduced electron transfer between molecular chromophores or ‘sensitizers’, and mesoporous thin films of nanocrystalline TiO₂ is utilized in dye sensitized solar cells (DSSCs) that convert solar irradiance into useful forms of energy.^{33,38} In DSSCs, the photogenerated electron must move through the mesoporous TiO₂ film without being intercepted by an oxidized sensitizer or a solution phase redox mediator, a process known as charge recombination. The redox mediator is present in the electrolyte to regenerate the sensitizer and transport the oxidizing equivalent, or ‘hole’, to the counter electrode. Understanding and impeding these charge recombination reactions has been the focus of numerous studies.^{30,36,38,120,178} Despite this, the recombination reaction remains poorly understood.

The role of the free energy change that occurs during charge recombination is not well understood.^{57,121,123,124,179,180} An experimental difficulty is relating the observed rate constants, abstracted from time resolved kinetic data to the actual interfacial electron transfer step. This is likely due to a large dependence of these reactions on electron diffusion rates within the TiO₂.¹²⁶ The majority of driving force studies have focused on recombination to surface

anchored sensitizers, and not solution phase redox mediators. In Chapter 4, it was shown that recombination to a surface anchored acceptor is fundamentally different than recombination to solution phase redox mediators.¹⁸¹ To that end, this study is focused on interfacial electron transfer from TiO₂ to a series of symmetrically substituted triphenylamine electron acceptors, **Scheme 5.1**. The TPA were substituted at the *para*-position of each phenyl ring with electron donating/withdrawing functional groups that allowed the TPA⁺⁰ reduction potential to be varied by ~ 0.5 V.

Scheme 5.1: Structure of the triphenylamines used throughout these studies.



5.2 Experimental Section

Materials: The following reagents and solvents were purchased from the listed commercial sources and used without further purification: acetonitrile (Burdick and Jackson, spectrophotometric grade), methanol (Fischer, ACS Reagent grade), sodium perchlorate (NaClO₄, Sigma-Aldrich, 99%), argon gas (Airgas, >99.998%), [Ru(2,2'-bipyridine)₂(4,4'-dicarboxy 2,2'-bipyridine)](PF₆)₂ (Solaronix), tri-*p*-tolyl- amine (**Me**-TPA, Sigma-Aldrich, 97%), tris (4-bromophenyl)amine (**Br**-TPA, Sigma-Aldrich, 98%). Tri-*p*-anisylamine (**MeO**-TPA)¹⁸² and tris (4-chlorophenyl)amine (**Cl**-TPA)¹⁸³ were prepared according to previously reported methods and a pure crystalline product of the compounds could be obtained by recrystallization from hot hexanes.

Materials Preparation: Anatase TiO₂ nanocrystallites were prepared through a previously described sol-gel method.¹⁴¹ The sols were casted as thin films by doctor blading onto methanol cleaned glass substrates. Scotch tape (~ 10 μ m) was used as a spacer and aided in achieving a uniform film thickness. The films were allowed to stand covered for ~30 min before being transferred to a tube furnace. The furnace was first purged with pure O₂, then heated to 450°C for 30 min. After annealing, the films were either kept in a 70°C oven for later use, or immediately submerged in concentrated acetonitrile solution of [Ru(bpy)₂(dcb)](PF₆)₂.

Electrochemistry: All electrochemical experiments were performed in acetonitrile solutions containing 0.1 M NaClO₄ as the supporting electrolyte. Potentials were applied against a self-contained Ag wire pseudo reference electrode containing the same electrolyte solution. The reference electrode was calibrated externally against the Fc⁺⁰ reduction potential (0.31 V vs SCE in 0.2 M LiClO₄).¹⁴⁹ Solution electrochemistry employed Pt disk electrodes (BASi, 1.6 mm diameter) as both working and auxiliary electrodes. A Au Honeycomb Spectroelectrochemical Cell (Pine Research Instrumentation) was used during spectroelectrochemical studies, and allowed absorption changes to be quantified after application of an electrochemical bias.

Absorption Spectra: Ground state absorption spectra were obtained from a Varian Cary 50 spectrophotometer. Serial dilution of stock solution was used to determine the extinction coefficient of each compound.

Transient Absorption: Nanosecond transient absorption measurements were performed on a previously described apparatus.¹⁶⁸ A summary of this apparatus follows. A pulsed (1 Hz) 150 W xenon arc lamp (Applied Photophysics) was used as the probe beam. Appropriate filters were placed before the sample to minimize sample excitation. After passing through the

sample, the probe beam was focused into a Spex monochromator coupled to a R928 Hamamatsu photomultiplier tube. A pulsed (1 Hz) Nd:YAG laser (Quantel U.S.A. Brilliant B; 5-6 ns full width at half-maximum, spot size $\sim 0.8 \text{ cm}^2$) provided sample excitation. Excitation power was measured at the sample using a thermopile power meter (Molelectron), with typical excitation powers varying between 500 μJ - 5 mJ/pulse. Typically, 30 pump-probe measurements were averaged over the range of 400 – 800 nm. Data generated for kinetic modeling typically averaged between 150 – 210 measurements in order to improve signal to noise. Full spectra were generated at a set time after laser excitation by averaging 3 – 21 data points around the timepoint of interest.

Data Modeling: Kinetic modeling was performed with OriginPro 9, which utilizes a Levenberg-Marquardt iteration method. A custom Mathematic 9 script was used to modeling the spectral signatures observed in transient absorption. Fitting was achieved through standard addition of steady state absorption spectra.

5.3 Results

Mesoporous nanocrystalline TiO_2 thin films were sensitized to visible light with $\text{Ru}(\text{bpy})_2(\text{dcb})^{2+}$ by immersion into concentrated ($\sim \text{mM}$) CH_3CN sensitizer solutions. These films were soaked for a minimum of 24 h to ensure that saturation surface coverages were obtained. The sensitized films, abbreviated $\text{TiO}_2|\text{S}$, displayed the characteristic metal-to-ligand charge transfer (MLCT) feature observed for the parent Ru compound. A bathochromic shift in this feature has observed upon the addition of 0.1 M NaClO_4 to a neat acetonitrile solution. This absorption shift was previously been assigned to a change in the local electric field present at the TiO_2 interface upon cation adsorption.⁷⁶

The neutral form of the TPAs used throughout this study absorbed little visible light, though strong absorption features were present in the UV region. The TPA extinction coefficients for these features were quantified through serial dilution of concentrated stock solutions. The $\text{TPA}^{+/0}$ reduction potential was determined through cyclic voltammetry measured in 0.1 M NaClO_4 acetonitrile, **Figure 5.1**. The spectra of the one electron oxidized form of these compounds were then quantified through spectroelectrochemical measurements, where the absorption changes were monitored after the application of electrochemical bias ~ 300 mV positive of the $\text{TPA}^{+/0}$ reduction potential.

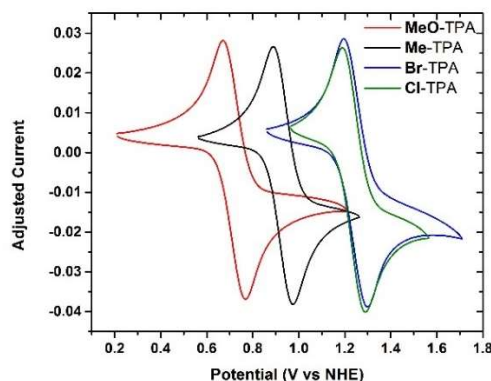


Figure 5.1: Cyclic voltammograms performed for each TPA in acetonitrile solutions.

Oxidization was assumed to be complete when the spectral changes become invariant with time. Each TPA possessed a strong red absorption feature, centered between 600-800 nm. The extinction coefficients for these absorptions were determined by comparison to the neutral form, **Figure 5.2**. A summary of the $E^0(\text{TPA}^{+/0})$ reduction potential, and the peak position and extinction coefficient for the TPA^+ spectra for species can be found in **Table 5.1**.

Nanosecond transient absorption was performed on the sensitized TiO_2 thin films in argon purged acetonitrile electrolytes containing 0.1 M NaClO_4 and 8 mM of a given TPA. The NaClO_4 was introduced to improve the injection yield.^{81,108} **Figure 5.3** shows the absorption

changes observed after pulsed light excitation of $\text{TiO}_2|\text{S}$ in the presence of **MeO**-TPA. These kinetics were separated into a regenerative phase, $\text{TiO}_2(\text{e}^-)|\text{S}^+ + \text{MeO-TPA} \rightarrow \text{TiO}_2(\text{e}^-)|\text{S} + \text{MeO-TPA}^+$, and a recombination phase, $\text{TiO}_2(\text{e}^-)|\text{S} + \text{MeO-TPA}^+ \rightarrow \text{TiO}_2|\text{S} + \text{MeO-TPA}$.

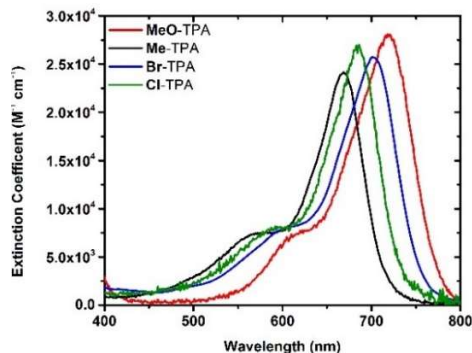


Figure 5.2: Absorption spectra generated for TPA^+ in acetonitrile electrolytes.

Table 5.1: Summary of electrochemical, spectroscopic and kinetic data.

	$E^0(\text{TPA}^{+/0})$ (V vs NHE)	Peak Absorbance (nm)	Extinction Coefficient ($\text{M}^{-1} \text{cm}^{-1}$)	k (s^{-1}), β	k_{kw} (s^{-1})
MeO-TPA	0.72	717	2.8×10^4	0.42×10^5 , 0.67	0.47×10^5
Me-TPA	0.93	668	2.4×10^4	1.5×10^5 , 0.74	1.7×10^5
Cl-TPA	1.24	685	2.7×10^4	12×10^5 , 1	12×10^5
Br-TPA	1.25	702	2.6×10^4	9.7×10^5 , 1	9.7×10^5

The transient spectra were modeled using: (1) the difference spectra between $\text{TiO}_2|\text{S}$ and $\text{TiO}_2|\text{S}^+$; (2) the TPA^+ spectra; and (3) the shift in the MLCT feature upon the addition of NaClO_4 . The third component accounts for a shift in the sensitizer absorption caused by an electric field generated by injected electrons (Stark effect).^{68,152} Features associated with the oxidized sensitizer decayed rapidly, with the spectra beyond 1 μs being well modeled using a combination of (2) and (3) only, **Figure 1B**. An analogous observation was made for Me-TPA, with regeneration being complete by $\sim 1 \mu\text{s}$.

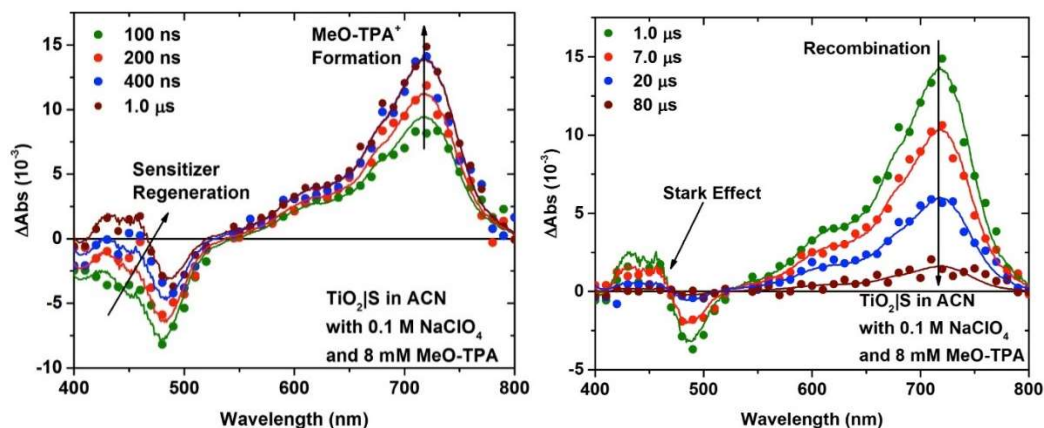


Figure 5.3: Transient absorption spectra generated for TiO_2/S submerged in 8 mM **MeO**-TPA at early (A) and late timescales (B)

Shown in **Figure 5.4** are the analogous absorption features observed after pulsed light excitation of TiO_2/S submerged in the presence of **Cl**-TPA. Unlike **Me**- and **MeO**-TPA, complete sensitizer regeneration was not observed. Incomplete regeneration was also evident with **Br**-TPA. The incomplete regeneration is likely due to the small regeneration driving force.

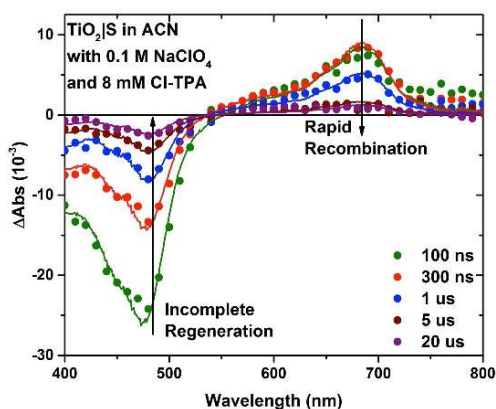


Figure 5.4: Transient absorption spectra generated after pulsed light excitation of TiO_2/S in the presence of 8 mM **Cl**-TPA

Shown in **Figure 5.5** are the absorption changes monitored at the peak absorption for each TPA^+ after pulsed like excitation of $\text{TiO}_2|\text{S}$, which reports on the interfacial electron transfer reaction rate $\text{TiO}_2(e^-) + \text{TPA}^+ \rightarrow \text{TiO}_2 + \text{TPA}$. The kinetics observed for **MeO-** and **Me-TPA** were biphasic, consisting of an initial rise followed by a decay. The signature for both **Cl-TPA** and **Br-TPA** showed a small growth followed by a decay. Both kinetic phases for **MeO-** and **Me-TPA** were dispersive in nature, requiring two Kohlrausch-Williams-Watts (KWW) stretched exponential functions to adequately model, **Equation 5.1**. The first KWW function corresponds to the regeneration phase of the profile. As a result, the concentration of $\text{TiO}_2|\text{S}^+$ was monitored at an isosbestic point for the Stark effect. This profile was fit to a single KWW function, and the value for β and k obtained were applied to the bi-KWW function used to model the TPA^+ kinetics as β_1 and k_1 .

$$\Delta A = \sum_{i=1}^n \Delta A_n e^{-(k_n t)^{\beta_n}} \quad (5.1)$$

In this equation, β is related to the width of an underlying Levy distribution of rate constants, with values between 0 and 1. An “average” rate constant, k_{kww} , was calculated as the first moment of this distribution using **Equation 5.2**, where Γ is the so-called Gamma function.

$$k_{kww} = \frac{k_i \beta}{\Gamma(1/\beta)} \quad (5.2)$$

Unlike **MeO-** and **Me-TPA**, the decay profile for **Cl-TPA** and **Br-TPA** was modeled with the KWW model with $\beta = 1$. This represents a unique observation, as recombination kinetics are rarely described by simple kinetic models such as single exponentials.

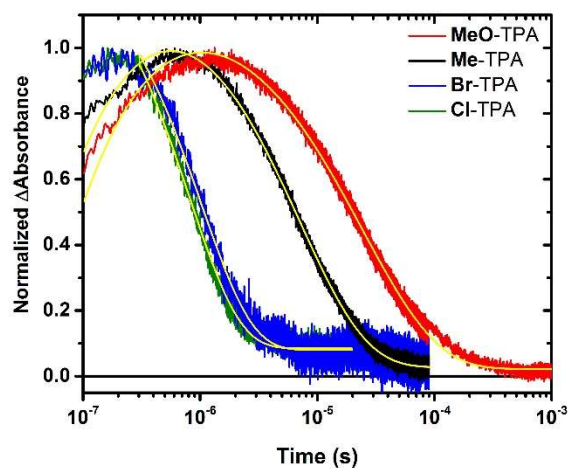


Figure 5.5: Recombination kinetics to TPA^+ . Overlaid are the best fits to these kinetic traces.

To investigate this further, the recombination reaction was monitored as a function of the incident irradiance, **Figure 5.6**. It was found that one value of k could be used to model all the kinetic data.

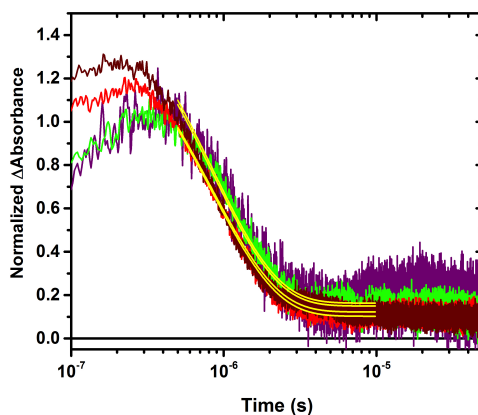


Figure 5.6: Normalized recombination kinetics observed for Cl-TPA

5.4 Discussion:

The recombination reactions $\text{TiO}_2(e^-) + \text{TPA}^+ \rightarrow \text{TiO}_2 + \text{TPA}$ was monitored for a series of symmetrically substituted triphenylamines. This reaction represents an unwanted process

that occurs during the operations of a DSSC. Key features for the TPA series is the significant (~ 0.5 V) change in redox potential as well as their structural similarities. Several previous studies have sought to understand the role of driving force on the recombination rate to a solution phase acceptor^{57,135}, though this study differs in two significant ways. The data presented here were not made on fully assembled DSSCs, but on the mesoporous thin films immersed in CH_3N electrolytes with the redox mediator present. This allows for a direct observation of recombination. The mediators studied here also possess the most positive redox potentials reported.

The charge separated state $\text{TiO}_2(\text{e}^-)|\text{S}^+$ was generated on a sub nanosecond timescale after pulsed light irradiation of the sensitized thin films. Sensitizer regeneration afforded the desired charge separated state $\text{TiO}_2(\text{e}^-)|\text{S} + \text{TPA}^+$. Regeneration rates have been shown to follow the Marcus equation.^{44,184} Under conditions where the mediator concentrations are too low or the rate of diffusion of the mediator is slow, this reaction can become diffusion limited.^{175,184} Full sensitizer regeneration was observed for both **MeO**- and **Me**-TPA with regeneration rates that qualitatively followed Marcus normal region behavior, with more rapid regeneration occurring for **MeO**-TPA relative to **Me**-TPA. Incomplete regeneration was observed for both **Cl**- and **Br**-TPA, likely due to the small driving force for regeneration (~ 0.1 V) and the low TPA concentration (8 mM).

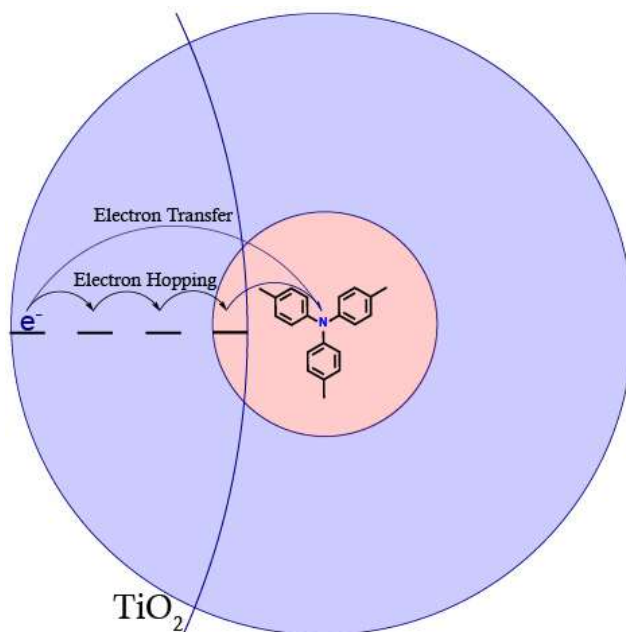
The oxidized TPA concentration was monitored as a function of time at the peak absorption wavelength. The **Me**- and **MeO**- TPA showed bi-phasic kinetics, where the concentration initially increased through sensitizer regeneration, and then decreased as recombination progressed. The growth was correlated to the decay of the oxidized sensitizer, which allowed the recombination rate to be determined without complications. A clear trend

in the recombination kinetics was identified: **Cl-TPA** \sim **Br-TPA** > **Me-TPA** > **MeO-TPA**. Given the similar structure for each acceptor, the recombination kinetics are attributed to the change in driving force of the reaction, consistent with Marcus normal region behavior. The key parameter for determining whether a reaction will occur in the Marcus normal region (i.e. increased rate with increased driving force) or the Marcus inverted region (i.e. decreased rate with increasing driving force) is the magnitude of the total reorganization energy compared to the reaction driving force. Though experimental values for TPA reorganization energy have not been reported, calculated values based on DFT put this parameter at ~ 0.3 eV.¹⁸⁵ Unfortunately, defining the reorganization energy at a nanocrystalline interface is difficult, yet solvent and electrolyte reorganization (outer sphere) as well as bond rearrangements (inner sphere) are expected to contribute.

Defining the recombination driving force is also difficult, being dependent on the TPA⁺⁰ reduction potential and the TiO₂ quasi-Fermi level.⁵⁷ The electron accepting states in TiO₂ are well modeled with an exponential function⁷⁶, implying that the reducing power of electrons in TiO₂ is highly sensitive to the number of TiO₂(e⁻). Additionally, the electrons in the TiO₂ are consumed throughout the reaction, meaning the driving force changes during charge recombination. If we assume that the acceptor states with the lowest energy are at ~ 0 V vs NHE, we can crudely estimate the driving force for the reaction as the TPA⁺⁰ reduction potential. Interestingly, the driving force exceeds the expected reorganization energy, and therefore inverted region behavior was expected. It is worth noting that a report by Hupp et al. showed normal region behavior for recombination from TiO₂ to a ferrocene series despite the small reorganization energy for the reaction compared to the recombination driving force.⁵⁷

The recombination kinetics were best modeled with a KWW function, where the values for β represent a distribution of rate constants. The stretched nature of the kinetics is often attributed to electron diffusion through the TiO_2 , which is believed to be governed by a trapping/detrapping mechanism.¹²⁶ This mechanism requires localized electrons to thermally access the conduction band, which grant the electron mobility until it ultimately traps in another localized state. In addition to an increase in the recombination reaction with driving force, the value for β was also found to increase, reaching a value of 1 for both **Cl**- and **Br**-TPA. This is a remarkable result since to our knowledge this represents the first example of an interfacial first-order recombination reaction.

Scheme 5.2: Schematic representation of the proposed Perrin-like model. When the recombination driving force is large (as seen for Br- and Cl-TPA), electrons can undergo an electron transfer over relatively large distances (Blue circle). Thus, fewer electron hops are required for the electron transfer to occur, leading to larger β values. When there is less driving force for recombination, the electron must hop closer to the TPA acceptor for electron transfer to occur (Red circle).



In Chapter 4, a study that sought to understand the influence of surface anchoring has on interfacial electron transfer. It was reported that surface anchoring led to more diffusive

kinetics ($\beta = 0.17$) and higher activation energies when compared to an analogous molecule that were free in solution. We propose that these two observations resulted from a higher barrier for recombination to surface anchored acceptors. First order kinetics were also predicted if minimal diffusion was observed.

Electron transfer rates are known to exponentially decrease with increasing distance between the donor and acceptor.¹³⁸ The driving force for electron transfer can be used to compensate for an increase in the distance between the donor and acceptor. Based on this, we proposed that that electron transfer reactions studied here follow a Perrin-like model, where $\text{TiO}_2(e^-)$ within a certain distance, r_{rec} , of the TPA acceptor will undergo electron transfer, while those outside this distance will not, **Scheme 5.2**. Increasing the electron transfer driving force also increases r_{rec} . If the driving force is large, as seen for **Cl-** and **Br-TPA**, the $\text{TiO}_2(e^-)$ can recombine with the TPA acceptor without significant movement by either the electron or acceptor. As the electron transfer driving force decreases, the electron must hop more times to fall within r_{rec} , leading to lower values for b . This is consistent with observations made for **Me-** and **MeO-TPA** that saw slower recombination kinetics and lower β values with decreasing driving force.

5.5 Conclusion:

Charge recombination was monitored to a series of symmetrically substituted triphenylamines where $\text{TPA}^{+/0}$ reduction potential varied by ~ 0.5 V. An increase in the recombination rate was seen with increased thermodynamic driving force, consistent with the reaction occurring in the Marcus normal region. This was surprising since the reorganization energy was expected to be smaller than the driving force. Recombination reactions between

TiO₂ nanocrystallites and molecular acceptors are known to have a large diffusive component, as the electron is phase separated from the oxidized molecule.

Chapter 6: Influence of Lewis Acidic Cations and Phantom Electrons on Charge Recombination from Nanocrystalline SnO₂ Thin Films

Work in Collaboration with Renato N. Sampaio, Timothy J. Barr and Erica M. James

6.1 Introduction

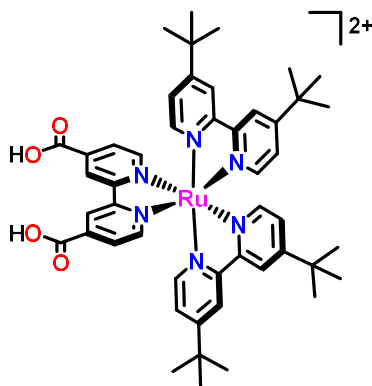
Dye sensitized solar cells (DSSCs) combine the robustness of wide-bandgap semiconductors with broadly absorbing, tunable, molecular sensitizers as a means of converting solar irradiance into electrical energy. A typical DSSC utilizes a mesoporous thin film of anatase nanocrystalline TiO₂ to facilitate charge separation and transport. Recently, there has been renewed interest in employing nanocrystalline rutile SnO₂ as a replacement for TiO₂, due to its ~100x higher electron diffusion coefficient and ~0.5 eV lower energy electron accepting states.^{130,186,187} Despite significant effort, TiO₂ still remains the semiconductor used in champion devices.³⁴ The reduced performance of SnO₂ is often attributed to increased charge recombination rates, in which the injected electron is captured by an oxidized sensitizer or solution phase redox mediator prior to collection.^{130,136} Surface passivation techniques, such as atomic layer deposition, have been shown to impede back electron transfer leading to improved device performance.^{21,136} Despite their poor performance in DSSCs, these surface passivated electrodes have been used with great success in dye sensitized photoelectrosynthetic cells.^{21,22} This success merits further investigation and optimization of SnO₂ for applications in DSSCs.

Electrolyte composition is known to significantly alter the performance of DSSCs. Lewis acidic cations are a common electrolyte additives, as these cation are known to alter

sensitizer injection yields by shifting the energy of the electron accepting states to more positive values.^{67,96,106,108} These cations are also known to impact the rate of charge recombination to oxidized sensitizers and solution phase redox mediators.^{59,152,153} We recently reported that Lewis acidic cations also lower the energy of electron accepting states in nanocrystalline SnO₂ thin films, analogous to observations made for TiO₂.¹⁰⁰ Additionally, a population of acceptor states that do not absorb in the UV-Vis region was discovered. We termed these states as ‘phantom electrons’. This chapter is focused on understanding how cation identity can influence interfacial electron transfer from SnO₂ nanocrystallites, and whether phantom electron participate in the charge recombination process.

6.2 Results and Discussion

Thin films of mesoporous nanocrystalline TiO₂ and SnO₂ were prepared according to previously reported methods,^{105,141} and were sensitized to visible light by submersion into concentrated (~ mM) acetonitrile solutions of the sensitizer [Ru(dtb)₂(dcb)](PF₆)₂, where dtb = 4,4’-di-*tert*-butyl 2,2’- bipyridine and dcb = 4,4’-dicarboxy 2,2’ – bipyridine), **Scheme 6.1**. This sensitizer was prepared according to a previous study¹⁴⁸, and was selected because it is known to give rise to significant absorption changes in the presence of interfacial electric



Scheme 6.1: Structure of $[\text{Ru}(\text{dtb})_2(\text{dcb})]^{2+}$

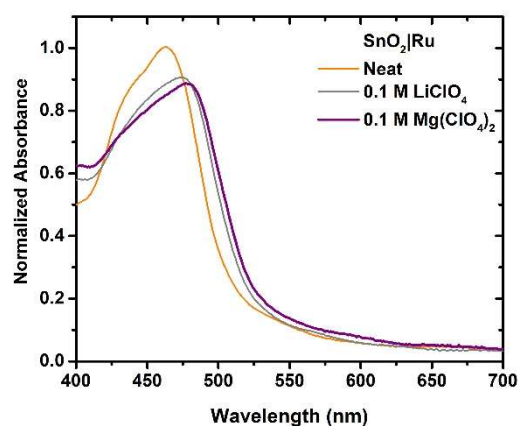


Figure 6.1: UV-Vis absorption changes for SnO_2/Ru films submerged in acetonitrile electrolytes. The spectral taking in LiClO_4 and $\text{Mg}(\text{ClO}_4)_2$ were normalized relative to the sample in neat acetonitrile.

fields.^{64,81} The sensitized films, abbreviated as SnO_2/Ru , TiO_2/Ru or the generic MO_2/Ru , displayed the characteristic metal-to-ligand charge transfer (MLCT) feature of the **Ru** sensitizer. Surface coverages were determined using **Equation 6.1**⁸⁶, where ε is the peak extinction coefficient ($16400 \text{ M}^{-1} \text{ cm}^{-1}$ at 465 nm).⁷⁶ Higher surface coverages were generally observed for TiO_2 ($\sim 8 \times 10^{-8} \text{ mol}^{-1} \text{ cm}^{-2}$) when compared to SnO_2 ($\sim 4 \times 10^{-8} \text{ mol cm}^{-2}$). Lower surface coverages for SnO_2 relative to TiO_2 have been reported previously and have been attributed to a lower isoelectronic point for SnO_2 .¹⁸⁸

$$Abs = 1000 \times \varepsilon \times \Gamma \quad (6.1)$$

The addition of 0.1 M LiClO₄ or Mg(ClO₄)₂ to the acetonitrile electrolyte resulted in a bathochromic shift in the MLCT transition, with a larger shift observed for Mg(ClO₄)₂ compared to LiClO₄, **Figure 6.1**. These shifts have been observed for several sensitizers anchored at TiO₂ interface^{76,74,152}, but the generality of this observation to other metal oxides has not been previously reported. The shifts have been attributed to changes in the local electric fields at the interface after cation adsorption, with the divalent Mg²⁺ causing a larger magnitude change relative to Li⁺. Though the exact nature of these interactions remains elusive, the cations were thought to be interacting with the residual negative charge of the TiO₂ interface, largely resulting from deprotonated surface hydroxyl groups.⁷⁶ However, given the similar shifts observed for TiO₂ and SnO₂ and given the large differences in surface charge, this assumption may be incorrect. It is possible that these cations are instead interacting with the negatively charged anchoring groups on the sensitizer. These interactions have been seen previously for similar Ru polypyridyl compounds in fluid acetonitrile solution.¹⁸⁹ Regardless of the exact nature of these interactions, the local electric field environment at the interface likely changes as a result of a cation interaction.

Nanosecond transient absorption measurements were performed on the sensitized thin films in argon purged acetonitrile electrolyte. Shown in **Figure 6.2A** are the absorption features observed after pulsed 532 nm light excitation of SnO₂|**Ru** in the presence of 0.25 M TBAI and 0.1 M LiClO₄. Pulse light excitation results in an electron transfer from excited sensitizer to the substrate, forming SnO₂(e⁻)|**Ru**⁺. The sensitizer is then rapidly regenerated through iodide

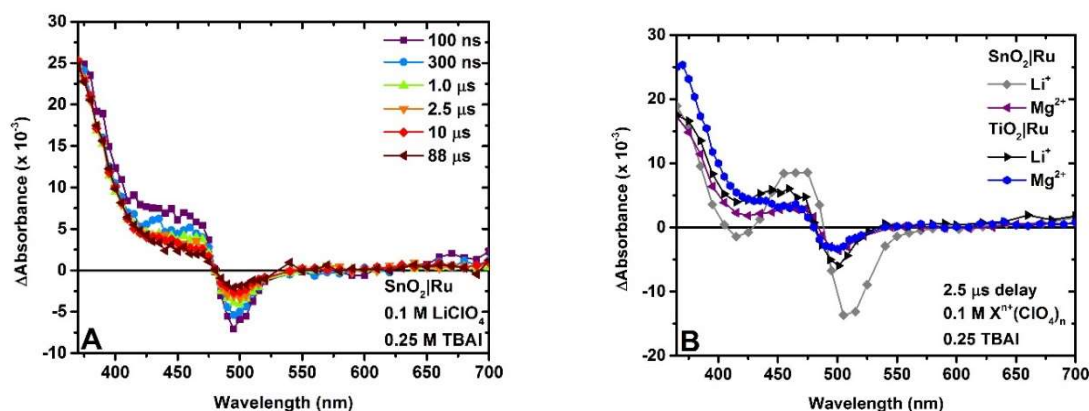


Figure 6.2: (A) Spectral changes observed after pulse light excitation of SnO_2/Ru submerged in argon purge acetonitrile containing 0.1 M LiClO_4 and 0.25 M TBAI. (B) Comparison of spectral changes 2.5 μs after excitation observed for TiO_2 and SnO_2 substrates in the presence of 0.25 M TBAI and either 0.1 M LiClO_4 or $\text{Mg}(\text{ClO}_4)_2$.

oxidation, with full regeneration being observed by $\sim 1 \mu\text{s}$. The oxidation of iodide to triiodide occurs through known disproportionation chemistry involved an $\text{I}_2^{\bullet-}$ intermediate.³⁹ Disproportionation was previously shown to occur at the same rate in the mesoporous of TiO_2 as in fluid solution ($3 \times 10^9 \text{ M}^{-1} \text{ s}^{-1}$)¹⁹⁰, and the SnO_2 was not expected to significantly alter this rate.

In addition to the absorption assigned to I_3^- (peak $\sim 370 \text{ nm}$), a first derivative shaped feature centered at $\sim 500 \text{ nm}$ was present. Some absorption due to $\text{MO}_2(e^-)$ was also observed at longer wavelengths.⁷⁶ Analogous spectral features could be seen for both substrates in both cation electrolytes, **Figure 6.2b**, though the relative magnitude of these features depended on the substrate and cation. The first derivative shape feature has been observed by several groups for TiO_2 thin films sensitized with a variety of organic and inorganic sensitizers.^{64,65,68,73} This feature has been assigned to a shift in the sensitizer's absorption spectrum in response to an electric field generated by the injected electron through a Stark or electric field effect. Assignment as a Stark effect has been supported by both spectroelectrochemical

measurements, where similar spectral signatures were observed upon reduction of sensitized films^{64,76,68}, and classical Stark spectroscopy, which monitored absorption changes in the presence of strong electric fields.⁶⁵ Given the similar shape of the feature for sensitized SnO₂, we conclude that sensitizers anchored at SnO₂ interfaces also experience a Stark effect induced by injected electrons.

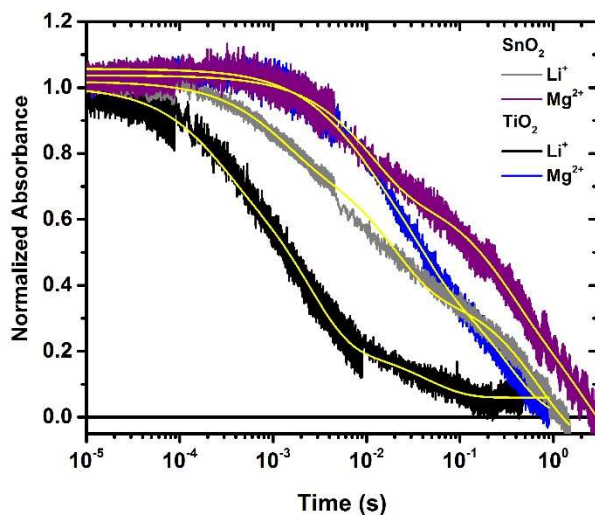


Figure 6.3: Recombination kinetics to I₃⁻ monitored at 375 nm. Overlaid are the best fits using a tri-exponential function.

Shown in **Figure 6.3** are the absorption changes associated monitored at 375 nm observed after pulsed light excitation of MO₂|Ru in the presence of either Li⁺ or Mg²⁺, which reported on the rate of the charge recombination reaction MO₂(e⁻) + I₃⁻ →. Although these kinetics are normalized for clarity, the maximum I₃⁻ absorption was kept at ~20 mOD for all samples. The kinetics for this reaction were well modeled using a sum of three exponentials, **Equation 6.2**, where an average rate constant could be abstracted using **Equation 6.3**.¹⁰⁵ In order to improve the accuracy of the fits, values for k_i were shared across multiple data sets for

the same cation and substrate while allowing the values for A_i to float. The values for $\langle k \rangle$ can be found in **Table 2**.

$$A(t) = A_1 e^{-k_1 t} + A_2 e^{-k_2 t} + A_3 e^{-k_3 t} \quad (6.2)$$

$$\langle \tau \rangle = 1/\langle k \rangle ; \langle \tau \rangle = \frac{\sum A_i \tau_i^2}{\sum A_i \tau_i} \quad (6.3)$$

Table 6.1: Values obtained from tri-exponential fit to recombination data.

$\langle k \rangle$ (s ⁻¹)	<u>SnO₂</u>		<u>TiO₂</u>	
	Li ⁺	Mg ²⁺	Li ⁺	Mg ²⁺
	1.9 ± 0.1	0.48 ± 0.01	90 ± 4	6.0 ± 0.3

Two observations became immediately apparent. The first was that the identity of the cation influenced charge recombination for both substrates. The second was the charge recombination occurs more slowly for SnO₂ compared to TiO₂ for under all conditions studied. The first observation agreed with previous results for TiO₂, and is discussed in more detail below.^{59,152} The slow recombination rate for SnO₂ compare to TiO₂ is surprising given previous results which reported that the opposite to be true.¹³⁰ In this previous report, recombination was monitored at wavelengths of 800 nm or longer, corresponding to the absorbance for MO₂(e⁻) as opposed to monitoring the primary electron acceptor, I₃⁻. As mentioned, we recently reported that at least two distinct electron accepting states exist in SnO₂, one of which does not absorb in the UV-Vis when populated.¹⁰⁰ This observation calls into question whether monitoring charge recombination through the long wavelength absorption of the electrons is valid for SnO₂ thin films. The role that these states play during charge recombination is currently unknown. For example, do electrons relax into so-called phantom states or does an equilibrium exist between the absorbing and non-absorbing states?

To address this, the recombination event was monitored at 375 nm for I_3^- and 800 nm for the electrons in the substrate. Shown in Figure 4 is such data taken for $\text{SnO}_2|\text{Ru}$ in 0.1 M $\text{Mg}(\text{ClO}_4)_2$. No significant differences were observed between these kinetics, both of which could be modeled with similar values of k_i . The same result was observed for all four samples. Two possible explanations for these results are: (1) The phantom states do not participate during photo-induced during photo-induced charge separation and recombination (2) a rapid

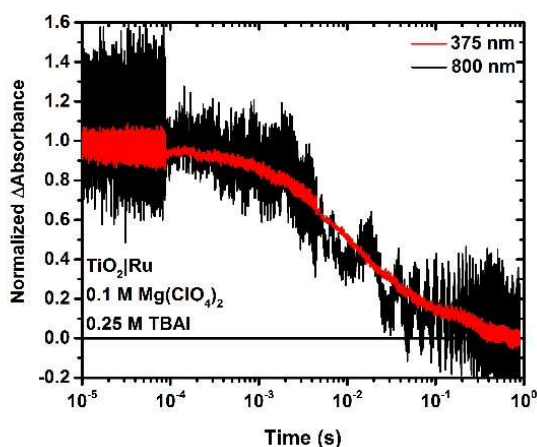


Figure 6.4: Comparison between the absorption measure at 375 and 800 nm at 100 μs .

equilibrium exists between the two $\text{SnO}_2(e^-)$ states such that they behave as a single state on the timescales of charge recombination. To gain a better understanding of the optically active states in both substrates, a comparison was made between the I_3^- absorption and $\text{MO}_2(e^-)$ over several laser intensities. The absorption was measured ~ 100 μs after excitation, which corresponded to a plateau region at both wavelengths. This data is found in **Figure 6.5**, where a clear linear relationship can be seen.

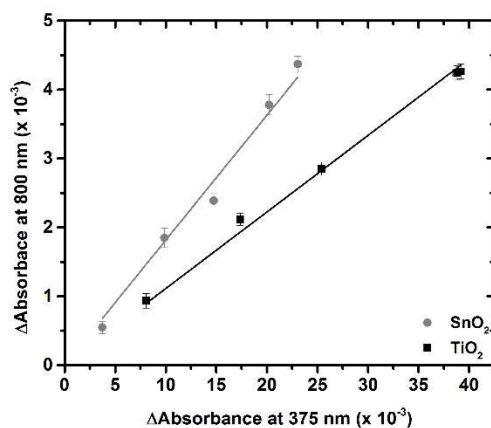


Figure 6.5: Absorption comparison between I_3^- and TiO_2 monitored $\sim 100 \mu s$ after pulse light excitation. Approximately $20 \mu s$ of data was averaged around this time point to improve signal to noise, and the error bars represent the observed standard deviation in this measurement.

An observed extinction coefficient for $MO_2(e^-)$ could be calculated based on slope using **Equation 6.4**.

$$\varepsilon_{e^-} = \frac{A_{e^-} - \varepsilon_{I_3^-}}{2 A_{I_3^-}} \quad (6.4)$$

In this equation, A_{e^-} and $A_{I_3^-}$ are the observed delta absorbance monitored at 800 nm and 375 nm respectively, which correspond to injected electrons and I_3^- . The factor of 2 accounts for the two-electron reduction required to reform I^- . The value for $\varepsilon_{I_3^-}$ at 375 nm is taken as $1.90 \times 10^4 \text{ M}^{-1} \text{ cm}^{-1}$ based on previous literature.³⁹ Extinction coefficient were determined to be 900 ± 100 and $2000 \pm 100 \text{ M}^{-1} \text{ cm}^{-1}$ for TiO_2 and SnO_2 respectively. The values for TiO_2 were consistent with values based on spectroelectrochemical measurements ($930 \text{ M}^{-1} \text{ cm}^{-1}$)⁷⁶, while the values observed for SnO_2 were significantly higher than those recently reported ($600 \text{ M}^{-1} \text{ cm}^{-1}$).¹⁰⁰ Values for SnO_2 were previously determined through spectroelectrochemical measurements, where the total within the films was correlated to the observed spectral changes. As mentioned, a potential window existed where a significant amount of charge was extracted without significant absorption changes. At more negative

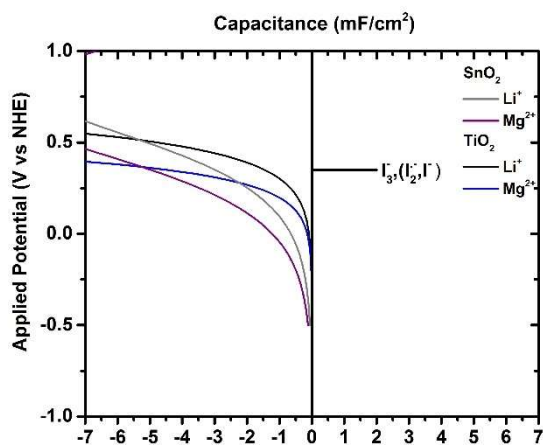
potentials, a linear relationship between absorption and charge was observed. We assumed that the majority of the charges over this potential range fell into optically active states, where the slope between extracted charge and absorbance reported on the electron extinction coefficient. The extinction coefficient abstracted from the data reported here suggests a larger fraction of optically active states play a role during recombination. It is possible that these states are spatially removed from optically inactive states, where electrons can only be injected into the optically active sites.

These observations do not account for the large discrepancy in recombination kinetics between our data and those previously reported.¹³⁰ One possible explanation are differences in electrolyte compositions. In the previous study, the authors introduced *tert*-butyl pyridine to their electrolyte solution, which is known to influence the electron accepting states in TiO₂.¹⁹¹ This effect may be more pronounced for nanocrystalline SnO₂, leading to significantly faster recombination.

The influence of Lewis acidic cations on interfacial electron transfer between TiO₂ and solution phase acceptors has been reported previously.^{59,152,192} Initially, a strong cation dependence was thought to arise primarily by an interaction between I₃⁻ and the electric field generated by electrons at the interface. The field experienced by the sensitizer is attenuated by the migration of cations towards the interface, with monovalent cations (Li⁺, Na⁺) showing a stronger response than divalent (Mg²⁺, Ca²⁺) cations. The trend in the electron transfer rate followed the screening trend, leading to the conclusion that the field must drive these interactions. However, the same trend was later observed for cationic mediators, which meant that the electric field could not solely account for the observed differences, **Chapter 3**.¹⁵²

The primary acceptor in our transient experiments was thought to be I_3^- due to the small concentration of $I_2^{\bullet-}$ expected based on equilibrium constants, as no I_2 was added to the system.^{39,59} The one electron reduction of I_3^- in acetonitrile is at -0.35 V vs NHE.³⁹ Shown in **Scheme 6.2** are the distribution of optically active electron accepting states observed through spectroelectrochemical measurements for both SnO_2 and TiO_2 in Li^+ and Mg^{2+} electrolytes.¹⁰⁰ Based on the low capacitance accumulated during these transient experiments, this recombination rate is likely thermodynamically uphill. Defining the driving force for this reaction is difficult, since the Fermi level likely changes throughout the reaction as the electrons in the substrate are depleted. The electrons are thought to move between acceptor states either through a trapping/detrapping or a hopping mechanism. Despite this, the energy of the electron states qualitatively follow the trend seen here, where a large barrier corresponds to slower kinetics. This also agrees with previous observations for recombination to organic mediators, where an increase in driving force corresponded to an increase in the rate. This assumes that these reactions occur within the Marcus normal region.

Scheme 6.2: Comparison of the I_3^- reduction potential and the distribution of optically active electron accepting states for SnO_2 or TiO_2 in Li^+ and Mg^{2+} based electrolytes.



6.3 Conclusions

In conclusion, we observed that cations added to an electrolyte solution induced a red shift in the MLCT feature of the surface anchored chromophore for sensitized TiO_2 and SnO_2 . Spectral features consistent with a Stark effect were observed for the first time on SnO_2 , confirming that the electrons in SnO_2 are also capable of generating significant electric fields. Charge recombination to I_3^- was shown to be slower for SnO_2 relative to TiO_2 in a given cation. This result stands at odds with previous reports¹³⁰, though this discrepancy is not well understood. We also assessed the role of phantom electrons seen for SnO_2 during electron recombination, and found that they do not play an appreciable role during this process.

Chapter 7: Excited State Dipoles Oriented Parallel and Anti-Parallel to TiO₂ Surface Electric Fields

Work in collaboration with Cassandra L. Ward and Ryan M. O'Donnell

7.1 Introduction

The incorporation of a molecularly sensitized mesoporous nanocrystalline metal oxide thin film as the photoanode in an efficient regenerative solar cell was first reported by Gratzel, and O'Regan over 25 years ago.³³ These devices, known as dye sensitized solar cells, (DSSCs), continue to be pursued for applications in solar energy conversion.^{36,38,120,193} In addition to molecules, sensitization can also be achieved using polymers,¹⁹⁴ quantum dots,¹⁹⁵ and/or inorganic solids.¹⁹⁶ Understanding the nature of the molecular excited state(s) that participated in electron transfer to the substrate is often difficult, given the rapid rate of electron transfer. Indeed there are now many reports of sub-picosecond electron transfer from molecular excited states to anatase TiO₂ nanocrystallites.^{36,177,197–199} The kinetics of electron transfer from Ru polypyridyl excited states are typically non-exponential, behavior that has recently been explained based on the energetic overlap between the molecular excited states and the electron accepting states in the semiconductor.³⁷ While ultrafast injection has garnered much experimental attention, it is also known that long-lived excited states can be observed under conditions where the semiconductor's acceptor states are energetically inaccessible.^{108,200} For example, molecules that are relatively weak photoreductants relative to the TiO₂ acceptor states may photoluminesce efficiently when anchored at the interface.^{37,201} The energetics of the acceptor states in metal oxides can also be tuned by pH or with other

potential determining cations, to increase or inhibit excited state injection.^{76,108,202} This chapter is focused on understanding the behavior of two ruthenium polypyridyl compounds with oppositely oriented metal-to-ligand charge transfer (MLCT) excited state dipole moments, which were anchored at the interface of nanocrystalline TiO₂. So-called ‘forward bias’ conditions, where electrons are electrochemically introduced into the mesoporous film, was used to study the interactions between these sensitizers and the TiO₂ mesoporous film in the presence of large electric fields generated by the electrons.

A curious observation first noted by O’Regan and coworkers was that surface anchored sensitizers began to photoluminescence more efficiently when the TiO₂ nanocrystallites were reduced with an applied electrochemical bias.¹⁹³ Early analysis concluded that sensitizer desorption caused this increased photoluminescence, a conclusion supported by quantitative quartz crystal microbalance measurements.²⁰³ The decreased electronic coupling that accompanied dye desorption was proposed to lower the excited state injection resulting in a higher quantum yield for radiative decay. While this interpretation agreed with the experimental observations, the same behavior was later observed for sensitizer that were insoluble in the external electrolyte. Furthermore, potential step experiments showed that the PL enhancements were reversible, suggesting that alternative and/or additional mechanisms were operative.

Here we report the excited state behavior of two Ru(II) polypyridyl compounds anchored to a mesoporous TiO₂ thin film, which was employed as the working electrode in a standard three electrode configuration. Throughout these experiments, the electrolyte was intentional modified to include different Lewis acidic cation containing salts. Lewis acidic cations are known to influence the energetics of the electron accepting states in the TiO₂.⁷⁶

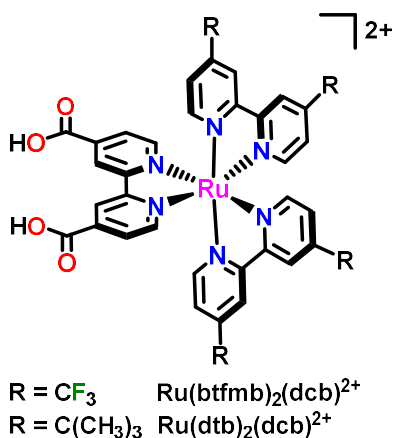
These two compounds were selected because their thermally equilibrated excited state dipoles are orientated differently with respect to the carboxylic acid binding groups. On the hours time scale of these experiments the degree of surface desorption was negligible enabling measurements under even more reducing conditions where a previously undocumented excited state quenching pathway was observed.

7.2 Experimental.

Materials. The following reagents and substrates were used as received from the indicated commercial suppliers: magnesium perchlorate ($\text{Mg}(\text{ClO}_4)_2$, Sigma-Aldrich, 99%), calcium perchlorate tetrahydrate ($\text{Ca}(\text{ClO}_4)_2 \cdot 4\text{H}_2\text{O}$, Sigma-Aldrich, 99%), tetra-*n*-butylammonium perchlorate (TBAClO_4 , Aldrich, $\geq 99.0\%$), sodium perchlorate (NaClO_4 , Sigma-Aldrich 99%), and lithium perchlorate (LiClO_4 , Sigma-Aldrich 99.99%) and were used to make the 0.1 M perchlorate acetonitrile (Burdick & Jackson, spectrophotometric grade) electrolyte solutions (abbreviated Mg^{2+} , Ca^{2+} , TBA^+ , Na^+ , and Li^+ , respectively). Transparent ZrO_2 or anatase TiO_2 nanocrystallites were prepared by acid hydrolysis of zirconium (IV) isopropoxide or titanium (IV) isopropoxide (Sigma-Aldrich, 97%), respectively, using a sol-gel method previously reported.¹⁴¹ Using a conductive transparent fluorine-doped SnO_2 -coated glass (FTO; Hartford Glass Co., Inc., 2.3 mm thick), the sols were cast by the doctor blade technique using transparent cellophane tape as a mask and spacer. The $\sim 4 \mu\text{m}$ thick films were sintered at 450 °C for 30 minutes under O_2 atmosphere and stored immediately afterwards in a 70 °C oven for later use. The $[\text{Ru}(\text{dtb})_2(\text{dcb})](\text{PF}_6)_2$ (dtb = 4,4'-di-*tert*-butyl-2,2'-bipyridine, and dcb = 4,4'-dicarboxylic acid-2,2'-bipyridine) and $[\text{Ru}(\text{btfmb})_2(\text{dcb})](\text{PF}_6)_2$ (btfmb = 4,4'-

bis(trifluoromethyl)-2,2'-bipyridine), **Scheme 7.1**, were available from previous studies.^{64,148,192}

Scheme 7.1: Ruthenium polypyridyl compounds used in this study.



Preparations. Sensitization was achieved by immersing the thin films overnight in a 1:1 acetonitrile:*t*-butanol solution containing ~1 mM of the Ru sensitizers. The films were sensitized to roughly maximum surface coverage, $\Gamma \sim 4 \times 10^{-8} \text{ mol/cm}^2$, which was determined by using a modified Beer-Lambert law.⁸⁶ The sensitized films were then immersed in neat acetonitrile 30 minutes before experimentation.

Spectroscopy. The sensitized thin films were positioned at a 45° angle in the 1 cm quartz cuvette for all measurements. Steady-state UV-visible absorption spectra were obtained on a Varian Cary 50 at room temperature. The corrected steady-state photoluminescence (PL) spectra were obtained with a Horiba Fluorolog-3 spectrophotometer using a 532 nm solid-state laser (Coherent) at room temperature and detected with a Hamamatsu R2658 photomultiplier with 750 nm blazed gratings. For the transient absorption (TA) measurements and spectroelectrochemical measurements, the solutions containing the sensitized thin films were purged with argon gas (Airgas, >99.998%) for 30 minutes.

Transient Absorption and Time-Resolved Photoluminescence. The transient absorption (TA) and time-resolved PL measurements were obtained with a 532 nm Q-switched, pulsed Nd:YAG laser (Quintel U.S.A. (BigSky) Brilliant B; ~6 ns full width at half maximum, 1 Hz) with a diameter of ~1 cm and the power at 10 mW.¹⁶⁸ A 150 W xenon arc lamp pulsed with 70 V served as the probe beam, which was aligned 90° to the laser excitation light. Single wavelength detection was achieved with a monochromator (Spex 1702/04) optically coupled to an R928 photomultiplier tube (Hamamatsu). Two glass filters <390 nm were positioned between the sample and the probe lamp to eliminate any possible direct excitation of the TiO₂, and a 532 nm notch filter was between the sample and detector to remove laser scatter. The transient data was acquired with a computer-interfaced digital oscilloscope (LeCroy 9450, Dual 350 MHz) with an overall instrument response time of ~20 ns. An average of 30 laser shots were collected at each probe wavelength. Time-resolved PL was achieved by collecting the scatter at 90° from the pulsed 532 nm excitation.

The steady-state and time-resolved PL at different applied potentials were achieved by using a potentiostat (Bioanalytical Scientific Instruments, Inc. (BAS) model CV-50W or EC Epsilon electrochemical analyzer) in a standard three-electrode arrangement with a sensitized TiO₂ thin film working electrode, a platinum gauze counter electrode, and an aqueous silver reference electrode. The reference electrode was calibrated using the ferrocenium/ferrocene half-wave potential that was measured before and after experiments in a 100 mM TBAClO₄/acetonitrile solution. All potentials reported here are reported versus the normal hydrogen electrode (NHE) by using the conversion constant -630 mV from NHE to ferrocenium/ferrocene in acetonitrile at 25 °C.²⁰⁴ A new sensitized TiO₂ slide was used for the different electrolyte solutions.

Electrochemistry. Spectroelectrochemical and cyclic voltammetry (CV) experiments were performed using a sensitized TiO₂ film as the working electrode in a three-electrode arrangement, as described above. Cyclic voltammetry gave quantitatively different values for $E^{\circ}(\text{Ru}^{\text{III/II}})$ ($\Delta E = 100 \text{ mV}$ vs NHE) when compared to the spectroelectrochemical. In the spectroelectrochemical experiments, the film absorption was monitored after the application of increasingly oxidative electrochemical biases. The resulting spectra reported on the relative concentrations of the Ru^{2+} and Ru^{3+} present under a given bias. The EO value could then be extracted using spectral modeling techniques. Non-Nernstian behavior was seen, and was accounted for with a non-ideality factor in accordance with previous reports.¹⁵⁴ The $E^{\circ}(\text{Ru}^{\text{III/II}})$ values for $\text{Ru}(\text{dtb})_2(\text{dcb})/\text{TiO}_2$ were previously reported using spectroelectrochemistry, so all CVs acquired were taken concurrently with $\text{Ru}(\text{dtb})_2(\text{dcb})/\text{TiO}_2$ in the various salt acetonitrile solutions. The differences in the $E^{\circ}(\text{Ru}^{\text{III/II}})$ values from CV compared to the literature values were used to adjust the $E^{\circ}(\text{Ru}^{\text{III/II}})$ values from CV for $\text{Ru}(\text{btfmb})_2(\text{dcb})/\text{TiO}_2$. This correction method is largely due to the extremely slow oxidation rate of $\text{Ru}(\text{btfmb})_2(\text{dcb})/\text{TiO}_2$.

The Gibbs free energy stored in the MLCT excited state (ΔG_{ES}) was determined by a tangent line extrapolated back to zero on the high energy side of the PL spectra in all the various perchlorate solutions.^{76,205} The excited-state reduction potentials $E^{\circ}(\text{Ru}^{\text{III/II}*})$ and $E^{\circ}(\text{Ru}^{\text{II*}/+})$ were then calculated by using **Equations 7.1** and **7.2**.

$$E^{\circ}(\text{Ru}^{\text{III/II}*}) = E^{\circ}(\text{Ru}^{\text{III/II}}) - \Delta G_{\text{ES}} \quad (7.1)$$

$$E^{\circ}(\text{Ru}^{\text{II*}/+}) = E^{\circ} + \Delta G_{\text{ES}} \quad (7.2)$$

The ligand reduction potentials ($E^0(\text{Ru}^{\text{II}/+})$) were determined from spectroelectrochemical measurements of $\text{Ru}(\text{btfmb})_2(\text{dcb})/\text{TiO}_2$ and $\text{Ru}(\text{dtb})_2(\text{dcb})/\text{ZrO}_2$.^{205,206}

Analysis. Global analysis of the time-resolved PL data was performed using Igor Pro 5.05 and minimization was accomplished using the Levenberg-Marquardt iteration algorithm.

7.3 Results

Figure 7.1 shows the metal-to-ligand charge-transfer (MLCT) absorption and photoluminescence (PL) spectra of $[\text{Ru}(\text{dtb})_2(\text{dcb})]^{2+}$ and $[\text{Ru}(\text{btfmb})_2(\text{dcb})]^{2+}$ anchored to mesoporous TiO_2 thin films, abbreviated $\text{Ru}(\text{dtb})_2(\text{dcb})/\text{TiO}_2$ and $\text{Ru}(\text{btfmb})_2(\text{dcb})/\text{TiO}_2$. The spectra were sensitive to the presence of Na^+ , Li^+ , Ca^{2+} , Mg^{2+} or tetrabutyl ammonium (TBA^+) perchlorate salts present at 0.1 M concentrations in the acetonitrile solution. The spectral difference between the neat and cation contained electrolytes, ΔA_{sd} , are seen **Figure 7.2C and 7.2D**.

The addition of cations induced a bathochromic shift in the MLCT feature for $\text{Ru}(\text{dtb})_2(\text{dcb})/\text{TiO}_2$, as seen in **Figure 7.1C**. In contrast, a hypsochromic shift is seen for $\text{Ru}(\text{btfmb})_2(\text{dcb})/\text{TiO}_2$. The bathochromic shift has been observe previously for $\text{Ru}(\text{dtb})_2(\text{dcb})/\text{TiO}_2$, and was attributed to a change in the local electric field at the interface after cation adsorption.⁷⁶ The interaction between the electric field change and the molecular dipole moment likely induces this shift. The hypsochromic shift seen for $\text{Ru}(\text{btfmb})_2(\text{dcb})/\text{TiO}_2$ is likely the same effect, since the dipole moment of the complex is anti-parallel with respect to $\text{Ru}(\text{dtb})_2(\text{dcb})/\text{TiO}_2$

Excitation into the MLCT absorption band of $\text{Ru}(\text{dtb})_2(\text{dcb})/\text{TiO}_2$ in acetonitrile resulted in room temperature PL. The spectra underwent a bathochromic shift after the addition of the

various perchlorate salts. The PL intensity also decreased with Na^+ , Li^+ , Ca^{2+} , or Mg^{2+} addition.⁷⁶ Room temperature PL observed after excitation of $\text{Ru}(\text{btfmb})_2(\text{dcb})/\text{TiO}_2$ underwent a hypsochromic shift after the addition of Na^+ or Li^+ perchlorate salts accompanied by a slight *increase* in the PL intensity. The addition of Ca^{2+} or Mg^{2+} perchlorate salts to the acetonitrile solution that surrounded a $\text{Ru}(\text{btfmb})_2(\text{dcb})/\text{TiO}_2$ thin films also induced a blue shift in the PL spectra with an $\sim 50\%$ decrease in PL intensity.

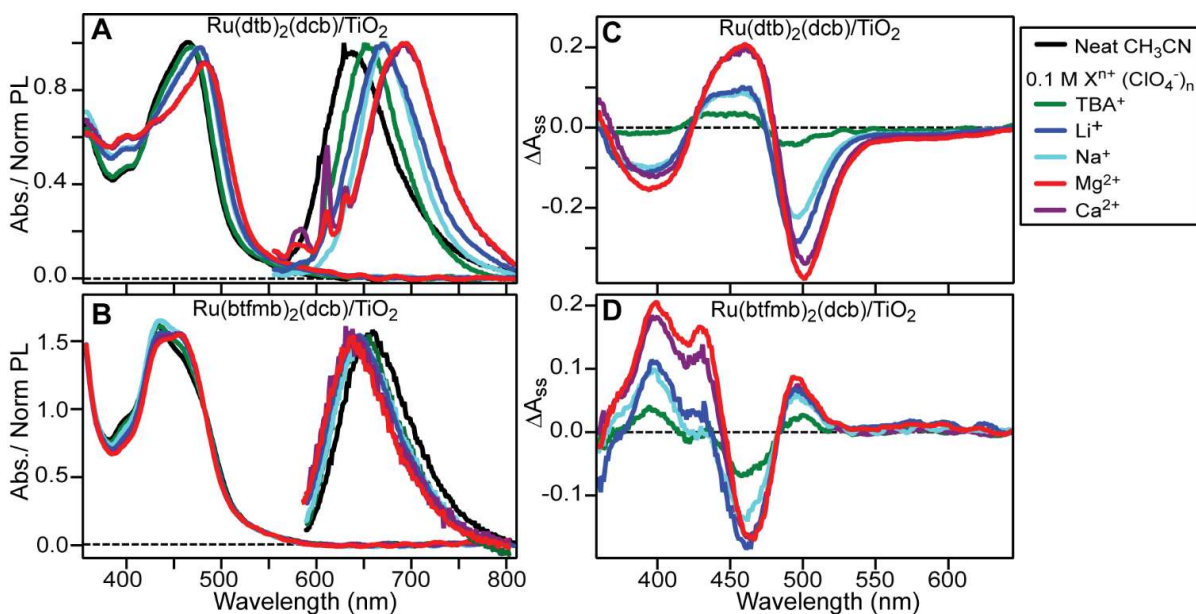


Figure 7.1: Steady-state absorption and normalized photoluminescence (PL) spectra of **A)** $\text{Ru}(\text{dtb})_2(\text{dcb})/\text{TiO}_2$ and **B)** $\text{Ru}(\text{btfmb})_2(\text{dcb})/\text{TiO}_2$ in neat acetonitrile and in the presence of 0.1 M perchlorate acetonitrile solutions. Steady-state difference absorption spectra (ΔA_{ss}) of **C)** $\text{Ru}(\text{dtb})_2(\text{dcb})/\text{TiO}_2$ and **D)** $\text{Ru}(\text{btfmb})_2(\text{dcb})/\text{TiO}_2$ in the indicated perchlorate acetonitrile solutions.

Application of negative electrochemical potential to a sensitized TiO_2 thin film in a standard three-electrode electrochemical cell resulted in the reduction of the TiO_2 nanocrystallites to yield $\text{TiO}_2(\text{e}^-)$ s. A broad absorption was seen across the visible, and has previously been assigned to $\text{TiO}_2(\text{e}^-)$.⁷⁶ **Figures 7.2A** and **7.2B** show the PL spectra of $\text{Ru}(\text{dtb})_2(\text{dcb})/\text{TiO}_2$ and $\text{Ru}(\text{btfmb})_2(\text{dcb})/\text{TiO}_2$ in 0.1 M LiClO_4 at selected applied potentials. As the applied potential was made more negative the PL intensity of $\text{Ru}(\text{dtb})_2(\text{dcb})/\text{TiO}_2$ first

increased, reached a plateau and then decreased. The PL spectra shifted toward the blue as the potential was decreased. Under the same conditions for Ru(btmb)₂(dcb)/TiO₂ only a decrease in the PL intensity was observed as the applied potential was made more negative.

Table 7.1: Photophysical and Electrochemical Properties of Ru(dtb)₂(dcb)/TiO₂ and Ru(btmb)₂(dcb)/TiO₂ in 0.1 M Cation Perchlorate Acetonitrile Solutions

Sensitizer	Cation	ΔG_{ES} (eV) ^a	$E^\circ(\text{Ru}^{\text{III/II}})^b$	$E^\circ(\text{Ru}^{\text{II/+}})^{b,c}$	$E^\circ(\text{Ru}^{\text{III/II}})_{b,c}$	$E^\circ(\text{Ru}^{2+*/+})^{b,c}$
Ru(dtb) ₂ (dcb) /TiO ₂	Na ⁺	2.00	1.43		-0.57	0.86
	Li ⁺	2.08	1.46	-0.99 ^d	-0.62	0.84
	Mg ²⁺	1.99	1.49		-0.50	0.99
	Ca ²⁺	2.01	1.50		-0.51	0.99
Ru(btmb) ₂ (dcb) /TiO ₂	Na ⁺	2.11	1.86		-0.25	1.5
	Li ⁺	2.13	1.83	-0.67	-0.30	1.3
	Mg ²⁺	2.15	1.91		-0.25	1.4
	Ca ²⁺	2.17	1.85		-0.32	1.3

^aThe free energy stored in the excited state. ^bAll reduction potentials are reported in V vs. NHE.

^cThe excited state reduction potential calculated using equations 1 and 2 in the text. ^dThe reduction potential was estimated from spectroelectrochemical data performed on ZrO₂, providing a value consistent with Wolfbauer et al.²⁰⁷

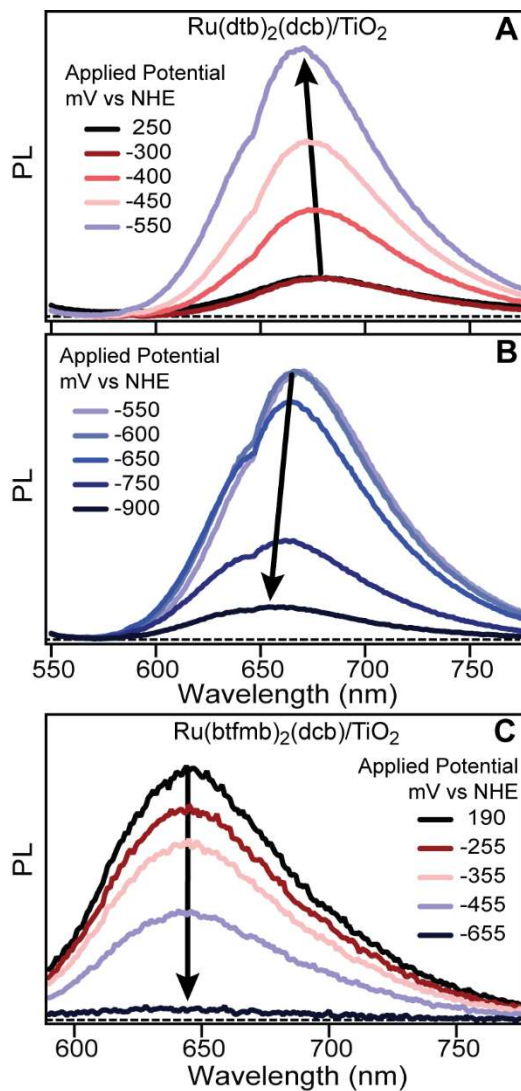


Figure 7.2: Steady-state PL spectra of **A)** and **B)** $\text{Ru(dtb)}_2(\text{dcb})/\text{TiO}_2$ and **C)** $\text{Ru(btmb)}_2(\text{dcb})/\text{TiO}_2$ in 0.1 M LiClO_4 acetonitrile at the indicated applied potentials.

Figures 7.3A and **7.3B** show the PL intensity maximum wavelength with respect to the applied potential for $\text{Ru(dtb)}_2(\text{dcb})/\text{TiO}_2$ and $\text{Ru(btmb)}_2(\text{dcb})/\text{TiO}_2$ where the dashed lines **7.3B** correspond to the PL maximum measured in neat CH_3CN . For both materials, a negative applied potential caused the PL spectra to shift towards the values measured in neat acetonitrile. **Figures 7.3C** and **7.3D** plot the PL maximum intensity at each applied potential

divided by the PL intensity at the most positive applied potential. This PL ratio reached a cation dependent maximum. For

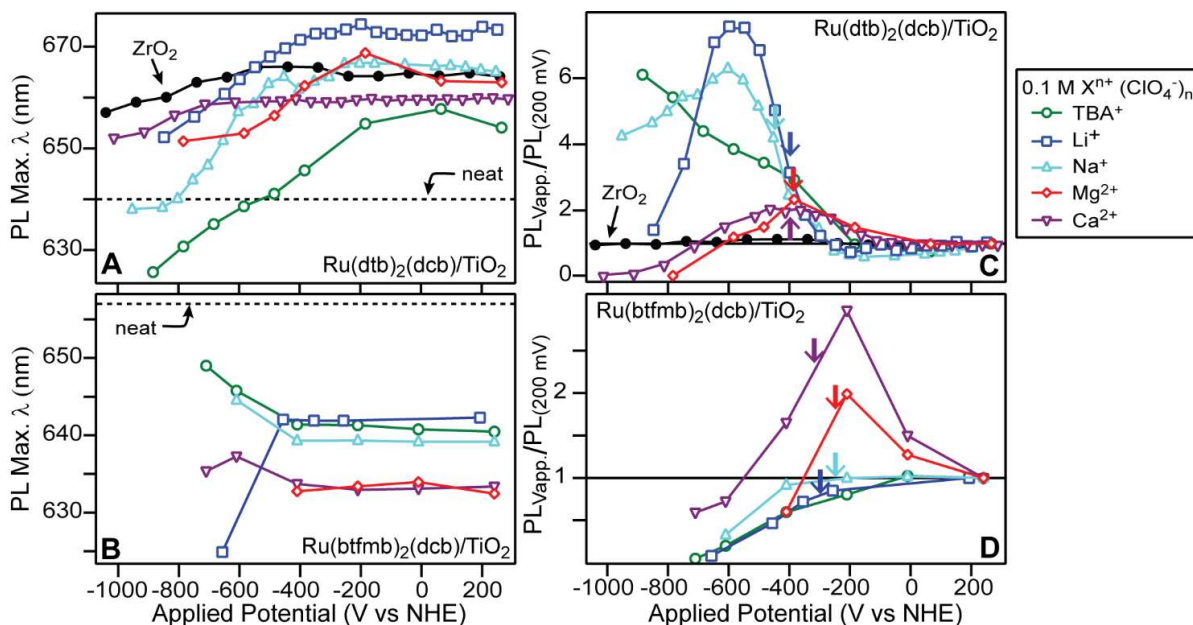


Figure 7.3: The PL intensity maximum wavelength of **A)** Ru(dtb)₂(dcb)/TiO₂ and **B)** Ru(btfmtb)₂(dcb)/TiO₂ measured in the five 0.1 M cation perchlorate acetonitrile solutions as a function of applied potential. The dotted line is PL center wavelength measured for Ru(dtb)₂(dcb)/TiO₂ and Ru(btfmtb)₂(dcb)/TiO₂ in neat acetonitrile. The relative PL intensities of **C)** Ru(dtb)₂(dcb)/TiO₂ and **D)** Ru(btfmtb)₂(dcb)/TiO₂ in 0.1 M cation perchlorate acetonitrile solutions at various applied potentials. The PL intensities of the >200 mV bands were normalized to one and the corresponding, more negative potential PL bands, were scaled relative to the >200 mV band. The black circles in A and C are from [Ru(dtb)₂(dcb)]²⁺ anchored to ZrO₂ in Li⁺ solution.

Ru(dtb)₂(dcb)/TiO₂, monovalent cations displayed a maximum intensity at more negative potentials than that measured for divalent cations. A PL intensity increase did not occur for Ru(btfmtb)₂(dcb)/TiO₂ in the monovalent salt solutions, but did in Mg²⁺ and Ca²⁺ salt solutions. The applied potential necessary to achieve the maximum PL intensity for Ru(btfmtb)₂(dcb)/TiO₂ in Mg²⁺ or Ca²⁺ was more positive than that required for Ru(dtb)₂(dcb)/TiO₂ in the same electrolytes. Interestingly, under all conditions studied, the PL maximum remained permanently shifted after application of a negative potential even though the PL intensity returned to the initial value when the potential was stepped back. Absorption

measurements before and after showed no measurable desorption of the surface bound sensitizers. Control experiments with $[\text{Ru}(\text{dtb})_2(\text{dcb})]^{2+}$ anchored to ZrO_2 , showed only a very small change in the PL intensity or maximum wavelength with applied bias.

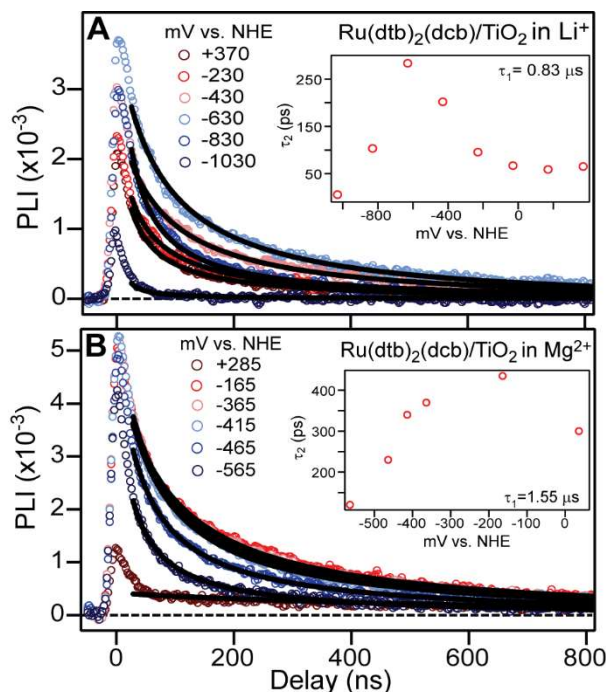


Figure 7.4: Representative time-resolved PL of $\text{Ru}(\text{dtb})_2(\text{dcb})/\text{TiO}_2$ in **A)** Li^+ and **B)** Mg^{2+} acetonitrile solutions at the indicated applied potentials. The black lines are from fitting with equation 2 where the first-order rate constant was held constant and $\tau_2 = 1/k_2$ was determined through global fits of the time-resolved data. The insets show τ_2 at each applied potential.

Figures 7.4A and 7.4B show time-resolved PL decays monitored at 710 nm or 700 nm after pulsed 532 nm laser excitation of $\text{Ru}(\text{dtb})_2(\text{dcb})/\text{TiO}_2$ in Li^+ and Mg^{2+} acetonitrile solutions at the indicated applied potentials. In Li^+ electrolytes, the initial amplitudes of the PL decays first increased and then decreased as the applied potential was made more negative. The largest PL amplitude was measured at -630 mV in Li^+ electrolyte, and at -415 mV for Mg^{2+} electrolyte. Time-resolved measurements in the other cation perchlorate solutions were

also performed, and for all five cation solutions, the initial PL amplitudes reached a maximum value at approximately the same potential as was observed in the steady-state PL experiments.

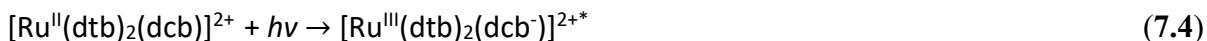
Excited state relaxation was sensitive to the applied potential. The PL decays were non-exponential, although a bi-exponential kinetic model fit the data well. At intermediate applied potentials, a parallel first- and second-order kinetic model described the data well, **Equation 3.**²⁰⁰

$$PL(t) = \frac{I_0 k_1 e^{-k_1 t}}{k_1 + k_2 I_0 - k_2 I_0 e^{-k_1 t}} \quad (7.3)$$

Here I_0 is the initial PL amplitude, k_1 is the first-order rate constant, and k_2 is the *observed* second-order rate constant. The best k_2 value was abstracted from the kinetic data while holding k_1 constant at each applied potential. The time constant $\tau_2 = 1/k_2$ first increased and then decreased with more negative applied potentials, Figure 4 insets.

7.4 Discussion

The thermally equilibrated excited states for Ru polypyridyl compounds studied here resided on the most easily reduced ligand. For $[Ru(dtb)_2(dcb)]^{2+}$ the excited state was localized on the dcb ligand with the carboxylic acid groups used for surface binding, while in $[Ru(btmb)_2(dcb)]^{2+}$ the excited state was localized on a remote trifluoro-methyl substituted bipyridine, **Equations 7.4 and 7.5.**¹⁴⁸ The excited state dipole moments of these compounds are therefore expected to be antiparallel.





The spectroscopic data reported herein indicates that the same excited state dipole orientation was maintained after anchoring to the TiO₂ nanocrystallites. Indeed, the spectra of the two compounds shifted in opposite directions when the surface electric field was intentionally changed. Such behavior has previously been reported for organic dye molecules, but to our knowledge this represents the first example for transition metal compounds.

The magnitude of the electric fields at these sensitized TiO₂ interfaces was controlled with an applied potential and/or with the introduction of specific cations into the external acetonitrile electrolyte that surrounds the sensitized thin film. There exists compelling evidence that Lewis acidic alkali and alkaline earth cations adsorb to the TiO₂ surface from acetonitrile solutions used in dye-sensitized solar cells.^{107,208–212} All the cations studied here induced a dramatic quenching of the PL intensity for Ru(dtb)₂(dcb)/TiO₂, and while only some of the cations caused a similar effect for Ru(btfmb)₂(dcb)/TiO₂ (see below). Transient absorption measurements have previously shown that the decrease in PL intensity was accompanied by enhanced excited state injection.¹⁰⁸ For this reason, alkali and alkaline earth cations are often referred to as “potential determining ions” for non-aqueous TiO₂ interfaces.^{66,106,108,164} Large organic cations, like tetra-butyl ammonium (TBA⁺), have a much smaller influence on excited state injection yields and hence are not considered to be potential determining.⁶⁶ The addition of alkali or alkaline earth cations resulted in a significant red shift in the absorption and PL spectra of Ru(dtb)₂(dcb)/TiO₂, and a blue shift in the absorption and PL spectra of Ru(btfmb)₂(dcb)/TiO₂.

Application of a sufficient negative electrochemical potential resulted in reduction of the TiO₂. The electrons in the substrate caused a shift in the PL spectra for Ru(dtb)₂(dcb)/TiO₂ and Ru(btmb)₂(dcb)/TiO₂. The shifts trended opposite energetic directions, consistent with reversed orientation of $\Delta\vec{\mu}$ for the two sensitizers relative to the surface field.

In all cases, the spectral shifts observed with electron injection or cation adsorption were unidirectional, giving rise to a first-derivative shape when subtracted from the initial spectrum, defined herein as ΔA_{sd} . Computational results and x-ray diffraction studies of titanium alkoxide materials indicate that the cations are associated with the vacant oxygen sites at the surface,^{210,213} while there exists very little evidence for anion adsorption to TiO₂ from organic solvents. There is a substantial and compelling literature that indicates that the as-prepared sol-gel processed TiO₂ is negatively charged,¹⁶⁴ thus, the origin of the spectral shift has been attributed to cation “screening” of the surface electric field generated by anionic oxide site(s), which will be explained below.

Cation adsorption to the surface will reduce the field experienced by the sensitizers, behavior sometimes termed “shielding” or more commonly called “screening”.^{64,59,68,81,152,214} The electric field in each TiO₂ nanocrystallite is expected to be normal to the surface,^{64,68} so the change in the transition dipole moment, $\Delta\vec{\mu}$, of the sensitizer will determine whether the excited state will be stabilized or destabilized with the addition of cations. For Ru(dtb)₂(dcb)/TiO₂, which has an anti-parallel $\Delta\vec{\mu}$ with respect to the TiO₂ electric field, the adsorbed cations “screened” the surface electric field and the sensitizers were stabilized (a red shift in absorption and PL spectrum was observed).^{64,68} Interestingly, for Ru(btmb)₂(dcb)/TiO₂, the absorption and PL spectra shifted to the blue compared to the neat spectrum, and the first derivative spectrum (ΔA_{sd}) had the opposite sign as Ru(dtb)₂(dcb)/TiO₂,

implying that the surface electric field was *parallel* to the sensitizer's $\Delta\vec{\mu}$. Hence, “screening” of the field by the surface adsorbed cations destabilized the energetics of Ru(btmb)₂(dcb)/TiO₂.

The influence of the PL intensity on the applied potential was also of fundamental interest as it reports on excited state relaxation processes that occur at these electrified interfaces. Interestingly the PL intensity first increases and then decreases as the quasi-Fermi level of the oxide materials were raised toward the vacuum level, i.e. forward bias. The PL enhancements in dye-sensitized materials has previously been observed and rationalized by surface desorption. The PL quenching has not been previously reported in sensitized TiO₂ literature. Below we discuss the applicability of these observations in the context of the relevant literature.

PL Enhancements: Band-Filling Model

As mentioned in the Introduction Section, the observed PL intensity increase with an applied forward bias was first reported by O'Regan, and has been studied by several groups since.^{62,102,193,215–217} In the present study, this PL increase cannot be attributed to dye desorption. Instead a band-filling model is proposed wherein the excited state injection yield decreases as the “acceptor states” in TiO₂ are filled with the applied potential. These acceptor states are thought to have an exponential energy dependence and can be filled to different levels with an applied potential.⁷⁶

The small PL intensity enhancement from Ru(btmb)₂(dcb)⁺/TiO₂ with a forward bias is likely due lower MLCT excited state energy, which limited injection prior to the application of an electrochemical bias. For Li⁺, Na⁺, and TBA⁺ containing electrolytes, there was no

measurable PL intensity enhancement from Ru(btmb)₂(dcb)*-TiO₂ and no evidence of efficient excited state injection. In contrast, with Ca²⁺ or Mg²⁺ containing electrolytes, a factor of three increase in PL intensity was observed with forward bias suggesting that excited state injection did indeed occur. It is known that the electrolytes Ca²⁺ and Mg²⁺ stabilize the TiO₂ acceptor states more substantially than do the monovalent cations, so it is reasonable to believe that the acceptor states are only energetically favorable for electron injection from Ru(btmb)₂(dcb)*-TiO₂ when Ca²⁺ or Mg²⁺ are present in the solution.^{76,108}

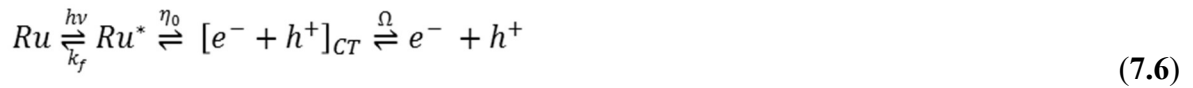
A new finding reported herein was that the PL intensity from both sensitizers anchored to TiO₂ decreased at more negative potentials, and the quenching mechanism was explored.

PL Decreases: Energy and/or Electron Transfer

The strong blue-black coloration that accompanies TiO₂ reduction could provide energy transfer pathways. It was shown previously that second-order behavior occurs with higher laser intensities, which creates a substantial amount of excited-state sensitizers.¹⁰⁸ It was proposed that this decrease was the result of a second-order mechanism triplet-triplet annihilation reaction. In the case presented in this paper, by reducing the competitive electron injection pathway (equation 3), there may be a buildup of excited state sensitizers that can undergo electron transfer quickly across the TiO₂ surface to annihilate another excited-state sensitizer. However, no significant change in quenching was observed when the surface concentration was lower from 7.5×10^{-8} mol/cm² to 1.0×10^{-8} mol/cm². Lowering the sensitizers concentration anchored at the surface (and therefore the number of excited state sensitizer) should have slowed the annihilation process.

Electric field-induced PL quenching with a field strength of $>10^6$ V/cm has been well documented for organic polymers and metal chelates for application in organic light-emitting diodes.^{218–222} Proposed mechanisms for the resulting PL quenching were exciton-exciton annihilation, exciton quenching by charge carriers, and field-assisted exciton-dissociation into an electron-hole pair. However, the lack of an excited-state concentration dependence on the PL decay in this present study (the results described above), triplet-triplet annihilation and triplet-charge carrier annihilation process are unlikely.

Field-induced exciton dissociation has been described using the Onsager theory of geminate recombination (**Equation 7.6**).²²⁰



After excitation to form the excited state, S^* , the system may relax back to the ground state with a rate k_f , or an electron will transfer to an acceptor molecule creating a charge-transfer (CT) state. The CT state may then dissociate into electrons and holes, forming the charge separated state. The initial separation probability η_0 to form the CT state was initial described as being field independent while the CT state dissociation is field-dependent with the probability Ω . The overall probability to separate is,

$$\eta(F) = \eta_0 \Omega(F) \quad (7.7)$$

and the luminescence can be model with,

$$L(F) = \frac{k_r}{k_r + k_n} [1 - \eta(F)] I_{ex} \quad (7.8)$$

I_{ex} is the radiant flux per unit area, k_r and k_n are the rate constants for the radiative and nonradiative decay, respectively.²²³ Several modifications to the Onsager theory have been introduced, including the model given by Braun to incorporate the electric field-dependent

lifetime of the CT state.^{224,225} Another modification is the macrotrap model where field-assisted charge hopping separation of localized excited states quenches the PL.^{223,226}

In the Onsager model, the competition between recombination to the ground state and dissociation of the CT state is dependent upon the magnitude of the Coulombic attraction felt by the CT state.²²⁷ The photogenerated electron-hole pairs are strongly bound by a Coulomb potential that forms excitons with some amount of binding energy. If the electric field becomes large enough to overcome the exciton binding energy, the excitons can dissociate because the electric field lowers the density of acceptor states, allowing for charge escape.^{218,228}

In the system studied here, the application of a negative applied bias to the TiO₂-sensitized thin film enhances the electric field, which is reported by the absorption shift of the sensitizer.^{64,76,81} It is therefore a possibility that when the electric field becomes as strong as the Coulomb potential, the density of acceptor states in TiO₂ are lowered allowing for rapid electron injection, and thus quenching the PL. **Figure 7.8** is the PL intensity as a function of the electric field felt by the sensitizers.⁷⁶ **Figure 7.8** suggests that the binding energy between the electrons and holes are weaker when in Na⁺ acetonitrile solution than in Ca²⁺, meaning that smaller magnitude of the electric field is required to overcome the Coulomb potential to separate the charges when Na⁺ electrolytes are present. THz measurements probing the intermediate interfacial charge transfer states in these four electrolyte acetonitrile solutions would be useful to support this hypothesis.²²⁸

Of course, fast charge recombination is also playing a role in the PL quenching.^{58,111,131,132} The build-up of electrons in the TiO₂ acceptor states is thought to increase the driving force for charge recombination, and thus faster charge recombination at more negative potentials.²¹⁷ The TA data shows that the intensity of oxidized dye produced reduces as the potential

becomes more negative. Most likely charge recombination is on the ps time scale at large negative potentials and cannot be probed on our TA system.²²⁹

7.5 Conclusion

In conclusion, this chapter sought understand how the application of a forward electrochemical bias to a sensitized nanocrystalline TiO₂ thin film would influence the photophysical properties. A key difference in the molecule studied here is the orientation of them molecular dipole moment, which are either normal (Ru(dtb)₂(dcb)^{*}/TiO₂) or anormal (Ru(btmb)₂(dcb)^{*}/TiO₂) to the surface. The addition of Lewis acidic cation caused a shift in the MLCT absorption of the film, which either shifted to higher or lower energies dependent on the dipole moment alignment, with the magnitude of the shift being dependent on the cation identity. Application of an increasingly negative bias saw an initial growth in PL for Ru(dtb)₂(dcb)^{*}/TiO₂ for all cations studied, while a similar effect for Ru(btmb)₂(dcb)^{*}/TiO₂ was only seen in Mg²⁺ or Ca²⁺. This was likely due to the filling of electron accepting states, which prevented injection by the sensitizer and lead to more radiative processes. The PL was eventually observed to decrease at sufficiently negative biases. Though speculative, it is possible that electric fields may induce causes a diminished PL at the interface. However, this study demonstrates that the orientation of molecular dipoles at the interface can significantly alter their interactions with the substrates, cations and electric fields present during functional device operation.

REFERENCES

- (1) International Energy Agency. *Key World Energy Statistics*; 2016.
- (2) Peterson, C. H.; Rice, S. D.; Short, J. W.; Esler, D.; Bodkin, J. L.; Ballachey, B. E.; Irons, D. B. Long-Term Ecosystem Response to the Exxon Valdez Oil Spill. *Science*, **2003**, *302* (5653), 2082–2086.
- (3) Beyer, J.; Trannum, H. C.; Bakke, T.; Hodson, P. V.; Collier, T. K. Environmental Effects of the Deepwater Horizon Oil Spill: A Review. *Mar. Pollut. Bull.* **2016**, *110* (1), 28–51.
- (4) International Energy Agency, *CO₂ Emissions from Fuel Combustion*; 2016.
- (5) Kampa, M.; Castanas, E. Human Health Effects of Air Pollution. *Environ. Pollut.* **2008**, *151* (2), 362–367.
- (6) Dresselhaus, M. S.; Thomas, I. L. Alternative Energy Technologies. *Nature* **2001**, *414* (6861), 332–337.
- (7) Mackenzie, F. T. *Our Changing Planet*, 4th ed.; Folchetti, N., Ed.; Pearson: Upper Saddle River, New Jersey, 2011.
- (8) Sawyer, J. S. Man-Made Carbon Dioxide and the “Greenhouse” Effect. *Nature* **1972**, *239* (5366), 23–26.
- (9) Petit, J. R.; Jouzel, J.; Raynaud, D.; Barkov, N. I.; Barnola, J.-M.; Basile, I.; Bender, M.; Chappellaz, J.; Davis, M.; Delaygue, G.; Delmotte, M.; Kotlyakov, V. M.; Legrand, M.; Lipenkov, V. Y.; Lorius, C.; Pepin, L.; Ritz, C.; Saltzman, E.; Stievenard, M. Climate and atmospheric history of the past 420,000 years from the Vostok ice core, Antarctic, *Nature* **1999**, *399* (6735), 429–436.
- (10) Lüthi, D.; Le Floch, M.; Bereiter, B.; Blunier, T.; Barnola, J.-M.; Siegenthaler, U.; Raynaud, D.; Jouzel, J.; Fischer, H.; Kawamura, K.; Stocker, T. F. High-Resolution Carbon Dioxide Concentration Record 650,000-800,000 Years before Present. *Nature* **2008**, *453* (7193), 379–382.
- (11) Stips, A.; Macias, D.; Coughlan, C.; Garcia-Gorriz, E.; Liang, X. S.; Lüthi, D.; Le Floch, M.; Bereiter, B.; Blunier, T.; Barnola, J.-M.; Siegenthaler, U.; Raynaud, D.; Jouzel, J.; Fischer, H.; Kawamura, K.; Stocker, T. F. On the Causal Structure between CO₂ and Global Temperature. *Nature* **2008**, *453* (7193), 379–382.
- (12) Hansen, J.; Ruedy, R.; Sato, M.; Lo, K. Global Surface Temperature Change. *Rev. Geophys.* **2010**, *48* (4), RG4004.

- (13) Walther, G.; Post, E.; Convey, P.; Menzel, A.; Parmesan, C.; Beebee, T. J. C.; Fromentin, J.; Hoegh-Guldberg, O.; Bairlein, F. Ecological Responses to Recent Climate Change. *Nature* **2002**, *416* (6879), 389–395.
- (14) Carpenter, K. E.; Abrar, M.; Aeby, G.; Aronson, R. B.; Banks, S.; Bruckner, A.; Chiriboga, A.; Cortes, J.; Delbeek, J. C.; DeVantier, L.; Edgar, G. J.; Edwards, A. J.; Fenner, D.; Guzman, H. M.; Hoeksema, B. W.; Hodgson, G.; Johan, O.; Licuanan, W. Y.; Livingstone, S. R.; Lovell, E. R.; Moore, J. A.; Obura, D. O.; Ochavillo, D.; Polidoro, B. A.; Precht, W. F.; Quibilan, M. C.; Reboton, C.; Richards, Z. T.; Rogers, A. D.; Sanciangco, J.; Sheppard, A.; Sheppard, C.; Smith, J.; Stuart, S.; Turak, E.; Veron, J. E. N.; Wallace, C.; Weil, E.; Wood, E. One-Third of Reef-Building Corals Face Elevated Extinction Risk from Climate Change and Local Impacts. *Science* **2008**, *321* (5888), 560–563.
- (15) Thomas, C. D.; Cameron, A.; Green, R. E.; Bakkenes, M.; Beaumont, L. J.; Collingham, Y. C.; Erasmus, B. F. N.; de Siqueira, M. F.; Grainger, A.; Hannah, L.; Hughes, L.; Huntley, B.; van Jaarsveld, A. S.; Midgley, G. F.; Miles, L.; Ortega-Huerta, M. a; Townsend Peterson, A.; Phillips, O. L.; Williams, S. E. Extinction Risk from Climate Change. *Nature* **2004**, *427* (6970), 145–148.
- (16) National Oceanic and Atmospheric Administration, Trends in Atmospheric CO₂, <https://www.esrl.noaa.gov/gmd/ccgg/trends/full.html>, Accessed 01/01/2017
- (17) Hill, J.; Nelson, E.; Tilman, D.; Polasky, S.; Tiffany, D. Environmental, Economic, and Energetic Costs and Benefits of Biodiesel and Ethanol Biofuels. *Proc. Natl. Acad. Sci.* **2006**, *103* (30), 11206–11210.
- (18) Searchinger, T.; Heimlich, R.; Houghton, R. A.; Dong, F.; Elobeid, A.; Fabiosa, J.; Tokgoz, S.; Hayes, D.; Yu, T.-H. Use of U.S. Croplands for Biofuels Increases Greenhouse Gases Through Emissions from Land-Use Change. *Science* **2008**, *319* (5867), 1238–1240.
- (19) Dares, C. J.; Lapides, A. M.; Mincher, B. J.; Meyer, T. J. Electrochemical Oxidation of 243Am(III) in Nitric Acid by a Terpyridyl-Derivatized Electrode. *Science* **2015**, *350* (6261), 652–655.
- (20) Lewis, N. S.; Nocera, D. G. Powering the Planet: Chemical Challenges in Solar Energy Utilization. *Proc. Natl. Acad. Sci.* **2006**, *103* (43), 15729–15735.
- (21) Brennaman, M. K.; Dillon, R. J.; Alibabaei, L.; Gish, M. K.; Dares, C. J.; Ashford, D. L.; House, R. L.; Meyer, G. J.; Papanikolas, J. M.; Meyer, T. J. Finding the Way to Solar Fuels with Dye-Sensitized Photoelectrosynthesis Cells. *J. Am. Chem. Soc.* **2016**, *138* (40), 13085–13102.

- (22) Ashford, D. L.; Gish, M. K.; Vannucci, A. K.; Brennaman, M. K.; Templeton, J. L.; Papanikolas, J. M.; Meyer, T. J. Molecular Chromophore–Catalyst Assemblies for Solar Fuel Applications. *Chem. Rev.* **2015**, *115* (23), 13006–13049.
- (23) Swanson, R. M. A Vision for Crystalline Silicon Photovoltaics. *Prog. Photovoltaics Res. Appl.* **2006**, *14* (5), 443–453.
- (24) Goodrich, A. C.; Powell, D. M.; James, T. L.; Woodhouse, M.; Buonassisi, T. Assessing the Drivers of Regional Trends in Solar Photovoltaic Manufacturing. *Energy Environ. Sci.* **2013**, *6* (10), 2811.
- (25) Tiedje, T.; Yablonovitch, E.; Cody, G. D.; Brooks, B. G. Limiting Efficiency of Silicon Solar Cells. *IEEE Trans. Electron Devices* **1984**, *31* (5), 711–716.
- (26) Shockley, W.; Queisser, H. J. Detailed Balance Limit of Efficiency of P-N Junction Solar Cells. *J. Appl. Phys.* **1961**, *32* (3), 510–519.
- (27) Meyer, G. J. The 2010 Millennium Technology Grand Prize: Dye-Sensitized Solar Cells. *ACS Nano* **2010**, *4* (8), 4337–4343.
- (28) Nazeeruddin, M. K.; Zakeeruddin, S. M.; Humphry-Baker, R.; Jirousek, M.; Liska, P.; Vlachopoulos, N.; Shklover, V.; Fischer, C.-H.; Grätzel, M. Acid–Base Equilibria of (2,2′-Bipyridyl-4,4′-Dicarboxylic acid)ruthenium(II) Complexes and the Effect of Protonation on Charge-Transfer Sensitization of Nanocrystalline Titania. *Inorg. Chem.* **1999**, *38* (26), 6298–6305.
- (29) Namba, S.; Hishiki, Y. Color Sensitization of Zinc Oxide with Cyanine Dyes 1. *J. Phys. Chem.* **1965**, *69* (3), 774–779.
- (30) Grätzel, M. Dye-Sensitized Solar Cells. *J. Photochem. Photobiol. C Photochem. Rev.* **2003**, *4* (2), 145–153.
- (31) Anderson, S.; Constable, E. C.; Dare-Edwards, M. P.; Goodenough, J. B.; Hamnett, A.; Seddon, K. R.; Wright, R. D. Chemical Modification of a Titanium (IV) Oxide Electrode to Give Stable Dye Sensitisation without a Supersensitiser. *Nature* **1979**, *280* (5723), 571–573.
- (32) Jaeger, C. D.; Fan, F.-R. F.; Bard, A. J. Semiconductor Electrodes. 26. Spectral Sensitization of Semiconductors with Phthalocyanine. *J. Am. Chem. Soc.* **1980**, *102* (8), 2592–2598.
- (33) O'Regan, B.; Grätzel, M. A Low-Cost, High-Efficiency Solar Cell Based on Dye-Sensitized Colloidal TiO₂ Films. *Nature* **1991**, *353* (6346), 737–740.
- (34) Mathew, S.; Yella, A.; Gao, P.; Humphry-Baker, R.; Curchod, B. F. E.; Ashari-Astani, N.; Tavernelli, I.; Rothlisberger, U.; Nazeeruddin, M. K.; Grätzel, M. Dye-Sensitized

- Solar Cells with 13% Efficiency Achieved through the Molecular Engineering of Porphyrin Sensitizers. *Nat. Chem.* **2014**, 6 (3), 242–247.
- (35) Yella, A.; Lee, H.-W.; Tsao, H. N.; Yi, C.; Chandiran, A. K.; Nazeeruddin, M. K.; Diau, E. W.-G.; Yeh, C.-Y.; Zakeeruddin, S. M.; Grätzel, M. Porphyrin-Sensitized Solar Cells with Cobalt (II/III)-Based Redox Electrolyte Exceed 12 Percent Efficiency. *Science* **2011**, 334 (6056), 629–634.
- (36) Listorti, A.; O'Regan, B.; Durrant, J. R. Electron Transfer Dynamics in Dye-Sensitized Solar Cells. *Chem. Mater.* **2011**, 23 (15), 3381–3399.
- (37) Zigler, D. F.; Morseth, Z. A.; Wang, L.; Ashford, D. L.; Brennaman, M. K.; Grumstrup, E. M.; Brigham, E. C.; Gish, M. K.; Dillon, R. J.; Alibabaei, L.; Meyer, G. J.; Meyer, T. J.; Papanikolas, J. M. Disentangling the Physical Processes Responsible for the Kinetic Complexity in Interfacial Electron Transfer of Excited Ru(II) Polypyridyl Dyes on TiO₂. *J. Am. Chem. Soc.* **2016**, 138 (13), 4426–4438.
- (38) Ardo, S.; Meyer, G. J. Photodriven Heterogeneous Charge Transfer with Transition-Metal Compounds Anchored to TiO₂ Semiconductor Surfaces. *Chem. Soc. Rev.* **2009**, 38 (1), 115–164.
- (39) Rowley, J. G.; Farnum, B. H.; Ardo, S.; Meyer, G. J. Iodide Chemistry in Dye-Sensitized Solar Cells: Making and Breaking I–I Bonds for Solar Energy Conversion. *J. Phys. Chem. Lett.* **2010**, 1 (20), 3132–3140.
- (40) Feldt, S. M.; Gibson, E. a.; Gabrielsson, E.; Sun, L.; Boschloo, G.; Hagfeldt, A. Design of Organic Dyes and Cobalt Polypyridine Redox Mediators for High-Efficiency Dye-Sensitized Solar Cells. *J. Am. Chem. Soc.* **2010**, 132 (46), 16714–16724.
- (41) Freitag, M.; Giordano, F.; Yang, W.; Pazoki, M.; Hao, Y.; Zietz, B.; Grätzel, M.; Hagfeldt, A.; Boschloo, G. Copper Phenanthroline as a Fast and High-Performance Redox Mediator for Dye-Sensitized Solar Cells. *J. Phys. Chem. C* **2016**, 120 (18), 9595–9603.
- (42) Saygili, Y.; Söderberg, M.; Pellet, N.; Giordano, F.; Cao, Y.; Muñoz-García, A. B.; Zakeeruddin, S. M.; Vlachopoulos, N.; Pavone, M.; Boschloo, G.; Kavan, L.; Moser, J.-E.; Grätzel, M.; Hagfeldt, A.; Freitag, M. Copper Bipyridyl Redox Mediators for Dye-Sensitized Solar Cells with High Photovoltage. *J. Am. Chem. Soc.* **2016**, 138 (45), 15087–15096.
- (43) Yaghoobi Nia, N.; Farahani, P.; Sabzyan, H.; Zendejdel, M.; Oftadeh, M. A Combined Computational and Experimental Study of the [Co(bpy)₃]^{2+/3+} Complexes as One-Electron Outer-Sphere Redox Couples in Dye-Sensitized Solar Cell Electrolyte Media. *Phys. Chem. Chem. Phys.* **2014**, 16 (23), 11481.

- (44) Feldt, S. M.; Lohse, P. W.; Kessler, F.; Nazeeruddin, M. K.; Grätzel, M.; Boschloo, G.; Hagfeldt, A. Regeneration and Recombination Kinetics in Cobalt Polypyridine Based Dye-Sensitized Solar Cells, Explained Using Marcus Theory. *Phys. Chem. Chem. Phys.* **2013**, *15* (19), 7087.
- (45) Kashif, M. K.; Axelson, J. C.; Duffy, N. W.; Forsyth, C. M.; Chang, C. J.; Long, J. R.; Spiccia, L.; Bach, U. A New Direction in Dye-Sensitized Solar Cells Redox Mediator Development: In Situ Fine-Tuning of the cobalt(II)/(III) Redox Potential through Lewis Base Interactions. *J. Am. Chem. Soc.* **2012**, *134* (40), 16646–16653.
- (46) Mosconi, E.; Yum, J.-H.; Kessler, F.; Gómez García, C. J.; Zuccaccia, C.; Cinti, A.; Nazeeruddin, M. K.; Grätzel, M.; De Angelis, F. Cobalt Electrolyte/dye Interactions in Dye-Sensitized Solar Cells: A Combined Computational and Experimental Study. *J. Am. Chem. Soc.* **2012**, *134* (47), 19438–19453.
- (47) Hamann, T. W. The End of Iodide? Cobalt Complex Redox Shuttles in DSSCs. *Dalt. Trans.* **2012**, *41* (11), 3111.
- (48) Kim, H.-S.; Ko, S.-B.; Jang, I.-H.; Park, N.-G. Improvement of Mass Transport of the [Co(bpy)₃](II/III) Redox Couple by Controlling Nanostructure of TiO₂ Films in Dye-Sensitized Solar Cells. *Chem. Commun.* **2011**, *47* (47), 12637–12639.
- (49) Kakiage, K.; Aoyama, Y.; Yano, T.; Otsuka, T.; Kyomen, T.; Unno, M.; Hanaya, M. An Achievement of over 12 Percent Efficiency in an Organic Dye-Sensitized Solar Cell. *Chem. Commun.* **2014**, *50* (48), 6379–6381.
- (50) Sapp, S. A.; Elliott, C. M.; Contado, C.; Caramori, S.; Bignozzi, C. A. Substituted Polypyridine Complexes of Cobalt (II / III) as Efficient Electron-Transfer Mediators in Dye-Sensitized Solar Cells. *J. Am. Chem. Soc.* **2002**, *124*, 11215–11222.
- (51) Carli, S.; Busatto, E.; Caramori, S.; Boaretto, R.; Argazzi, R.; Timpson, C. J.; Bignozzi, C. A.; Isof, C. N. R.; Borsari, L. Comparative Evaluati, Ion of Catalytic Counter Electrodes for Co(III)/(II) Electron Shuttles in Regenerative Photoelectrochemical Cells, *J. Phys. Chem. C* **2013**, *117*, 5142.
- (52) Bessette, A.; Cibian, M.; Ferreira, J. G.; DiMarco, B. N.; Bélanger, F.; Désilets, D.; Meyer, G. J.; Hanan, G. S. Azadipyrromethene Cyclometalation in Neutral Ru II Complexes: Photosensitizers with Extended near-Infrared Absorption for Solar Energy Conversion Applications. *Dalt. Trans.* **2016**, *45* (26), 10563–10576.
- (53) Argazzi, R.; Bignozzi, C. A.; Heimer, T. A.; Castellano, F. N.; Meyer, G. J. Light-Induced Charge Separation across Ru(II)-Modified Nanocrystalline TiO₂ Interfaces with Phenothiazine Donors. *J. Phys. Chem. B* **1997**, *101* (14), 2591–2597.

- (54) Gillaizeau-Gauthier, I.; Odobel, F.; Alebbi, M.; Argazzi, R.; Costa, E.; Bignozzi, C. A.; Qu, P.; Meyer, G. J. Phosphonate-Based Bipyridine Dyes for Stable Photovoltaic Devices. *Inorg. Chem.* **2001**, *40* (23), 6073–6079.
- (55) Argazzi, R.; Bignozzi, C. A.; Heimer, T. A.; Castellano, F. N.; Meyer, G. J. Long-Lived Photoinduced Charge Separation across Nanocrystalline TiO₂ Interfaces. *J. Am. Chem. Soc.* **1995**, *117* (47), 11815–11816.
- (56) Brigham, E. C.; Meyer, G. J. Ostwald Isolation to Determine the Reaction Order for TiO₂(e⁻)|S⁺ → TiO₂|S Charge Recombination at Sensitized TiO₂ Interfaces. *J. Phys. Chem. C* **2014**, *118* (15), 7886–7893.
- (57) DeVries, M. J.; Pellin, M. J.; Hupp, J. T. Dye-Sensitized Solar Cells: Driving-Force Effects on Electron Recombination Dynamics with Cobalt-Based Shuttles. *Langmuir* **2010**, *26* (11), 9082–9087.
- (58) Haque, S. a; Tachibana, Y.; Willis, R. L.; Moser, J. E.; Grätzel, M.; Klug, D. R.; Durrant, J. R. Parameters Influencing Charge Recombination Kinetics in Dye-Sensitized Nanocrystalline Titanium Dioxide Films. *J. Phys. Chem. B* **2000**, *104* (3), 538–547.
- (59) Sampaio, R. N.; O'Donnell, R. M.; Barr, T. J.; Meyer, G. J. Electric Fields Control TiO₂(e⁻) + I₃⁻ → Charge Recombination in Dye-Sensitized Solar Cells. *J. Phys. Chem. Lett.* **2014**, *5*, 3265–3268.
- (60) Nelson, J.; Haque, S. A.; Klug, D. R.; Durrant, J. R. Trap-Limited Recombination in Dye-Sensitized Nanocrystalline Metal Oxide Electrodes. *Phys. Rev. B* **2001**, *63* (20), 205321.
- (61) Bauer, C.; Boschloo, G.; Mukhtar, E.; Hagfeldt, A. Electron Injection and Recombination in Ru(dcbpy)₂(NCS)₂ Sensitized Nanostructured ZnO. *J. Phys. Chem. B* **2001**, *105* (24), 5585–5588.
- (62) Zaban, A.; Ferrere, S.; Gregg, B. a. Relative Energetics at the Semiconductor/Sensitizing Dye/Electrolyte Interface. *J. Phys. Chem. B* **1998**, *102* (2), 452–460.
- (63) Olson, C. L. Influence of Cation on Charge Recombination in Dye-Sensitized TiO₂ Electrodes. *J. Phys. Chem. B* **2006**, *110* (19), 9619–9626.
- (64) Ardo, S.; Sun, Y.; Staniszewski, A.; Castellano, F. N.; Meyer, G. J. Stark Effects after Excited-State Interfacial Electron Transfer at Sensitized TiO₂ Nanocrystallites. *J. Am. Chem. Soc.* **2010**, *132* (19), 6696–6709.

- (65) Cappel, U. B.; Feldt, S. M.; Schöneboom, J.; Hagfeldt, A.; Boschloo, G. The Influence of Local Electric Fields on Photoinduced Absorption in Dye-Sensitized Solar Cells. *J. Am. Chem. Soc.* **2010**, *132* (26), 9096–9101.
- (66) Redmond, C.; Fitzmaurice, D.; Section, E. Spectroscopic Determination of Flatband Potentials. **1993**, 1426–1430.
- (67) Enright, B.; Redmond, G.; Fitzmaurice, D. Spectroscopic Determination of Flatband Potentials for Polycrystalline TiO₂ Electrodes in Mixed Solvent Systems. *J. Phys. Chem.* **1994**, *98* (24), 6195–6200.
- (68) Ardo, S.; Sun, Y.; Castellano, F. N.; Meyer, G. J. Excited-State Electron Transfer from Ruthenium-Polypyridyl Compounds to Anatase TiO₂ Nanocrystallites: Evidence for a Stark Effect *J. Phys. Chem. B* **2010**, *114* (45), 14596–14604.
- (69) Oh, D. H.; Boxer, S. G. Stark Effect Spectra of Ru(diimine)₃²⁺ Complexes. *J. Am. Chem. Soc.* **1989**, *111* (3), 1130–1131.
- (70) Vance, F. W.; Hupp, J. T. Probing the Symmetry of the Nonlinear Optic Chromophore Ru(trans-4,4'-Diethylaminostyryl-2,2'-bipyridine)₃²⁺: Insight from Polarized Hyper-Rayleigh Scattering and Electroabsorption (Stark) Spectroscopy. *J. Am. Chem. Soc.* **1999**, *121*, 4047–4053.
- (71) Fried, S. D.; Boxer, S. G. Measuring Electric Fields and Noncovalent Interactions Using the Vibrational Stark Effect. *Acc. Chem. Res.* **2015**, *48* (4), 998–1006.
- (72) Boxer, S. G. Stark Realities. *J. Phys. Chem. B* **2009**, *113* (10), 2972–2983.
- (73) Burdziński, G.; Karolczak, J.; Ziólek, M. Dynamics of Local Stark Effect Observed for a Complete D149 Dye-Sensitized Solar Cell. *Phys. Chem. Chem. Phys.* **2013**, *15* (11), 3889.
- (74) Sampaio, R. N.; Li, G.; Meyer, G. J. Continuous Surface Electric Field Contraction Accompanying Electron Transfer from TiO₂ to Oxidized Sensitizers. *ACS Energy Lett.* **2016**, *1* (4), 846–851.
- (75) Adamo, C.; Jacquemin, D. The Calculations of Excited-State Properties with Time-Dependent Density Functional Theory. *Chem. Soc. Rev.* **2013**, *42* (3), 845–856.
- (76) O'Donnell, R. M.; Sampaio, R. N.; Barr, T. J.; Meyer, G. J. Electric Fields and Charge Screening in Dye Sensitized Mesoporous Nanocrystalline TiO₂ Thin Films. *J. Phys. Chem. C* **2014**, *118* (30), 16976–16986.
- (77) Pastore, M.; De Angelis, F. Computational Modeling of Stark Effects in Organic Dye-Sensitized TiO₂ Heterointerfaces. *J. Phys. Chem. Lett.* **2011**, *2* (11), 1261–1267.

- (78) Ohta, N.; Awasthi, K.; Okoshi, K.; Manseki, K.; Miura, H.; Inoue, Y.; Nakamura, K.; Kono, H.; Diau, E. W.-G. Stark Spectroscopy of Absorption and Emission of Indoline Sensitizers: A Correlation with the Performance of Photovoltaic Cells. *J. Phys. Chem. C* **2016**, acs.jpcc.6b08531.
- (79) Roiati, V.; Mosconi, E.; Listorti, A.; Colella, S.; Gigli, G.; De Angelis, F. Stark Effect in Perovskite/TiO₂-Sensitized Solar Cells: Evidence of Local Interfacial Order. *Nano Lett.* **2014**, 14 (4), 2168–2174.
- (80) Vaissier, V.; Mosconi, E.; Moia, D.; Pastore, M.; Frost, J. M.; De Angelis, F.; Barnes, P. R. F.; Nelson, J. Effect of Molecular Fluctuations on Hole Diffusion within Dye Monolayers. *Chem. Mater.* **2014**, 26 (16), 4731–4740.
- (81) O'Donnell, R. M.; Ardo, S.; Meyer, G. J. Charge-Screening Kinetics at Sensitized TiO₂ Interfaces. *J. Phys. Chem. Lett.* **2013**, 4 (17), 2817–2821.
- (82) Saavedra Becerril, V.; Franchi, D.; Abrahamsson, M. Ionic Liquid-Induced Local Charge Compensation: Effects on Back Electron-Transfer Rates in Dye-Sensitized TiO₂ Thin Films. *J. Phys. Chem. C* **2016**, 120 (36), 20016–20023.
- (83) Bonhôte, P.; Gogniat, E.; Tingry, S.; Barbé, C.; Vlachopoulos, N.; Lenzmann, F.; Comte, P.; Grätzel, M. Efficient Lateral Electron Transport inside a Monolayer of Aromatic Amines Anchored on Nanocrystalline Metal Oxide Films. *J. Phys. Chem. B* **1998**, 102 (9), 1498–1507.
- (84) Blauch, D. N.; Saveant, J. M. Dynamics of Electron Hopping in Assemblies of Redox Centers. Percolation and Diffusion. *J. Am. Chem. Soc.* **1992**, 114 (9), 3323–3332.
- (85) Blauch, D. N.; Saveant, J. M. Effects of Long-Range Electron Transfer on Charge Transport in Static Assemblies of Redox Centers. *J. Phys. Chem.* **1993**, 97 (24), 6444–6448.
- (86) Trammell, S. A.; Meyer, T. J. Diffusional Mediation of Surface Electron Transfer on TiO₂. *J. Phys. Chem. B* **1999**, 103 (1), 104–107.
- (87) Wang, Q.; Zakeeruddin, S. M.; Cremer, J.; Bäuerle, P.; Humphry-Baker, R.; Grätzel, M. Cross Surface Ambipolar Charge Percolation in Molecular Triads on Mesoscopic Oxide Films. *J. Am. Chem. Soc.* **2005**, 127 (15), 5706–5713.
- (88) Ardo, S.; Meyer, G. J. Direct Observation of Photodriven Intermolecular Hole Transfer across TiO₂ Nanocrystallites: Lateral Self-Exchange Reactions and Catalyst Oxidation. *J. Am. Chem. Soc.* **2010**, 132 (27), 9283–9285.
- (89) Hu, K.; Robson, K. C. D.; Johansson, P. G.; Berlinguette, C. P.; Meyer, G. J. Intramolecular Hole Transfer at Sensitized TiO₂ Interfaces. *J. Am. Chem. Soc.* **2012**, 134 (20), 8352–8355.

- (90) Hu, K.; Robson, K. C. D.; Beauvilliers, E. E.; Schott, E.; Zarate, X.; Arratia-Perez, R.; Berlinguette, C. P.; Meyer, G. J. Intramolecular and Lateral Intermolecular Hole Transfer at the Sensitized TiO₂ Interface. *J. Am. Chem. Soc.* **2014**, *136* (3), 1034–1046.
- (91) Manke, F.; Frost, J. M.; Vaissier, V. V.; Nelson, J.; Barnes, P. R. F. Influence of a Nearby Substrate on the Reorganization Energy of Hole Exchange between Dye Molecules. *Phys. Chem. Chem. Phys.* **2015**, *17* (11), 7345–7354.
- (92) Moia, D.; Vaissier, V.; López-Duarte, I.; Torres, T.; Nazeeruddin, M. K.; O'Regan, B. C.; Nelson, J.; Barnes, P. R. F. The Reorganization Energy of Intermolecular Hole Hopping between Dyes Anchored to Surfaces. *Chem. Sci.* **2014**, *5* (1), 281–290.
- (93) Moia, D.; Cappel, U. B.; Leijtens, T.; Li, X.; Telford, A. M.; Snaith, H. J.; O'Regan, B. C.; Nelson, J.; Barnes, P. R. F. The Role of Hole Transport between Dyes in Solid-State Dye-Sensitized Solar Cells. *J. Phys. Chem. C* **2015**, *119* (33), 18975–18985.
- (94) Moia, D.; Szumska, A.; Vaissier, V.; Planells, M.; Robertson, N.; O'Regan, B. C.; Nelson, J.; Barnes, P. R. F. Interdye Hole Transport Accelerates Recombination in Dye Sensitized Mesoporous Films. *J. Am. Chem. Soc.* **2016**, *138* (40), 13197–13206.
- (95) DiMarco, B. N.; Motley, T. C.; Balok, R. S.; Li, G.; Siegler, M. A.; O'Donnell, R. M.; Hu, K.; Meyer, G. J. A Distance Dependence to Lateral Self-Exchange across Nanocrystalline TiO₂: A Comparative Study of Three Homologous Ru III/II Polypyridyl Compounds. *J. Phys. Chem. C* **2016**, *120* (26), 14226–14235.
- (96) Wang, Q.; Zakeeruddin, S. M.; Nazeeruddin, M. K.; Humphry-Baker, R.; Grätzel, M. Molecular Wiring of Nanocrystals: NCS-Enhanced Cross-Surface Charge Transfer in Self-Assembled Ru-Complex Monolayer on Mesoscopic Oxide Films. *J. Am. Chem. Soc.* **2006**, *128* (13), 4446–4452.
- (97) Brennan, B. J.; Regan, K. P.; Durrell, A. C.; Schmittenmaer, C. A.; Brudvig, G. W. Solvent Dependence of Lateral Charge Transfer in a Porphyrin Monolayer *ACS Energy Lett.* **2016**, *2*, 168–173.
- (98) Ardo, S.; Meyer, G. J. Characterization of Photoinduced Self-Exchange Reactions at Molecule–Semiconductor Interfaces by Transient Polarization Spectroscopy: Lateral Intermolecular Energy and Hole Transfer across Sensitized TiO₂ Thin Films. *J. Am. Chem. Soc.* **2011**, *133* (39), 15384–15396.
- (99) Moia, D.; Leijtens, T.; Noel, N.; Snaith, H. J.; Nelson, J.; Barnes, P. R. F. Dye Monolayers Used as the Hole Transporting Medium in Dye-Sensitized Solar Cells. *Adv. Mater.* **2015**, *27* (39), 5889–5894.
- (100) Barr, T. J.; Sampaio, R. N.; DiMarco, B. N.; James, E. M.; Meyer, G. J. Phantom Electrons and Cation Effects in SnO₂ Thin Films. *Submitted*.

- (101) Barzykin, A. V.; Tachiya, M. Mechanism of Charge Recombination in Dye-Sensitized Nanocrystalline Semiconductors: Random Flight Model. *J. Phys. Chem. B* **2002**, *106* (17), 4356–4363.
- (102) Knorr, F. J.; McHale, J. L. Spectroelectrochemical Photoluminescence of Trap States of Nanocrystalline TiO₂ in Aqueous Media. *J. Phys. Chem. C* **2013**, *117* (26), 13654–13662.
- (103) Mercado, C. C.; Knorr, F. J.; McHale, J. L.; Usmani, S. M.; Ichimura, A. S.; Saraf, L. V. Location of Hole and Electron Traps on Nanocrystalline Anatase TiO₂. *J. Phys. Chem. C* **2012**, *116* (19), 10796–10804.
- (104) Ansari-Rad, M.; Abdi, Y.; Arzi, E. Reaction Order and Ideality Factor in Dye-Sensitized Nanocrystalline Solar Cells: A Theoretical Investigation. *J. Phys. Chem. C* **2012**, *116* (20), 10867–10872.
- (105) Knauf, R. R.; Brennaman, M. K.; Alibabaei, L.; Norris, M. R.; Dempsey, J. L. Revealing the Relationship between Semiconductor Electronic Structure and Electron Transfer Dynamics at Metal Oxide–Chromophore Interfaces. *J. Phys. Chem. C* **2013**, *117* (48), 25259–25268.
- (106) Redmond, G.; Fitzmaurice, D. Spectroscopic Determination of Flatband Potentials for Polycrystalline Titania Electrodes in Nonaqueous Solvents. *J. Phys. Chem.* **1993**, *97*, 1426–1430.
- (107) Wang, H.; Peter, L. M. Influence of Electrolyte Cations on Electron Transport and Electron Transfer in Dye-Sensitized Solar Cells. *J. Phys. Chem. C* **2012**, *116* (19), 10468–10475.
- (108) Kelly, C. A.; Farzad, F.; Thompson, D. W.; Stipkala, J. M.; Meyer, G. J. Cation-Controlled Interfacial Charge Injection in Sensitized Nanocrystalline TiO₂. *Langmuir* **1999**, *15* (20), 7047–7054.
- (109) Nelson, J.; Chandler, R. E. Random Walk Models of Charge Transfer and Transport in Dye Sensitized Systems. *Coord. Chem. Rev.* **2004**, *248* (13–14), 1181–1194.
- (110) Katoh, R.; Furube, A.; Barzykin, A. V.; Arakawa, H.; Tachiya, M. Kinetics and Mechanism of Electron Injection and Charge Recombination in Dye-Sensitized Nanocrystalline Semiconductors. *Coord. Chem. Rev.* **2004**, *248* (13–14), 1195–1213.
- (111) Tachibana, Y.; Haque, S. a; Mercer, I. P.; Durrant, J. R.; Klug, D. R. Electron Injection and Recombination in Dye Sensitized Nanocrystalline Titanium Dioxide Films: A Comparison of Ruthenium Bipyridyl and Porphyrin Sensitizer Dyes. *J. Phys. Chem. B* **2000**, *104* (6), 1198–1205.

- (112) Bisquert, J.; Vikhrenko, V. S. Interpretation of the Time Constants Measured by Kinetic Techniques in Nanostructured Semiconductor Electrodes and Dye-Sensitized Solar Cells. *J. Phys. Chem. B* **2004**, *108*, 2313.
- (113) Bisquert, J.; Zaban, A.; Salvador, P. Analysis of the Mechanisms of Electron Recombination in Nanoporous TiO₂ Dye-Sensitized Solar Cells. Nonequilibrium Steady-State Statistics and Interfacial Electron Transfer via Surface States. *J. Phys. Chem. B* **2002**, *106* (34), 8774–8782.
- (114) Bauer, C.; Boschloo, G.; Mukhtar, E.; Hagfeldt, A. Interfacial Electron-Transfer Dynamics in Ru(tcterpy)(NCS) 3 -Sensitized TiO₂ Nanocrystalline Solar Cells. *J. Phys. Chem. B* **2002**, *106* (49), 12693–12704.
- (115) Gish, M. K.; Lapides, A. M.; Brennaman, M. K.; Templeton, J. L.; Meyer, T. J.; Papanikolas, J. M. Ultrafast Recombination Dynamics in Dye-Sensitized SnO₂ /TiO₂ Core/Shell Films. *J. Phys. Chem. Lett.* **2016**, *7* (24), 5297–5301.
- (116) Rowley, J. G.; Ardo, S.; Sun, Y.; Castellano, F. N.; Meyer, G. J. Charge Recombination to Oxidized Iodide in Dye-Sensitized Solar Cells. **2011**, 20316–20325.
- (117) Robson, K. C. D.; Hu, K.; Meyer, G. J.; Berlinguette, C. P. Atomic Level Resolution of Dye Regeneration in the Dye Sensitized Solar Cell. *J. Am. Chem. Soc.* **2013**, 1961–1971.
- (118) Hu, K.; Blair, A. D.; Piechota, E. J.; Schauer, P. A.; Sampaio, R. N.; Parlane, F. G. L.; Meyer, G. J.; Berlinguette, C. P. Kinetic Pathway for Interfacial Electron Transfer from a Semiconductor to a Molecule. *Nat. Chem.* **2016**, *8* (9), 853–859.
- (119) Achey, D.; Ardo, S.; Xia, H.-L.; Siegler, M. A.; Meyer, G. J. Sensitization of TiO₂ by the MLCT Excited State of Co^I Coordination Compounds. *J. Phys. Chem. Lett.* **2011**, *2* (4), 305–308.
- (120) Hagfeldt, A.; Boschloo, G.; Sun, L.; Kloo, L.; Pettersson, H. Dye-Sensitized Solar Cells. *Chem. Rev.* **2010**, *110* (11), 6595–6663.
- (121) Yan, S.J.; Prieskorn, J.S.; Kim, Y.; Hupp, J.T. In Search of the Inverted Region: Chromophore-Based Driving Force Dependence of Interfacial Electron Transfer Reactivity at the Nanocrystalline Titanium Dioxide Semiconductor/solution Interface. *J. Phys. Chem. B* **2000**, *104* (46), 10877.
- (122) Dang, X.; Hupp, J. T. Interfacial Charge-Transfer Pathways: Evidence for Marcus-Type Inverted Electron Transfer in Metal Oxide Semiconductor/inorganic Dye Systems. *J. Am. Chem. Soc.* **1999**, *121* (36), 8399–8400.
- (123) Kuciauskas, D.; Freund, M. S.; Gray, H. B.; Winkler, J. R.; Lewis, N. S. Electron Transfer Dynamics in Nanocrystalline Titanium Dioxide Solar Cells Sensitized with

- Ruthenium or Osmium Polypyridyl Complexes. *J. Phys. Chem. B* **2001**, *105* (2), 392–403.
- (124) Hasselmann, G. M.; Meyer, G. J. Diffusion-Limited Interfacial Electron Transfer with Large Apparent Driving Forces. *J. Phys. Chem. B* **1999**, *103* (36), 7671–7675.
 - (125) Ansari-Rad, M.; Abdi, Y.; Arzi, E. Monte Carlo Random Walk Simulation of Electron Transport in Dye-Sensitized Nanocrystalline Solar Cells: Influence of Morphology and Trap Distribution. *J. Phys. Chem. C* **2012**, *116* (5), 3212–3218.
 - (126) Ansari-Rad, M.; Anta, J. A.; Bisquert, J. Interpretation of Diffusion and Recombination in Nanostructured and Energy-Disordered Materials by Stochastic Quasiequilibrium Simulation. *J. Phys. Chem. C* **2013**, *117* (32), 16275–16289.
 - (127) Knauf, R. R.; Kalanyan, B.; Parsons, G. N.; Dempsey, J. L. Charge Recombination Dynamics in Sensitized SnO₂ /TiO₂ Core/Shell Photoanodes. *J. Phys. Chem. C* **2015**, *119* (51), 28353–28360.
 - (128) Achey, D.; Brigham, E. C.; DiMarco, B. N.; Meyer, G. J. Excited State Electron Transfer after Visible Light Absorption by the Co(I) State of Vitamin B₁₂. *Chem. Commun.* **2014**, *50* (87), 13304–13306.
 - (129) Cid, J.-J.; García-Iglesias, M.; Yum, J.-H.; Forneli, A.; Albero, J.; Martínez-Ferrero, E.; Vázquez, P.; Grätzel, M.; Nazeeruddin, M. K.; Palomares, E.; Torres, T. Structure-Function Relationships in Unsymmetrical Zinc Phthalocyanines for Dye-Sensitized Solar Cells. *Chem. - A Eur. J.* **2009**, *15* (20), 5130–5137.
 - (130) Green, A. N. M.; Palomares, E.; Haque, S. A.; Kroon, J. M.; Durrant, J. R. Charge Transport versus Recombination in Dye-Sensitized Solar Cells Employing Nanocrystalline TiO₂ and SnO₂ Films. *J. Phys. Chem. B* **2005**, *109* (25), 12525–12533.
 - (131) Haque, S. A.; Palomares, E.; Cho, B. M.; Green, A. N. M.; Hirata, N.; Klug, D. R.; Durrant, J. R. Charge Separation versus Recombination in Dye-Sensitized Nanocrystalline Solar Cells: The Minimization of Kinetic Redundancy. *J. Am. Chem. Soc.* **2005**, *127* (10), 3456–3462.
 - (132) Haque, S. A.; Tachibana, Y.; Klug, D. R.; Durrant, J. R. Charge Recombination Kinetics in Dye-Sensitized Nanocrystalline Titanium Dioxide Films under Externally Applied Bias. *J. Phys. Chem. B* **1998**, *102* (10), 1745–1749.
 - (133) Regan, B. C. O.; Durrant, J. R. Kinetic and Energetic Paradigms for Dye- Sensitized Solar Cells : Moving from the Ideal to the Real. *Acc. Chem. Res.*, **2009**, *42* (11).
 - (134) Farnum, B. H.; Morseth, Z. A.; Brennaman, M. K.; Papanikolas, J. M.; Meyer, T. J. Driving Force Dependent, Photoinduced Electron Transfer at Degenerately Doped,

- Optically Transparent Semiconductor Nanoparticle Interfaces. *J. Am. Chem. Soc.* **2014**, *136* (45), 15869–15872.
- (135) Hamann, T. W.; Farha, O. K.; Hupp, J. T. Outer-Sphere Redox Couples as Shuttles in Dye-Sensitized Solar Cells. Performance Enhancement Based on Photoelectrode Modification via Atomic Layer Deposition. *J. Phys. Chem. C* **2008**, *112* (49), 19756–19764.
 - (136) Prasittichai, C.; Hupp, J. T. Surface Modification of SnO₂ Photoelectrodes in Dye-Sensitized Solar Cells: Significant Improvements in Photovoltage via Al₂O₃ Atomic Layer Deposition. *J. Phys. Chem. Lett.* **2010**, *1* (10), 1611–1615.
 - (137) Klahr, B. M.; Hamann, T. W. Performance Enhancement and Limitations of Cobalt Bipyridyl Redox Shuttles in Dye-Sensitized Solar Cells. *J. Phys. Chem. C* **2009**, *113* (31), 14040–14045.
 - (138) Johansson, P. G.; Kopecky, A.; Galoppini, E.; Meyer, G. J. Distance Dependent Electron Transfer at TiO₂ Interfaces Sensitized with Phenylene Ethynylene Bridged Ru^{II}-Isothiocyanate Compounds. *J. Am. Chem. Soc.* **2013**, *135*, 8331–8341.
 - (139) Bonhôte, P.; Moser, J.-E.; Humphry-Baker, R.; Vlachopoulos, N.; Zakeeruddin, S. M.; Walder, L.; Grätzel, M. Long-Lived Photoinduced Charge Separation and Redox-Type Photochromism on Mesoporous Oxide Films Sensitized by Molecular Dyads. *J. Am. Chem. Soc.* **1999**, *121* (6), 1324–1336.
 - (140) Johansson, P. G.; Zhang, Y.; Abrahamsson, M.; Meyer, G. J.; Galoppini, E. Slow Excited State Injection and Charge Recombination at Star-Shaped Ruthenium Polypyridyl compounds—TiO₂ Interfaces. *Chem. Commun.* **2011**, *47* (22), 6410.
 - (141) Heimer, T. A.; D’Arcangelis, S. T.; Farzad, F.; Stipkala, J. M.; Meyer, G. J. An Acetylacetonate-Based Semiconductor–Sensitizer Linkage. *Inorg. Chem.* **1996**, *35* (18), 5319–5324.
 - (142) Hu, K.; Meyer, G. J. Lateral Intermolecular Self-Exchange Reactions for Hole and Energy Transport on Mesoporous Metal Oxide Thin Films. *Langmuir* **2015**, *31* (41), 11164–11178.
 - (143) Hanson, K.; Brennaman, M. K.; Ito, A.; Luo, H.; Song, W.; Parker, K. A.; Ghosh, R.; Norris, M. R.; Glasson, C. R. K.; Concepcion, J. J.; Lopez, R.; Meyer, T. J. Structure–Property Relationships in Phosphonate-Derivatized, Ru II Polypyridyl Dyes on Metal Oxide Surfaces in an Aqueous Environment. *J. Phys. Chem. C* **2012**, *116* (28), 14837–14847.
 - (144) Penner, R. M.; Gogotsi, Y. The Rising and Receding Fortunes of Electrochemists. *ACS Nano* **2016**, *10* (4), 3875–3876.

- (145) Sutin, N. Nuclear, Electronic, and Frequency Factors in Electron Transfer Reactions. *Acc. Chem. Res.* **1982**, *15* (9), 275–282.
- (146) Barbara, P. F.; Meyer, T. J.; Ratner, M. a. Contemporary Issues in Electron Transfer Research. *J. Phys. Chem.* **1996**, *100* (31), 13148–13168.
- (147) Swords, W. B.; Li, G.; Meyer, G. J. Iodide Ion Pairing with Highly Charged Ruthenium Polypyridyl Cations in CH₃CN. *Inorg. Chem.* **2015**, *54* (9), 4512–4519.
- (148) O'Donnell, R. M.; Sampaio, R. N.; Li, G.; Johansson, P. G.; Ward, C. L.; Meyer, G. J. Photoacidic and Photobasic Behavior of Transition Metal Compounds with Carboxylic Acid Group(s). *J. Am. Chem. Soc.* **2016**, *138* (11), 3891–3903.
- (149) Bard, A. J.; Faulkner, L. R. *Electrochemical Methods: Fundamentals and Applications*, 2nd ed.; Wiley: New York, NY, 2001.
- (150) Daum, P.; Lenhard, J. R.; Rolison, D.; Murray, R. W. Diffusional Charge Transport through Ultrathin Films of Radiofrequency Plasma Polymerized Vinylferrocene at Low Temperature. *J. Am. Chem. Soc.* **1980**, *102* (14), 4649–4653.
- (151) Marton, A.; Clark, C. C.; Srinivasan, R.; Freundlich, R. E.; Narducci Sarjeant, A. A.; Meyer, G. J. Static and Dynamic Quenching of Ru(II) Polypyridyl Excited States by Iodide. *Inorg. Chem.* **2006**, *45* (1), 362–369.
- (152) DiMarco, B. N.; O'Donnell, R. M.; Meyer, G. J. Cation-Dependent Charge Recombination to Organic Mediators in Dye-Sensitized Solar Cells. *J. Phys. Chem. C* **2015**, *119* (37), 21599–21604.
- (153) Ward, C. L.; O'Donnell, R. M.; DiMarco, B. N.; Meyer, G. J. Kinetic Resolution of Charge Recombination and Electric Fields at the Sensitized TiO₂ Interface. *J. Phys. Chem. C* **2015**, *119* (45), 25273–25281.
- (154) Ardo, S.; Achey, D.; Morris, A. J.; Abrahamsson, M.; Meyer, G. J. Non-Nernstian Two-Electron Transfer Photocatalysis at Metalloporphyrin–TiO₂ Interfaces. *J. Am. Chem. Soc.* **2011**, *133* (41), 16572–16580.
- (155) Li, X.; Nazeeruddin, M. K.; Thelakkat, M.; Barnes, P. R. F.; Vilar, R.; Durrant, J. R. Spectroelectrochemical Studies of Hole Percolation on Functionalised Nanocrystalline TiO₂ Films: A Comparison of Two Different Ruthenium Complexes. *Phys. Chem. Chem. Phys.* **2011**, *13* (4), 1575–1584.
- (156) Chan, M.-S.; Wahl, A. C. Rate of Electron Exchange between Iron, Ruthenium, and Osmium Complexes Containing 1,10-Phenanthroline, 2,2'-bipyridyl, or Their Derivatives from Nuclear Magnetic Resonance Studies. *J. Phys. Chem.* **1978**, *82* (24), 2542–2549.

- (157) Swierk, J. R.; McCool, N. S.; Saunders, T. P.; Barber, G. D.; Mallouk, T. E. Effects of Electron Trapping and Protonation on the Efficiency of Water-Splitting Dye-Sensitized Solar Cells. *J. Am. Chem. Soc.* **2014**, *136* (31), 10974–10982.
- (158) Brown, G. M.; Sutin, N. A Comparison of the Rates of Electron Exchange Reactions of Ammine Complexes of ruthenium(II) and -(III) with the Predictions of Adiabatic, Outer-Sphere Electron Transfer Models. *J. Am. Chem. Soc.* **1979**, *101* (4), 883–892.
- (159) Biner, M.; Buerger, H. B.; Ludi, A.; Roehr, C. Crystal and Molecular Structures of [Ru(bpy)₃](PF₆)₃ and [Ru(bpy)₃](PF₆)₂ at 105 K. *J. Am. Chem. Soc.* **1992**, *114* (13), 5197–5203.
- (160) Grätzel, M. Solar Energy Conversion by Dye-Sensitized Photovoltaic Cells. *Inorg. Chem.* **2005**, *44* (20), 6841–6851.
- (161) Liu, Y.; Hagfeldt, A.; Xiao, X.-R.; Lindquist, S.-E. Investigation of Influence of Redox Species on the Interfacial Energetics of a Dye-Sensitized Nanoporous TiO₂ Solar Cell. *Sol. Energy Mater. Sol. Cells* **1998**, *55* (3), 267–281.
- (162) Wu, J.; Lan, Z.; Lin, J.; Huang, M.; Huang, Y.; Fan, L.; Luo, G. Electrolytes in Dye-Sensitized Solar Cells. *Chem. Rev.* **2015**, *115* (5), 2136–2173.
- (163) Staniszewski, A.; Ardo, S.; Sun, Y.; Castellano, F. N.; Meyer, G. J. Slow Cation Transfer Follows Sensitizer Regeneration at Anatase TiO₂ Interfaces. *J. Am. Chem. Soc.* **2008**, *130*, 11586–11587.
- (164) Pelet, S.; Moser, J.-E.; Gratzel, M. Cooperative Effect of Adsorbed Cations and Iodide on the Interception of Back Electron Transfer in the Dye Sensitization of Nanocrystalline TiO₂. *J. Phys. Chem. B* **2000**, *104* (8), 1795.
- (165) Kopidakis, N.; Schiff, E. a.; Park, N.-G.; van de Lagemaat, J.; Frank, a. J. Ambipolar Diffusion of Photocarriers in Electrolyte-Filled, Nanoporous TiO₂. *J. Phys. Chem. B* **2000**, *104* (16), 3930–3936.
- (166) Kambe, S.; Nakade, S.; Kitamura, T.; Wada, Y.; Yanagida, S. Influence of the Electrolytes on Electron Transport in Mesoporous TiO₂ –Electrolyte Systems. *J. Phys. Chem. B* **2002**, *106* (11), 2967–2972.
- (167) Bosch, E.; Kochi, J. K. Catalytic Oxidation of Chlorpromazine and Related Phenothiazines. Cation Radicals as the Reactive Intermediates in Sulfoxide Formation. *J. Chem. Soc. Perkin Trans. I* **1995**, No. 8, 1057.
- (168) Argazzi, R.; Bignozzi, C. a.; Heimer, T. A.; Castellano, F. N.; Meyer, G. J. Enhanced Spectral Sensitivity from Ruthenium(II) Polypyridyl Based Photovoltaic Devices. *Inorg. Chem.* **1994**, *33* (c), 5741–5749.

- (169) Shan, B.; Schmehl, R. Photochemical Generation of Strong One-Electron Reductants via Light-Induced Electron Transfer with Reversible Donors Followed by Cross Reaction with Sacrificial Donors. *J. Phys. Chem. A* **2014**, *118* (45), 10400–10406.
- (170) O'Donnell, R. M.; Johansson, P. G.; Abrahamsson, M.; Meyer, G. J. Excited-State Relaxation of Ruthenium Polypyridyl Compounds Relevant to Dye-Sensitized Solar Cells. *Inorg. Chem.* **2013**, *52* (12), 6839–6848.
- (171) Barnes, P. R. F.; Miettunen, K.; Li, X.; Anderson, A. Y.; Bessho, T.; Gratzel, M.; O'Regan, B. C. Interpretation of Optoelectronic Transient and Charge Extraction Measurements in Dye-Sensitized Solar Cells. *Adv. Mater.* **2013**, *25* (13), 1881–1922.
- (172) Lewis, N. S. Progress in Understanding Electron-Transfer Reactions at Semiconductor/Liquid Interfaces. *J. Phys. Chem. B* **1998**, *102* (25), 4843–4855.
- (173) Plater, M. J.; Jackson, T. Polyaromatic Amines. Part 3: Synthesis of Poly(diarylamino)styrenes and Related Compounds. *Tetrahedron* **2003**, *59* (25), 4673–4685.
- (174) Park, S. M.; Bard, A. J. Electrogenenerated Chemiluminescence. XXII. Generation of Exciplexes in the Radical Ion Reaction. *J. Am. Chem. Soc.* **1975**, *97* (11), 2978–2985.
- (175) Ansari-Rad, M. Dye Regeneration Kinetics in Dye-Sensitized Solar Cell: Long-Range Charge-Transfer Effects. *J. Phys. Chem. C* **2016**, *120* (16), 9000–9006.
- (176) Barzykin, a. V.; Tachiya, M. Mechanism of Molecular Control of Recombination Dynamics in Dye-Sensitized Nanocrystalline Semiconductor Films. *J. Phys. Chem. B* **2004**, *108* (24), 8385–8389.
- (177) Swierk, J. R.; McCool, N. S.; Nemes, C. T.; Mallouk, T. E.; Schmittenmaer, C. A. Ultrafast Electron Injection Dynamics of Photoanodes for Water-Splitting Dye-Sensitized Photoelectrochemical Cells. *J. Phys. Chem. C* **2016**, *120* (11), 5940–5948.
- (178) Pazoki, M.; Hagfeldt, A.; Boschloo, G. Stark Effects in D35-Sensitized Mesoporous TiO₂: Influence of Dye Coverage and Electrolyte Composition. *Electrochim. Acta* **2015**, *179*, 174–178.
- (179) Govind Rao, V.; Dhital, B.; Lu, H. P. Probing Driving Force and Electron Accepting State Density Dependent Interfacial Electron Transfer Dynamics: Suppressed Fluorescence Blinking of Single Molecules on Indium Tin Oxide Semiconductor. *J. Phys. Chem. B* **2016**, *120* (8), 1685–1697.
- (180) Hamann, T. W.; Gstrein, F.; Brunschwig, B. S.; Lewis, N. S. Measurement of the Free-Energy Dependence of Interfacial Charge-Transfer. *J. Am. Chem. Soc.* **2005**, *127*, 7815–7824.

- (181) DiMarco, B. N.; Troian-Gautier, L.; Marquard, S. L.; Meyer, G. J. Electron Transfer at TiO₂ Interface. A Comparative Study Between Free and Anchored Tri-Phenylamine (TPA) Redox Mediators. *In Prep.*
- (182) Quinton, C.; Alain-Rizzo, V.; Dumas-Verdes, C.; Miomandre, F.; Clavier, G.; Audebert, P. Redox-Controlled Fluorescence Modulation (Electrofluorochromism) in Triphenylamine Derivatives. *RSC Adv.* **2014**, *4* (65), 34332.
- (183) Davis, A. P.; Fry, A. J. Selective Oxidation of an Electronically Unsymmetrical Distyrylbenzene at Either of Two Sites. *J. Electrochem. Soc.* **2013**, *160* (7), G3091–G3096.
- (184) Daeneke, T.; Mozer, A. J.; Uemura, Y.; Makuta, S.; Fekete, M.; Tachibana, Y.; Koumura, N.; Bach, U.; Spiccia, L. Dye Regeneration Kinetics in Dye-Sensitized Solar Cells. *J. Am. Chem. Soc.* **2012**, *134* (41), 16925–16928.
- (185) Cias, P.; Slugovc, C.; Gescheidt, G. Hole Transport in Triphenylamine Based OLED Devices: From Theoretical Modeling to Properties Prediction. *J. Phys. Chem. A* **2011**, *115* (50), 14519–14525.
- (186) Jarzebski, Z. M. Physical Properties of SnO₂ Materials. *J. Electrochem. Soc.* **1976**, *123* (9), 299C.
- (187) Tiwana, P.; Docampo, P.; Johnston, M. B.; Snaith, H. J.; Herz, L. M. Electron Mobility and Injection Dynamics in Mesoporous ZnO, SnO₂, and TiO₂ Films Used in Dye-Sensitized Solar Cells. *ACS Nano* **2011**, *5* (6), 5158–5166.
- (188) Kay, A.; Grätzel, M. Dye-Sensitized Core–Shell Nanocrystals: Improved Efficiency of Mesoporous Tin Oxide Electrodes Coated with a Thin Layer of an Insulating Oxide. *Chem. Mater.* **2002**, *14* (7), 2930–2935.
- (189) Beauvilliers, E. E.; Meyer, G. J. Evidence for Cation-Controlled Excited-State Localization in a Ruthenium Polypyridyl Compound. *Inorg. Chem.* **2016**, *55* (15), 7517–7526.
- (190) Rowley, J. G.; Meyer, G. J. Di- and Tri-Iodide Reactivity at Illuminated Titanium Dioxide Interfaces. *J. Phys. Chem. C* **2011**, *115* (13), 6156–6161.
- (191) Li, G.; Hu, K.; Yi, C.; Knappenberger, K. L.; Meyer, G. J.; Gorelsky, S. I.; Shatruk, M. Panchromatic Light Harvesting and Hot Electron Injection by Ru(II) Dipyrrinates on a TiO₂ Surface. *J. Phys. Chem. C* **2013**, *117* (34), 17399–17411.
- (192) Ward, C. L.; O'Donnell, R. M.; DiMarco, B. N.; Meyer, G. J. Kinetic Resolution of Charge Recombination and Electric Fields at the Sensitized TiO₂ Interface. *J. Phys. Chem. C* **2015**, *119* (45).

- (193) O'Regan, B.; Moser, J.; Anderson, M.; Graetzel, M. Vectorial Electron Injection into Transparent Semiconductor Membranes and Electric Field Effects on the Dynamics of Light-Induced Charge Separation. *J. Phys. Chem.* **1990**, *94* (24), 8720–8726.
- (194) Chae, H.; Song, D.; Lee, Y.-G.; Son, T.; Cho, W.; Pyun, Y. B.; Kim, T.; Lee, J. H.; Fabregat-Santiago, F.; Bisquert, J.; Kang, Y. S. Chemical Effects of Tin Oxide Nanoparticles in Polymer Electrolytes-Based Dye-Sensitized Solar Cells. *J. Phys. Chem. C* **2014**, *118* (30), 16510–16517.
- (195) Kamat, P. V. Boosting the Efficiency of Quantum Dot Sensitized Solar Cells through Modulation of Interfacial Charge Transfer. *Acc. Chem. Res.* **2012**, *45* (11), 1906–1915.
- (196) Ogomi, Y.; Morita, A.; Tsukamoto, S.; Saitho, T.; Fujikawa, N.; Shen, Q.; Toyoda, T.; Yoshino, K.; Pandey, S. S.; Ma, T.; Hayase, S. $\text{CH}_3\text{NH}_3\text{Sn}_x\text{Pb}_{(1-x)}\text{I}_3$ Perovskite Solar Cells Covering up to 1060 nm. *J. Phys. Chem. Lett.* **2014**, *5* (6), 1004–1011.
- (197) Ghosh, H. N.; Asbury, J. B.; Lian, T. Direct Observation of Ultrafast Electron Injection from Coumarin 343 to TiO_2 Nanoparticles by Femtosecond Infrared Spectroscopy. *J. Phys. Chem. B* **1998**, *102* (34), 6482–6486.
- (198) Koops, S. E.; O'Regan, B. C.; Barnes, P. R. F.; Durrant, J. R. Parameters Influencing the Efficiency of Electron Injection in Dye-Sensitized Solar Cells. *J. Am. Chem. Soc.* **2009**, *131* (13), 4808–4818.
- (199) Benkő, G.; Myllyperkiö, P.; Pan, J.; Yartsev, A. P.; Sundström, V. Photoinduced Electron Injection from $\text{Ru}(\text{dcbpy})_2(\text{NCS})_2$ to SnO_2 and TiO_2 Nanocrystalline Films. *J. Am. Chem. Soc.* **2003**, *125* (5), 1118–1119.
- (200) Kelly, C. A.; Farzad, F.; Thompson, D. W.; Meyer, G. J. Excited-State Deactivation of Ruthenium(II) Polypyridyl Chromophores Bound to Nanocrystalline TiO_2 Mesoporous Thin Films. *Langmuir* **1999**, *15* (3), 731–737.
- (201) Hoertz, P. G.; Thompson, D. W.; Friedman, L. A.; Meyer, G. J. Ligand-Localized Electron Trapping at Sensitized Semiconductor Interfaces. *J. Am. Chem. Soc.* **2002**, *124* (33), 9690–9691.
- (202) Lyon, L. A.; Hupp, J. T. Energetics of the Nanocrystalline Titanium Dioxide/Aqueous Solution Interface: Approximate Conduction Band Edge Variations between $H_0 = -10$ and $H_- = +26$. *J. Phys. Chem. B* **1999**, *103* (22), 4623–4628.
- (203) Lemon, B. I.; Hupp, J. T. EQCM Investigations of Dye-Functionalized Nanocrystalline Titanium Dioxide Electrode/Solution Interfaces: Does Luminescence Report Directly on Interfacial Electron Transfer Kinetics? *J. Phys. Chem. B* **1999**, *103* (19), 3797–3799.

- (204) Pavlishchuk, V. V.; Addison, A. W. Conversion Constants for Redox Potentials Measured versus Different Reference Electrodes in Acetonitrile Solutions at 25°C. *Inorganica Chim. Acta* **2000**, 298 (1), 97–102.
- (205) Rehm, K. .; Weller, A. No Title. *Isr. J. Chem.* **1970**, 8, 259–271.
- (206) Boschloo, G.; Fitzmaurice, D. Spectroelectrochemical Investigation of Surface States in Nanostructured TiO₂ Electrodes. *J. Phys. Chem. B* **1999**, 103 (12), 2228–2231.
- (207) Wolfbauer, G.; Bond, A. M.; Deacon, G. B.; MacFarlane, D. R.; Spiccia, L. Experimental and Theoretical Investigations of the Effect of Deprotonation on Electronic Spectra and Reversible Potentials of Photovoltaic Sensitizers: Deprotonation of Cis -L₂RuX₂ (L = 2,2'-Bipyridine-4,4'-Dicarboxylic Acid; X = CN -, NCS -) by Elec. *J. Am. Chem. Soc.* **2000**, 122 (1), 130–142.
- (208) Wang, H.; He, J.; Boschloo, G.; Lindström, H.; Hagfeldt, A.; Lindquist, S.-E. Electrochemical Investigation of Traps in a Nanostructured TiO₂ Film. *J. Phys. Chem. B* **2001**, 105 (13), 2529–2533.
- (209) Wang, H.; Bell, J.; Desilvestro, J.; Bertoz, M.; Evans, G. Effect of Inorganic Iodides on Performance of Dye-Sensitized Solar Cells. *J. Phys. Chem. C* **2007**, 111 (41), 15125–15131.
- (210) Kislenko, S. A.; Amirov, R. H.; Samoylov, I. S. Effect of Cations on the TiO₂/acetonitrile Interface Structure: A Molecular Dynamics Study. *J. Phys. Chem. C* **2013**, 117 (20).
- (211) Zhang, C. N.; Huang, Y.; Chen, S. H.; Tian, H. J.; Mo, L. E.; Hu, L. H.; Huo, Z. P.; Kong, F. T.; Ma, Y. W.; Dai, S. Y. Photoelectrochemical Analysis of the Dyed TiO₂/Electrolyte Interface in Long-Term Stability of Dye-Sensitized Solar Cells. *J. Phys. Chem. C* **2012**, 116, 19807–19813.
- (212) Fredin, K.; Nissfolk, J.; Boschloo, G.; Hagfeldt, A. The Influence of Cations on Charge Accumulation in Dye-Sensitized Solar Cells. *J. Electroanal. Chem.* **2007**, 609 (2), 55–60.
- (213) Hampden-Smith, M. J.; Williams, D. S.; Rheingold, A. L. Synthesis and Characterization of Alkali-Metal Titanium Alkoxide Compounds MTi(O-Iso-Pr)₅ (M = Li, Na, K): Single Crystal X-Ray Diffraction Structure of [LiTi(O-Iso-Pr)₅]₂ *Inorg. Chem.* **1990**, 29 (20), 4076–4081.
- (214) Song, W.; Luo, H.; Hanson, K.; Concepcion, J. J.; Brennaman, M. K.; Meyer, T. J. Visualization of Cation Diffusion at the TiO₂ Interface in Dye Sensitized Photoelectrosynthesis Cells (DSPEC). *Energy Environ. Sci.* **2013**, 6 (4), 1240.

- (215) Kamat, P. V.; Bedja, I.; Hotchandani, S.; Patterson, L. K. Photosensitization of Nanocrystalline Semiconductor Films. Modulation of Electron Transfer between Excited Ruthenium Complex and SnO₂ Nanocrystallites with an Externally Applied Bias. *J. Phys. Chem.* **1996**, *100* (12), 4900–4908.
- (216) Farzad, F.; Thompson, D. W.; Kelly, C. a; Meyer, G. J. Competitive Intermolecular Energy Transfer and Electron Injection at Sensitized Semiconductor Interfaces. *J. Am. Chem. Soc.* **1999**, *121* (23), 5577–5578.
- (217) Rao, V. G.; Dhital, B.; Peter Lu, H. Single-Molecule Interfacial Electron Transfer Dynamics of Porphyrin on TiO₂ Nanoparticles: Dissecting the Interfacial Electric Field and Electron Accepting State Density Dependent Dynamics. *Chem. Commun.* **2015**, *51* (94), 16821–16824.
- (218) Kersting, R.; Lemmer, U.; Deussen, M.; Bakker, H. J.; Mahrt, R. F.; Kurz, H.; Arkhipov, V. I.; Bessler, H.; Gebel, E. O. Ultrafast Field-Induced Dissociation of Excitons in Conjugated Polymers. *Phys. Rev. Lett.* **1994**, *73* (10), 1440–1443.
- (219) Stampor, W.; Kalinowski, J.; Di Marco, P.; Fattori, V. Electric Field Effect on Luminescence Efficiency in 8-Hydroxyquinoline Aluminum (Alq₃) Thin Films. *Appl. Phys. Lett.* **1997**, *70* (15), 1935.
- (220) Szmytkowski, J.; Stampor, W.; Kalinowski, J.; Kafafi, Z. H. Electric Field-Assisted Dissociation of Singlet Excitons in Tris-(8-Hydroxyquinolino) Aluminum (III). *Appl. Phys. Lett.* **2002**, *80* (8), 1465–1467.
- (221) Smith, T. M.; Hazelton, N.; Peteanu, L. A.; Wildeman, J. Electrofluorescence of MEH-PPV and Its Oligomers: Evidence for Field-Induced Fluorescence Quenching of Single Chains. *J. Phys. Chem. B* **2006**, *110* (15), 7732–7742.
- (222) Adams, D. M.; Kerimo, J.; Liu, C.; Bard, A. J.; Barbara, P. F. Electric Field Modulated Near-Field Photo-Luminescence of Organic Thin Films. *J. Phys. Chem. B* **2000**, *104* (29), 6728–6736.
- (223) Kalinowski, J.; Stampor, W.; Di Marco, P. Electromodulation of Luminescence in Organic Photocinductors. *J. Electrochem. Soc.* **1996**, *143* (1), 315–325.
- (224) Braun, C. L. Electric Field Assisted Dissociation of Charge Transfer States as a Mechanism of Photocarrier Production. *J. Chem. Phys.* **1984**, *80* (9), 4157–4161.
- (225) Noolandi, J.; Hong, K. M. Theory of Photogeneration and Fluorescence Quenching. *J. Chem. Phys.* **1979**, *70* (7), 3230.
- (226) Kalinowski, J.; Stampor, W.; Mezyk, J.; Cocchi, M.; Virgili, D.; Fattori, V.; Di Marco, P. Quenching Effects in Organic Electrophosphorescence. *Phys. Rev. B* **2002**, *66*, 1–15.

- (227) Clarke, T. M.; Durrant, J. R. Charge Photogeneration in Organic Solar Cells. *Chem. Rev.* **2010**, *110* (11), 6736–6767.
- (228) Brauer, J. C.; Marchioro, A.; Paraecattil, A. A.; Oskouei, A. A.; Moser, J.-E. Dynamics of Interfacial Charge Transfer States and Carriers Separation in Dye-Sensitized Solar Cells: A Time-Resolved Terahertz Spectroscopy Study. *J. Phys. Chem. C* **2015**, *119* (47), 26266–26274.
- (229) D’Angelantonio, M.; Mulazzani, Q. G.; Venturi, M.; Ciano, M.; Hoffman, M. Z. One-Electron Reduction of ruthenium(II)-Diimine Complexes: Characterization of Reduced Species Containing 2,2’-bipyridine, 2,2’-bipyrimidine, and 2,2’-bipyrazine in Aqueous Solution. *J. Phys. Chem.* **1991**, *95* (13), 5121–5129.